ELECTRON PARAMAGNETIC RESONANCE STUDIES OF BETA-ALUMINA, A PROTOTYPE GLASS

BY

STEVEN ROSS KURTZ

B.S., Bucknell University, 1975
M.S., University of Illinois, 1977

THESIS

Submitted in partial fulfillment of the requirements
for the degree of Doctor of Philosophy in Physics
in the Graduate College of the
University of Illinois at Urbana-Champaign, 1980

Urbana, Illinois

DISCLAIMER

ELECTRON PARAMAGNETIC RESONANCE STUDIES OF BETA-ALUMINA, A PROTOTYPE GLASS

BY

STEVEN ROSS KURTZ

B.S., Bucknell University, 1975
M.S., University of Illinois, 1977

THESIS

Submitted in partial fulfillment of the requirements
for the degree of Doctor of Philosophy in Physics
in the Graduate College of the
University of Illinois at Urbana-Champaign, 1980

Urbana, Illinois

ELECTRON PARAMAGNETIC RESONANCE STUDIES OF BETA-ALUMINA, A PROTOTYPE GLASS

Steven Ross Kurtz, Ph.D
Department of Physics
University of Illinois at Urbana-Champaign, 1980

Electron paramagnetic resonance techniques are used to study single crystal Na, K, and Li beta-alumina. Color centers are introduced into this material by irradiating the samples with electrons at liquid nitrogen temperature. Using electron paramagnetic resonance and electron nuclear double resonance, the color centers generated in this manner are identified, and their location within the material is determined. For one of these centers, an F^+ center, the electron spin relaxation rate is measured over the range 2-20 K using the pulse saturation and recovery technique. These measurements reveal an exceptionally fast relaxation rate with anomalous temperature and microwave frequency dependence.

Beta-alumina is a structurally unique system. It is partially disordered and consists of ordered blocks of aluminum oxide separated by planar disordered regions. Extensive measurements have shown that beta-alumina displays properties identical to those observed for glasses at low temperature as a result of this limited structural disorder. These glass-like properties have been explained by proposing that atomic tunneling occurs in beta-alumina at low temperature producing a system of localized two level states.

A model is developed which quantitatively describes the electron spin relaxation data. The proposed relaxation mechanism couples the

color center spin to the phonon induced relaxation of a nearby localized two level tunneling state. A detailed comparison shows that this model is in good agreement with earlier heat capacity, thermal conductivity, and dielectric susceptibility measurements in beta-alumina.

ACKNOWLEDGMENTS

I wish to thank my advisor, Professor Harvey J. Stapleton, for his guidance, encouragement, and friendship during the course of this research. He has provided me with a stimulating environment in which to work, and through his dedication to teaching, he has contributed greatly to my professional development.

Among several of my fellow graduate students who have helped me during my graduate education, I particularly want to thank Mr. Douglas G. Stinson for assistance in constructing the EPR and ENDOR spectrometers and for his help with some of the EPR measurements in this thesis. I have learned many things through our collaboration and numerous discussions.

I am grateful to Prof. A. C. Anderson and Dr. P. J. Anthony for providing the samples used in this study and introducing me to the properties of glasses. Dr. M. M. Abraham's abundant advice concerning the EPR and ENDOR of color centers is also appreciated.

Finally, I want to thank my father and late mother for their example and support, and I thank my wife, Mary, for her encouragement and patience.

This research was supported by the Department of Energy through Contract DE-AC02-76ER01198.

TABLE OF CONTENTS

I. INTRODUCTION

The family of materials referred to as beta-alumina is an ideal system for the study of a wide range of physical phenomena related to disorder. At low temperatures single crystals of this solid exhibit thermal, dielectric, and acoustic properties typical of glasses. These results on beta-alumina agree with predictions of the localized tunneling state theory developed for disordered materials. At higher temperatures beta-alumina is a fast ionic (superionic) conductor, and it has been used as a solid electrolyte in batteries.

These interesting properties result because single crystal beta-alumina is partially disordered with the disordered region consisting of a two-dimensional plane sandwiched between ordered structures. However, since this material is only partially ordered, it is possible to study the properties of amorphous solids while utilizing some of the advantages of working with a single crystal. For example, the "confined disorder" in beta-alumina allows identification of color centers and tunneling species with a higher degree of certainty than would be possible in a typical glass. This property has been used repeatedly throughout this work to reduce the number of "variables" normally encountered when studying amorphous materials.

In Chapter II, a brief summary of the properties of beta-alumina is presented. This review is not intended to be complete. Emphasis has been placed on the subjects needed to analyze the experiments in this thesis, and for this reason, some important topics in the field have been

omitted. (The best review on beta-alumina is by J. H. Kennedy, Ref. 1.) Part A of this chapter describes the structure of beta-alumina and introduces several facts for later reference. Part B discusses the superionic properties of beta-alumina, and Part C is a qualitative description of its low temperature glass-like properties. Part C serves as an introduction to the concepts and previous experiments which form the basis of the spin relaxation studies in this work.

Electron paramagnetic resonance (EPR) and related measurements, electron-nuclear double resonance (ENDOR) and electron spin relaxation, are attractive techniques for studying disordered solids. EPR and ENDOR provide information about the identity and structural surroundings of a paramagnetic species, whereas electron spin relaxation measurements probe the low energy excitations within a material. However, these experiments have not previously been productive in studying typical glasses. The extensive disorder of these materials often made it impossible to resolve ligand hyperfine interactions from EPR and ENDOR results, and as a result little structural information was provided by these experiments. This factor plus a lack of adequate data from other low temperature measurements made detailed analysis of electron spin relaxation results very speculative for most disordered solids.

For beta-alumina the application of EPR techniques is not limited by these difficulties. Some hyperfine interactions between paramagnetic centers and adjacent nuclei are resolvable, and enough low temperature data exist to permit an in depth study of electron spin relaxation in this glass. Since beta-alumina is not naturally paramagnetic, it was necessary to introduce a paramagnetic probe into the material to perform

these experiments. Color centers were successfully generated by electron irradiation in the disordered region of beta-alumina, and EPR and ENDOR were used to identify these centers. The production and characterization of color centers in beta-alumina is the subject of Chapter III.

Finally, Chapter IV discusses electron spin relaxation measurements on a F^+ center produced by irradiation. A model is introduced which explains the relaxation data and agrees with previous low temperature measurements on beta-alumina. This experiment represents the first quantitative study of electron spin relaxation in a glass.

II. PHYSICAL PROPERTIES OF BETA-ALUMINA

A. Structure

The interesting physical properties of M beta-alumina (M = Na, K, Li, etc.) result from its unique structure. The material consists of ordered, 8 Å wide, spinel-like blocks of Al^{3+} and O^{2-}. Within this lattice, the oxygen atoms form close packed layers, and the aluminum atoms occupy both octahedral and tetrahedral sites between the oxygen layers. Every fifth layer, the spinel structure is violated by the presence of a disordered plane containing M^+ and O^{2-}. The M^+ cations reside only in this region called the conduction plane. The spinel blocks are stacked so that the conduction plane is a mirror plane, and there are two spinel blocks and two conduction planes per unit cell. Beta-alumina has a hexagonal crystal structure with lattice constants a = 5.59 Å and c = 22.53 Å for Na beta-alumina.[1,2] (See Fig. 1a.)

The conduction plane is an open, oxygen depleted region where the M^+ ions can reside at several different sites. These are the BR (Beevers-Ross), aBR (anti-Beevers-Ross), and mO (mid-oxygen) sites. (See Fig. 1b.) The occupation of these sites by M^+ ions is highly temperature dependent and varies for the different types of M^+ cations. For example, the site occupation probabilities for Na^+ in Na beta-alumina are 0.63, 0.36, and 0.01 for the BR, mO, and aBR sites respectively at 80 K.[3] With increasing temperature, Na^+ ions are transferred from BR and mO sites to aBR sites. At lower temperatures the Na^+ site occupation remains about the

Figure 1a. Stoichiometric structure of Na beta-alumina. Half of a unit cell is shown, and the Na cations occupy Beevers-Ross (BR) sites. The Na ions are located in conduction planes perpendicular to the c axis. The four different Al atoms are labeled within the figure. (Ref. 51)

b. Structure of the conduction plane of stoichiometric Na beta-alumina. Only Beevers-Ross (BR) Na cations and "bridge" oxygen ions are shown in the conduction plane and indicated by dark circles. Other Na sites, the anti-Beevers-Ross (aBR) and the mid-oxygen (mO) sites, are also marked "x". Light circles are the closed-packed oxygen layer above and below the conduction plane. The unit cell of Fig. 1a is indicated by the dotted line. (Ref. 51)

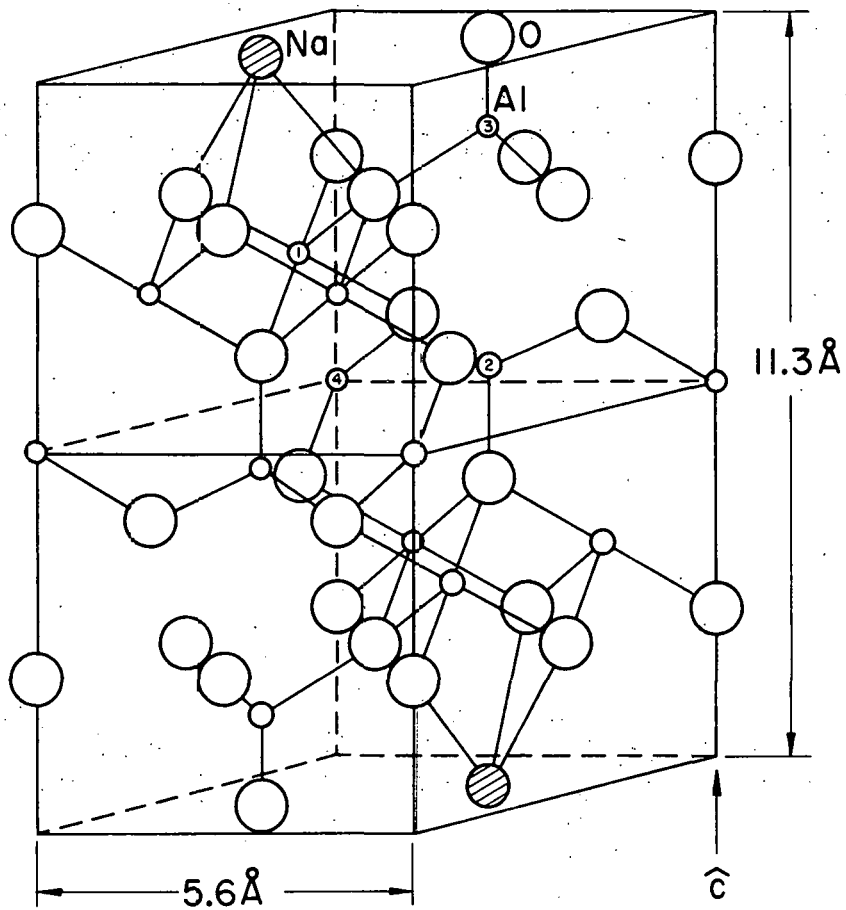

(a)

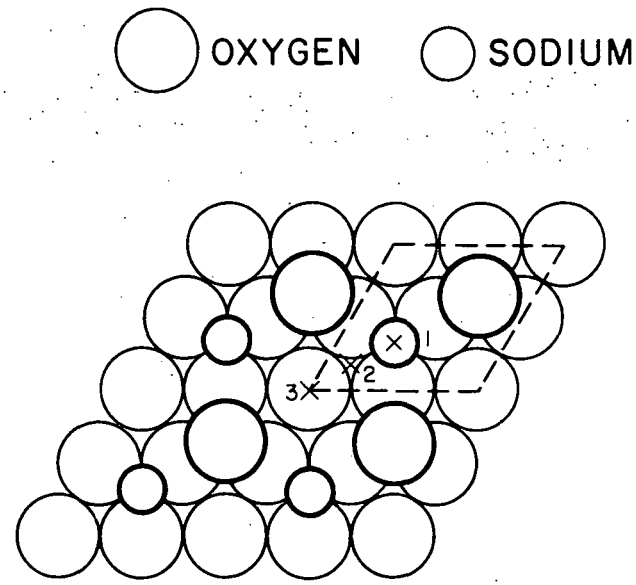

1 : BR 2 : mO 3 : aBR

(b)

same as at 80 K because these cations are essentially frozen-in at this temperature.

The conduction plane disorder is further complicated by the fact that beta-alumina is non-stoichiometric. Na beta-alumina has been observed to be stable over the range 15%-30% excess Na^+ ions residing in the conduction plane producing a chemical composition of 1.15 $Na_2O \cdot 11Al_2O_3$ to 1.30 $Na_2O \cdot 11Al_2O_3$.[1] Density changes with ion exchange indicate the samples used in this study contained ≈17% excess cations over stoichiometry.[4] This would result in (0.63 • 1.17 = 0.74) 74% and (0.36 • 1.17/3 = 0.14) 14% of the BR and mO sites respectively being occupied by Na^+ at 80 K. (There are 3 mO sites per BR or aBR site.) As expected, the structure of the conduction plane varies for different types of beta-alumina and depends on the method of producing the crystals, but at low temperature the physical picture presented here for Na beta-alumina also accurately represents the structure of the other materials studied in this work, Li and K beta-alumina.

With the excess cations in beta-alumina, a significant number of charge compensating defects are required to maintain electrical neutrality. Based on x-ray[2,5] and neutron diffraction[3] data, Roth proposed the excess cations are compensated by O^{2-} ions located at mO sites within the conduction plane. These negative ions symmetrically distort the positions of the two Al^{3+} ions normally located on each side of the mO site along the c axis. This results in the formation of aluminum vacancy-interstitial pairs (Frenkel defects) and creates another Al-O-Al bond across the conduction plane. This defect structure occurs in roughly every tenth unit cell depending on the M^+ composition.

In this discussion of the M^+ cation and charge compensation structure of the conduction plane, no mention has been made of ion displacements perpendicular to the conduction plane which would break the mirror symmetry of the plane, and for K and Na beta-alumina, there has been no evidence to support this ion displacement. However, for Li beta-alumina, Raman data indicates that the Li^+ cations are displaced $\simeq$ 0.8 Å from the center of the plane towards the spinel block.[6] It is believed that the small Li^+ ionic radius allows these cations to reside in "pocket sites" created by the close packed oxygen layers next to the conduction plane. If the BR and mO Li^+ ions are both displaced out of the plane in this manner, it is even possible to form two layers of Li^+ ions 1.6 Å apart. This structural difference must be considered when comparing Li beta-alumina results with data for the other types of beta-alumina.

B. Fast Ion Conduction

Most of the research on beta-alumina involves its behavior as a fast ionic conductor. In general these materials are referred to as superionic conductors because they have anomalously high ionic conductivity. For Na beta-alumina at room temperature, $\sigma \simeq 10^{-2}$ $(\Omega\ \text{cm})^{-1}$ contrasted with $\sigma \simeq 10^{-6}$ $(\Omega\ \text{cm})^{-1}$ for NaCl. This enormous difference in ionic conductivity is a consequence of the extensive disorder in the structure of superionic conductors instead of ionic conduction via the motion of isolated defects and impurities which occurs in ordered ionic crystals like NaCl.

For M beta-alumina, the M^+ cation is a mobile charge carrier within the conduction plane, and its motion has been described by thermally activated hopping or diffusion between the cation sites mentioned in Part A. The temperature dependence of superionic ionic conductivity is described by an Arrhenius relation

$$\sigma = (\sigma_o/T) \exp(-Q_c/kT) \qquad (1)$$

where σ_o is a constant, and Q_c is a mobile ion activation energy.[7] For single crystal Na beta-alumina, Q_c = 0.17 eV from ^{23}Na NMR linewidth data, in good agreement with diffusion and conductivity measurements.[1] Other types of beta-alumina have larger values of Q_c due to the fact that the Na^+ ion is probably an ideal size for the beta-alumina conduction plane. Larger ions may experience a greater electrostatic repulsion than Na^+, and Li^+ ions are probably small enough to be trapped in the "pocket sites" of the spinel block.[8] (This discussion of conductivity and ion size does not always apply for mixed-ion beta-alumina.)

For discussion of the results of the experiments in this thesis, this description of the superionic behavior of beta-alumina is adequate, but in reality this picture is an oversimplification. Superlattice and cluster formation of cations and charge compensation defects has been reported by diffuse x-ray scattering,[9,10] and ion-ion correlations have been proposed to explain diffusion data for beta-alumina.[11,12]

The high temperature M^+ mobility allows cations to be substituted into the conduction plane by ion exchange. To prevent water from entering the conduction plane, ion exchange is usually carried out by using an appropriate molten salt. For example, the K and Li beta-alumina samples

used in this study were produced by repeated immersion of Na beta-alumina into molten KNO_3 or $LiNO_3$.[4] Mixed-ion beta-aluminas and substitution of divalent ions has also been reported using this method[1] making beta-alumina a versatile system for experiments and practical applications.

C. Low Temperature Properties

The thermal, acoustic, and dielectric properties of amorphous insulators at low temperature are fundamentally different from the properties seen in corresponding materials in the crystalline form. These differences are observed through both the magnitude and temperature dependence obtained from a given experiment, and the same general results are obtained for a wide variety of amorphous dielectrics indicating the observed behavior is a consequence of disorder and not due to the chemical composition of a particular material. At low temperature beta-alumina also displays properties identical to those characteristic of glasses, and to begin this discussion, it is necessary to survey the data obtained from other amorphous solids for comparison with beta-alumina results and to understand the motivation behind applying the localized tunneling state (LTS) model to beta-alumina.

The effects of disorder can clearly be seen by comparing data for crystalline α-quartz and a silica glass, vitreous silica. Although these materials have the same chemical composition, SiO_2, their thermal properties are distinctly different. Debye theory predicts for phonon contributions to the specific heat, $C_p \propto T^3$.[13] This behavior is observed in the α-quartz specific heat data displayed in Fig. 2a. However, the data

Figure 2a. A comparison of specific heat data for a glass, vitreous silica, and a crystal, α-quartz, having the same chemical composition as the glass. (Ref. 14)

b. A comparison of thermal conductivity data for vitreous silica and α-quartz. (Ref. 14)

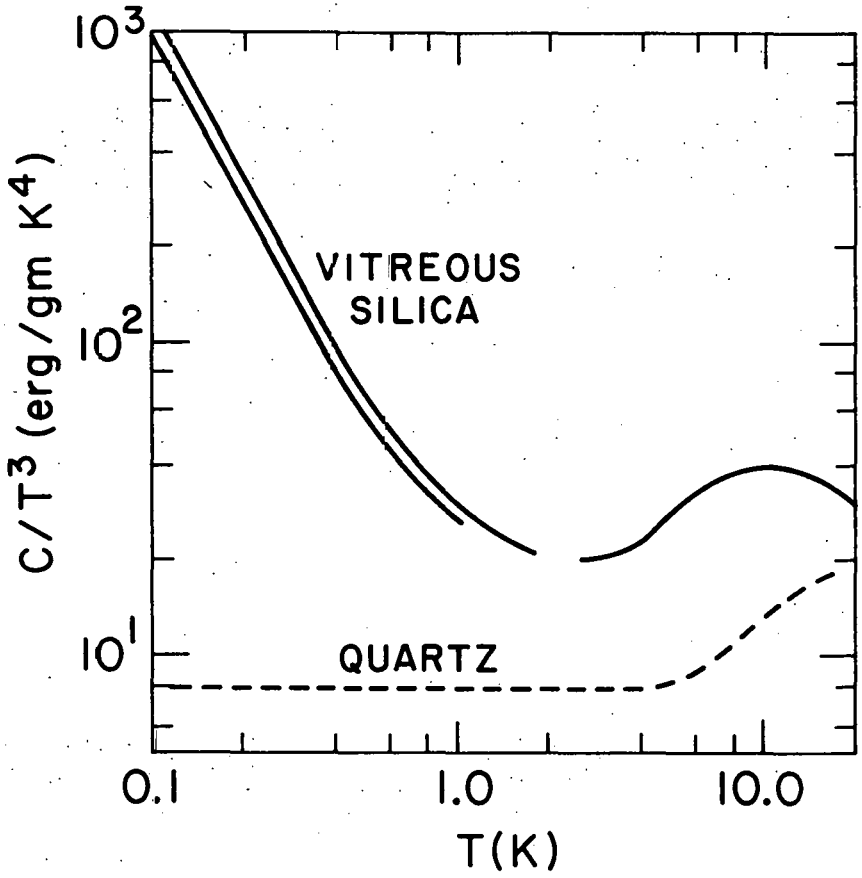
10^3
10^2
10^1
C/T^3 (erg/gm K^4)
VITREOUS
SILICA
QUARTZ
0.1
1.0
10.0
T(K)

(a)

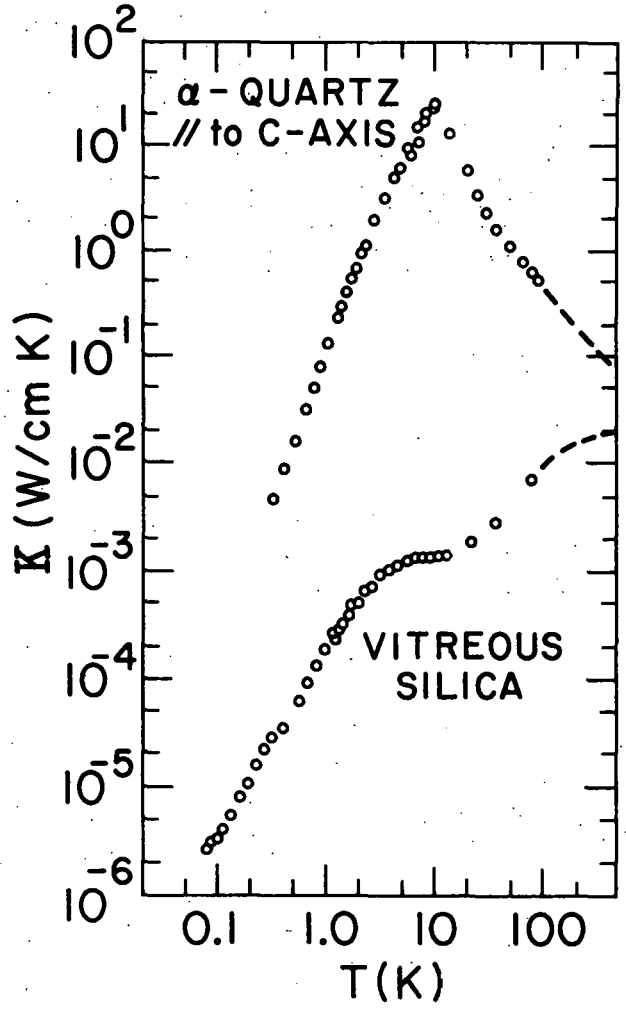
10^2
10^1
10^0
10^{-1}
10^{-2}
10^{-3}
10^{-4}
10^{-5}
10^{-6}
K (W/cm K)
α - QUARTZ
// to C-AXIS
VITREOUS
SILICA
0.1
1.0
10
100
T(K)

(b)

for vitreous silica in the same graph has an excess specific heat with $C_p \propto T$ for $T \leq 1$ K.

Comparison of the thermal conductivity also reveals anomalous results due to disorder. From kinetic theory,

$$K = (1/3)\, C_p\, v\ell \qquad (2)$$

where C_p is the phonon specific heat, v the phonon velocity, and ℓ the phonon mean free path.[13] At lowest temperatures in a perfect crystal, ℓ is limited only by the sample size producing $K \propto T^3$ in agreement with the α-quartz data in Fig. 2b. For vitreous silica, K is proportional to T^2 in this figure, and there is a plateau in the thermal conductivity near 10 K.

The $C_p \propto T$ and $K \propto T^2$ behavior is not unique to vitreous silica. These same effects have been seen in a wide range of disordered substances including inorganic glasses, amorphous polymers, and even grease.[14] (For the purposes of this thesis, any of these materials can be referred to as a "glass".) Specific heat and thermal conductivity results can both be explained by a distribution of low energy states in glasses which interact with the phonons enhancing phonon scattering. This picture is also supported by ultrasonic absorption and sound velocity data,[15,16,17] and in particular, saturation of the ultrasonic absorption has been observed indicating the low energy excitations have a finite number of accessible states.

Assuming these low energy states have an electric-dipole moment, glasses should display anomalous dielectric properties at low temperature similar to the manner in which these materials interact with sound waves.

In an ordered dielectric, the low frequency dielectric constant is independent of temperature, but in glasses the ε vs T curve is characterized by a distinct frequency dependent minima at low temperature.[18,19] Analogous to the ultrasonic experiments, saturation of dielectric absorption also occurs at sufficiently high intensities.[20]

In 1972, Anderson, Halperin, Varma,[21] and Phillips[22] proposed the LTS model which has been successful in describing the diverse phenomena observed in glasses at low temperature. This model assumes that atoms or groups of atoms in amorphous materials reside in asymmetric double well potentials, and tunneling occurs through the barrier separating the two wells. This results in a localized, two energy level system. Since there is a variety of local environments within a disordered material, it is reasonable for there to be a distribution of energy splittings of the 2-level states, $P_o(E)$. The form of $P_o(E)$ cannot be derived from first principles, but it is found that $P_o(E)$ equal to a constant for $0 \leq E \leq E_{max}$ predicts the approximate temperature dependence for all of the "anomalous" effects observed in glasses. As a result, this form of density of tunneling states has become a distinguishing characteristic of the LTS system.

With this brief description of the LTS model, it is now possible to describe some of the applications of this theory. The expression for the excess specific heat due to the LTS system is[21]

$$C_p = k \int_o^{E_{max}} P_o(E) \left(\frac{E}{kT}\right)^2 \frac{\exp(-E/kT)}{[1 + \exp(-E/kT)]^2} \, dE \quad . \qquad (3)$$

For $kT << E_{max}$ and $P_o(E) = P_o$, a constant, this becomes

$$C_p = (\pi^2/6) \, P_o \, k^2 T. \qquad (4)$$

Therefore, with minor corrections to $P_o(E)$, the LTS model can predict the low temperature specific heat data for glasses.

The ultrasonic and dielectric properties of glasses are described by scattering processes involving the LTS system. Using the golden rule, the rate at which a phonon or photon is absorbed by a resonant ($E = \hbar\omega$) LTS is[4,15]

$$1/\tau_{res} \propto P_o(\hbar\omega)\ \omega\ \tanh(\hbar\omega/2kT) \quad . \tag{5}$$

By using this scattering process to determine the phonon mean free path and averaging over phonon energies, $K \propto T^2$ is obtained for $P_o(\hbar\omega) = P_o$.[15] (LTS contributions to the specific heat are not included in Eq. (2) because the LTS do not transport heat.) Another scattering process observed experimentally is relaxation scattering.[4,15,17] As an elastic or electromagnetic wave passes through the glass, it distorts the energy splittings of the two-level states, and the LTS emit or absorb phonons to maintain thermal equilibrium thus attenuating the wave. This attenuation is characterized by

$$1/\tau_{rel} \propto P_o\ T^3 \quad . \tag{6}$$

The sum of resonant and relaxation scattering processes with their different temperature dependences produces via a Kramers-Kronig transformation the characteristic minima in the ε vs T data for glasses.[4,18]

Comparing the results of low temperature measurements on beta-alumina with the predictions of the LTS model, specific heat data for several beta-aluminas are shown in Fig. 3. For $T \leq 1$ K the excess specific heat is well described by $C_p \propto T$. Deviation from this behavior at the

Figure 3. Measured specific heat of beta-alumina. The solid lines are predicted using the LTS model. (Ref. 4 and 23) The higher temperature data indicated by the dotted lines is attributed to Einstein oscillators. (Ref. 74)

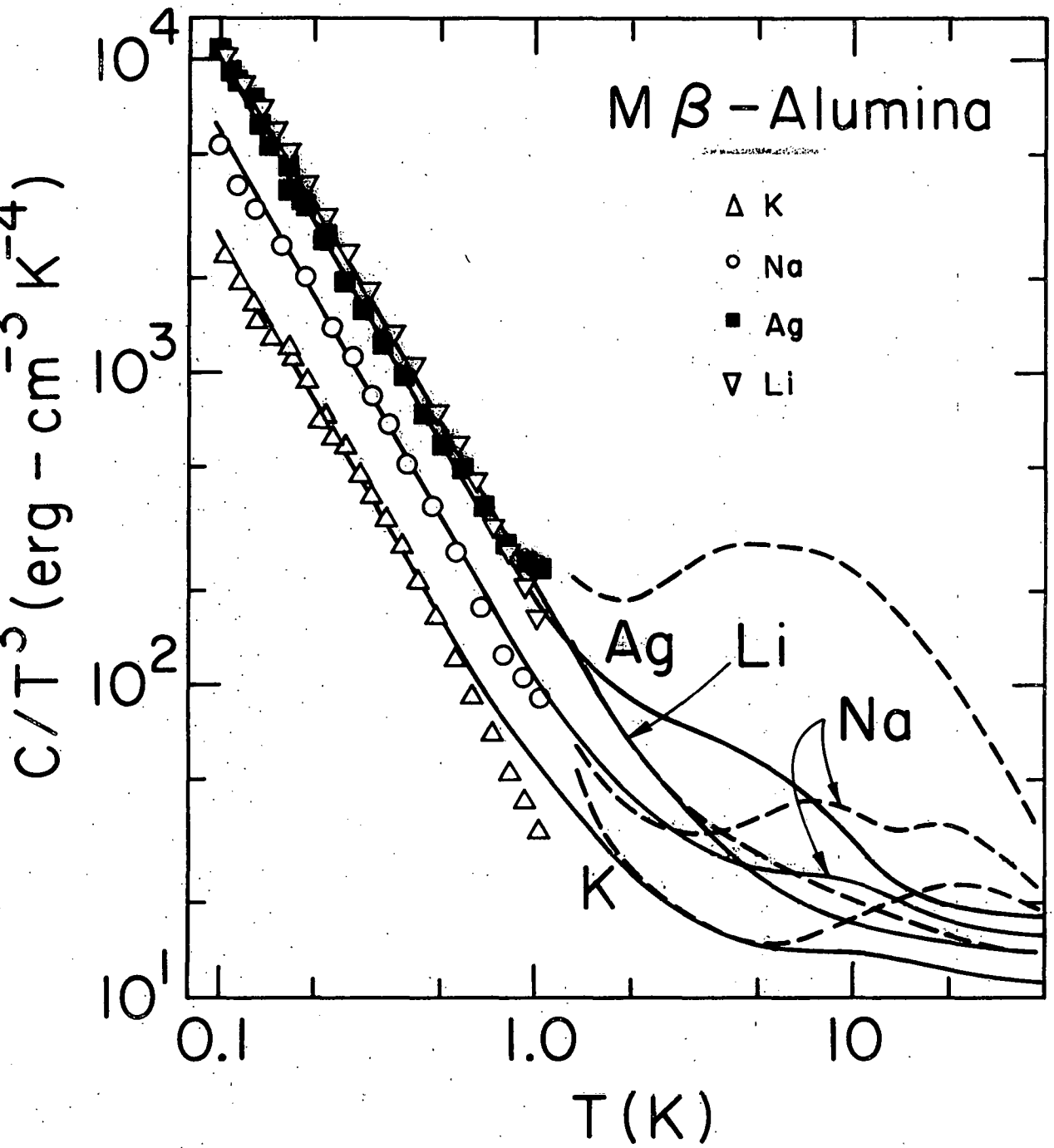
M β – Alumina
Δ K
○ Na
■ Ag
▽ Li
Ag
Li
Na
K
10^4
10^3
10^2
10^1
0.1
1.0
10
T(K)
C/T^3 (erg – cm^{-3} K^{-4})

higher temperatures in this figure is due to contributions from Debye phonons and Einstein oscillator states.[23,24] Thermal conductivity data (Fig. 4) is also in agreement with the predictions of the LTS model. For Ag, Li, and Na beta-alumina the $K \propto T^2$ behavior is observed. Also, the characteristic plateau is seen at ≈10 K for these materials. In K beta-alumina thermal conductivity is proportional to T^3 indicating that boundary scattering dominates LTS scattering in this case.[25]

Variation of the dielectric constant ($\Delta\varepsilon/\varepsilon$) vs temperature for beta-alumina is displayed in Fig. 5-7. (In each curve ε is a fixed but arbitrary value.) Each of these curves show the characteristic minima in dielectric constant, and the minima position shifts with frequency as predicted by the LTS model. Similar $\Delta\varepsilon/\varepsilon$ vs T behavior and saturation of dielectric absorption has been observed at microwave frequencies for Na beta-alumina.[26] The results of the microwave study are also in quantitative agreement with the lower frequency data of Anthony and Anderson.[27]

At this time it is necessary to point out several interesting conclusions of the dielectric susceptibility experiments on beta-alumina. Glass-like behavior was observed in each sample when the $\vec{E}$ field was perpendicular to the c axis, but only Li beta-alumina displayed glass-like behavior when $\vec{E}$ was parallel to the c axis.[23] This indicates that the LTS electric-dipoles are perpendicular to the c axis except for Li beta-alumina where the dipole may have a component pointing out of the conduction plane. Remembering that only Li cations can reside out of the conduction plane in "pocket sites," this result suggests that the conduction plane cations are actually tunneling. Also, the specific heat and thermal conductivity data was dependent on the type of cation present

Figure 4. Measured thermal conductivity of beta-alumina. The solid lines are predicted using the LTS model. (Ref. 4 and 25)

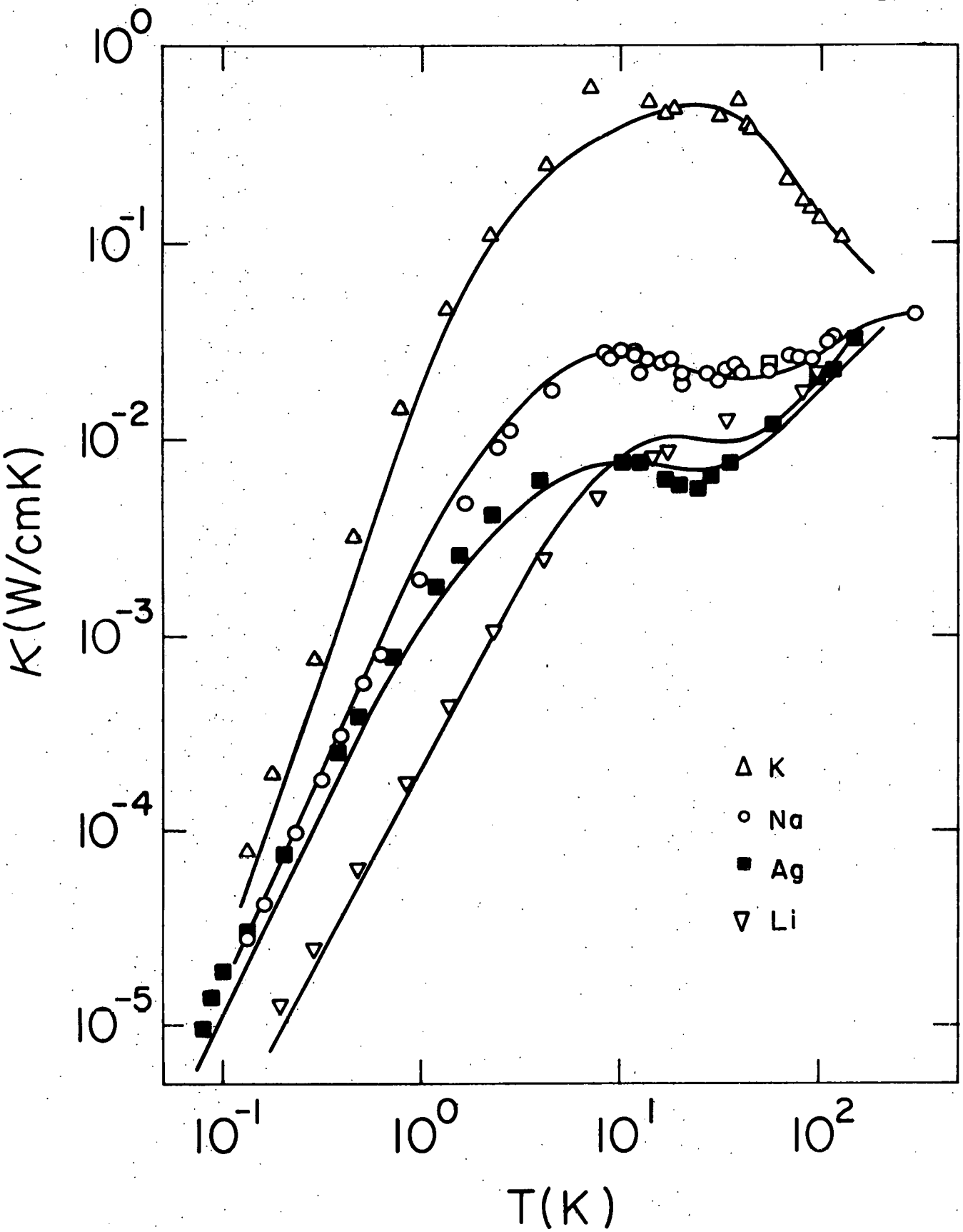
10^0
10^{-1}
10^{-2}
10^{-3}
10^{-4}
10^{-5}
K(W/cmK)
10^{-1}
10^0
10^1
10^2
T(K)
Δ K
○ Na
■ Ag
▽ Li

Figure 5. Measured variation of dielectric susceptibility as a function of temperature for Na beta-alumina. The solid lines are predicted using the LTS model. (Ref. 4 and 23) The dotted line is the 11.5 GHz data. (Ref. 26)

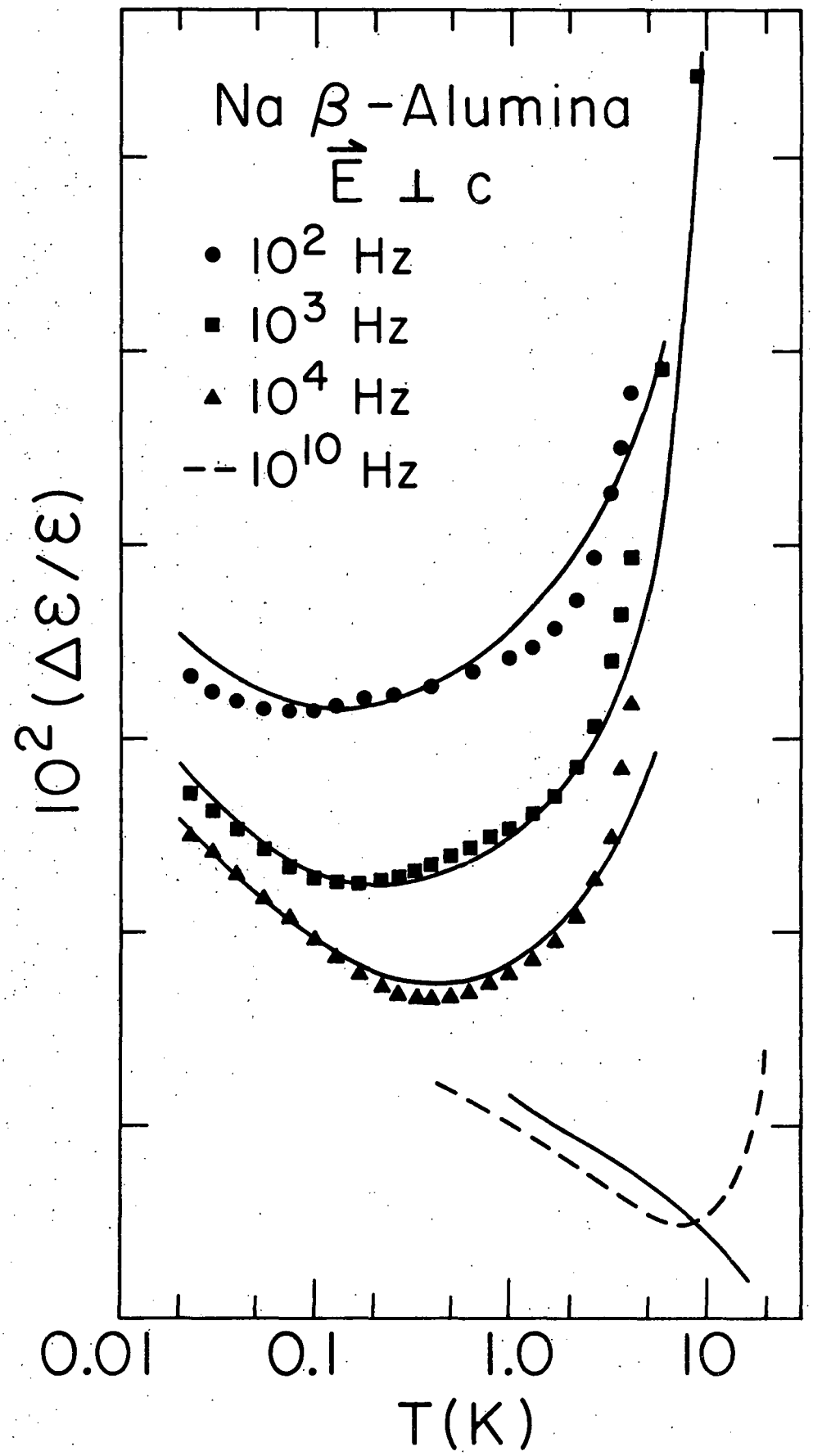
Na β-Alumina
$\vec{E} \perp c$
10^2 Hz
10^3 Hz
10^4 Hz
10^{10} Hz
$10^2(\Delta\varepsilon/\varepsilon)$
0.01
0.1
1.0
10
T(K)

Figure 6. Measured variation of dielectric susceptibility as a function of temperature for K beta-alumina. The solid lines are predicted using the LTS model. (Ref. 4 and 23)

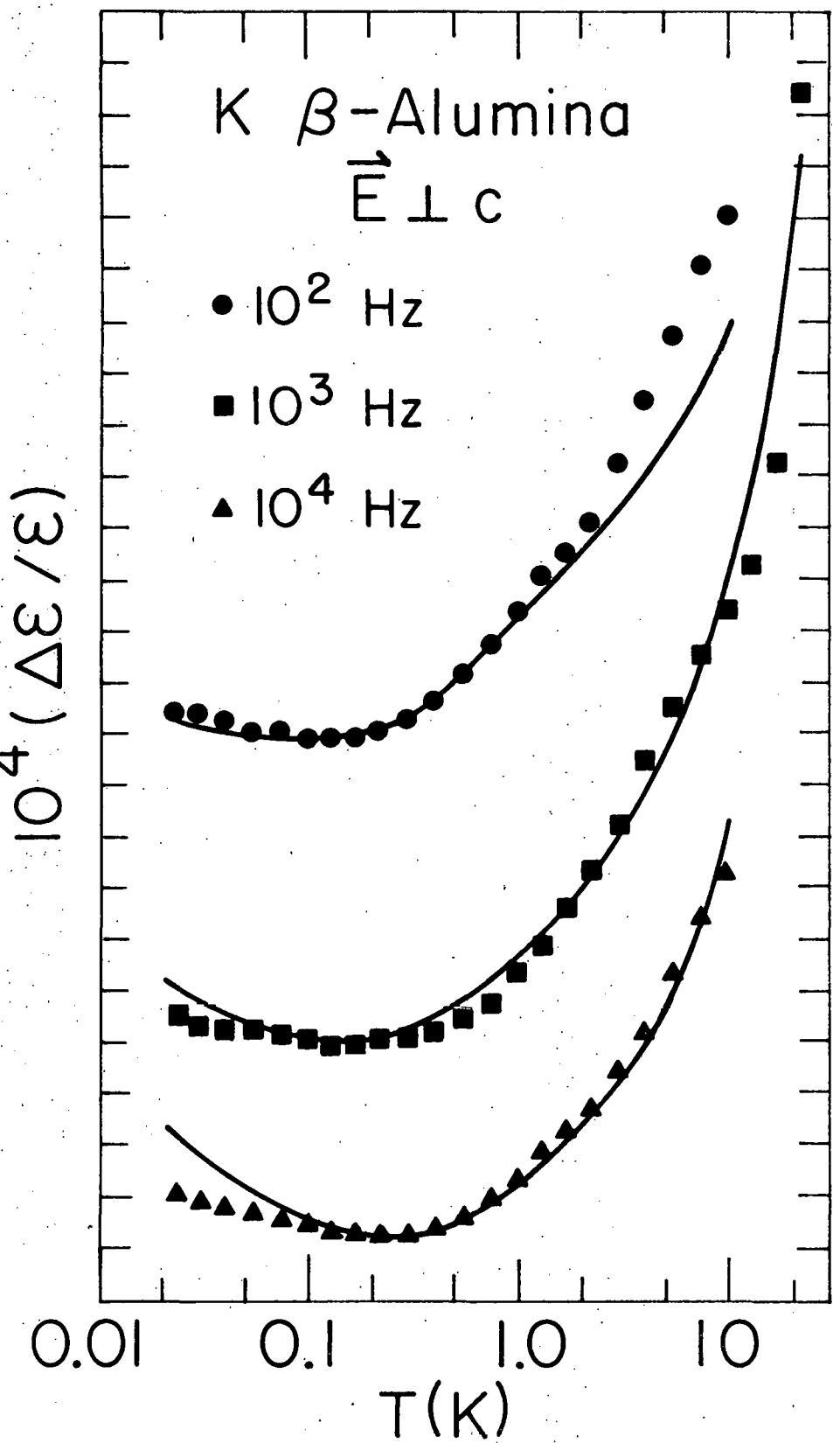
K β-Alumina
$\vec{E} \perp c$
10^2 Hz
10^3 Hz
10^4 Hz
$10^4(\Delta\varepsilon/\varepsilon)$
0.01
0.1
1.0
10
T(K)

Figure 7. Measured variation of dielectric susceptibility as a function of temperature for Li beta-alumina. The solid lines are predicted using the LTS model. (Ref. 4 and 23)

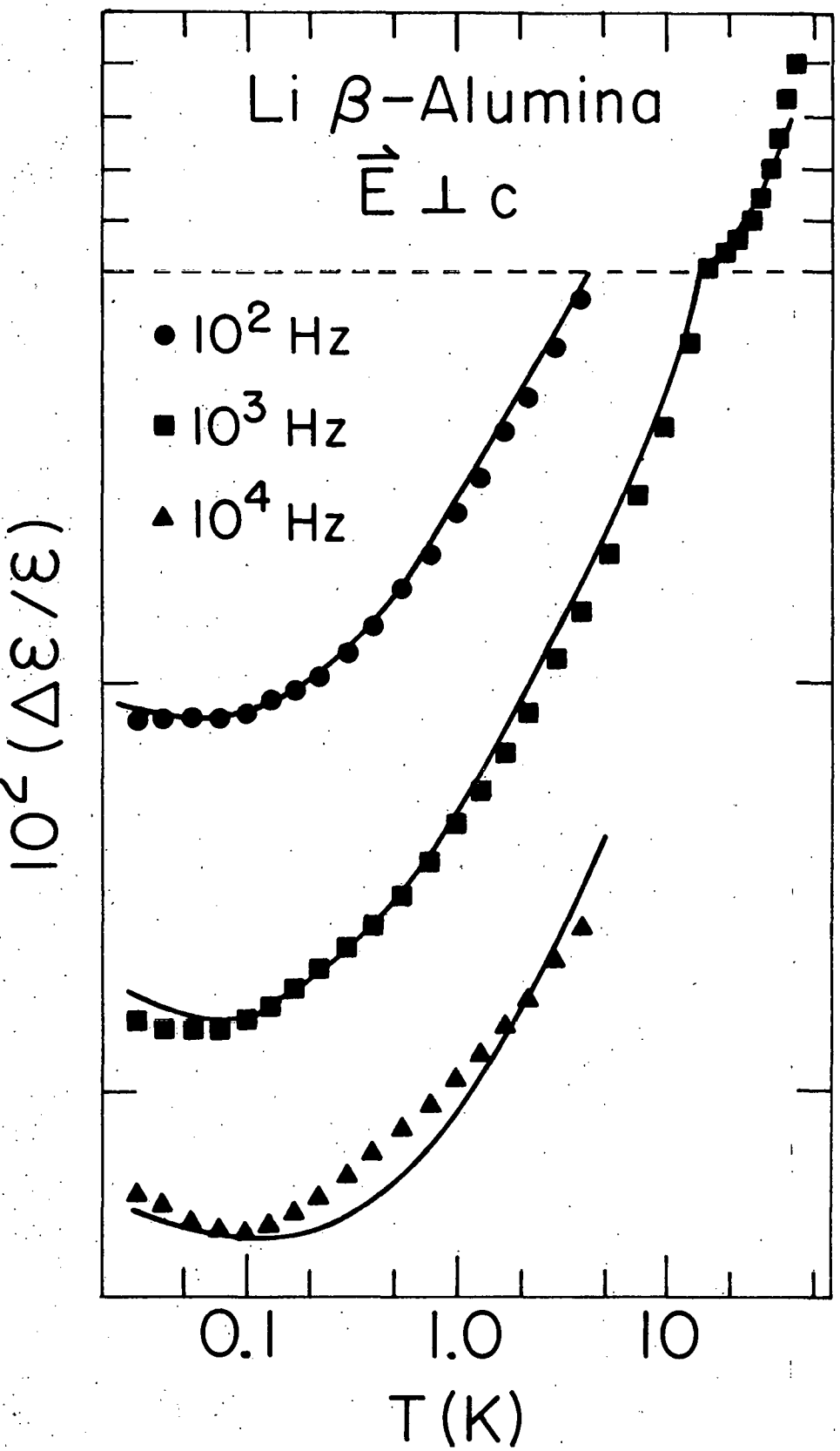
Li β-Alumina
$\vec{E} \perp c$
10^2 Hz
10^3 Hz
10^4 Hz
$10^2(\Delta\varepsilon/\varepsilon)$
0.1
1.0
10
T(K)

providing additional support for this idea. Estimates of the LTS dipole moment needed to predict the magnitude of the beta-alumina dielectric data indicate that the tunneling species only tunnels a distance $d \approx 0.1 - 1.0$ Å.[23,26] Therefore, the tunneling probably does not occur between the cation sites previously mentioned, a distance of ≈3 Å.

The most remarkable result of the specific heat, thermal conductivity, and dielectric susceptibility measurements in beta-alumina is that the magnitude and temperature dependence observed in each of these experiments can be predicted with approximately the same set of parameters describing the LTS system.[4,23] This fact supports the LTS model and the idea that all of these "anomalous" effects are caused by the same group of low energy excitations associated with the disorder. For each type of beta-alumina, a single parameterization was generated to fit the data, and the solid lines in Fig. 3-7 are the predictions of the LTS model using these parameterizations. The only exception was the LTS-phonon coupling used to predict the dielectric susceptibility was slightly different from the coupling which predicts the correct magnitude of the thermal conductivity. Since these two experiments probe different size energy splittings within the LTS system, it is not unreasonable to expect these couplings to be different.

As a consequence of these extensive low temperature measurements, beta-alumina is a well understood disordered material. It has been proven that beta-alumina behaves like a glass, and the data is in good agreement with predictions of the LTS model. These studies have produced quantitative descriptions of the LTS systems in several different types of beta-alumina, and evidence indicates that conduction plane cations are tunneling.

All of these factors combine to make beta-alumina a perfect system to investigate new phenomena related to disorder.

III. PRODUCTION AND IDENTIFICATION OF COLOR CENTERS IN BETA-ALUMINA

A. Sample Preparation and Irradiation Procedure

The samples used in this work were loaned to us by A. C. Anderson, and originally they were prepared and used by P. J. Anthony in his specific heat and thermal conductivity measurements. The single crystal Na beta-alumina was cut from a boule grown by Union Carbide, and the Li and K beta-alumina samples were made from Na beta-alumina by repeated ion exchange.[4] All samples were stored in an anhydrous environment, and as a further precaution, the Li beta-alumina was dehydrated before irradiation by heating to 300 C for 48 hours in a vacuum.

In order to study beta-alumina using EPR, it is necessary to introduce paramagnetic sites into the conduction plane. This can be done by substitution of Na^+ ions with transition metal ions[28] or by irradiation of the material to produce color centers. In this work only the latter technique has been tried using an electron accelerator. Other research groups have produced color centers in beta-alumina with UV, x-ray, and Cs or Co γ-ray irradiation.[29,30,31]

The electron irradiation was performed at 77 K in the irradiation chamber shown in Fig. 8. The samples could be removed without warming through a large quik-connect at the top of the chamber. With this feature, EPR measurements could be made on color centers that would bleach-out at higher temperatures. A 50 micron thick titanium foil was placed between the incident electron beam and the sample, scattering the electron beam

Figure 8. Sample chamber for electron irradiation. a, sample mounted on the sample holder in contact with the liquid nitrogen reservoir; b, titanium electron scattering foil; c, electrically isolated copper screen.

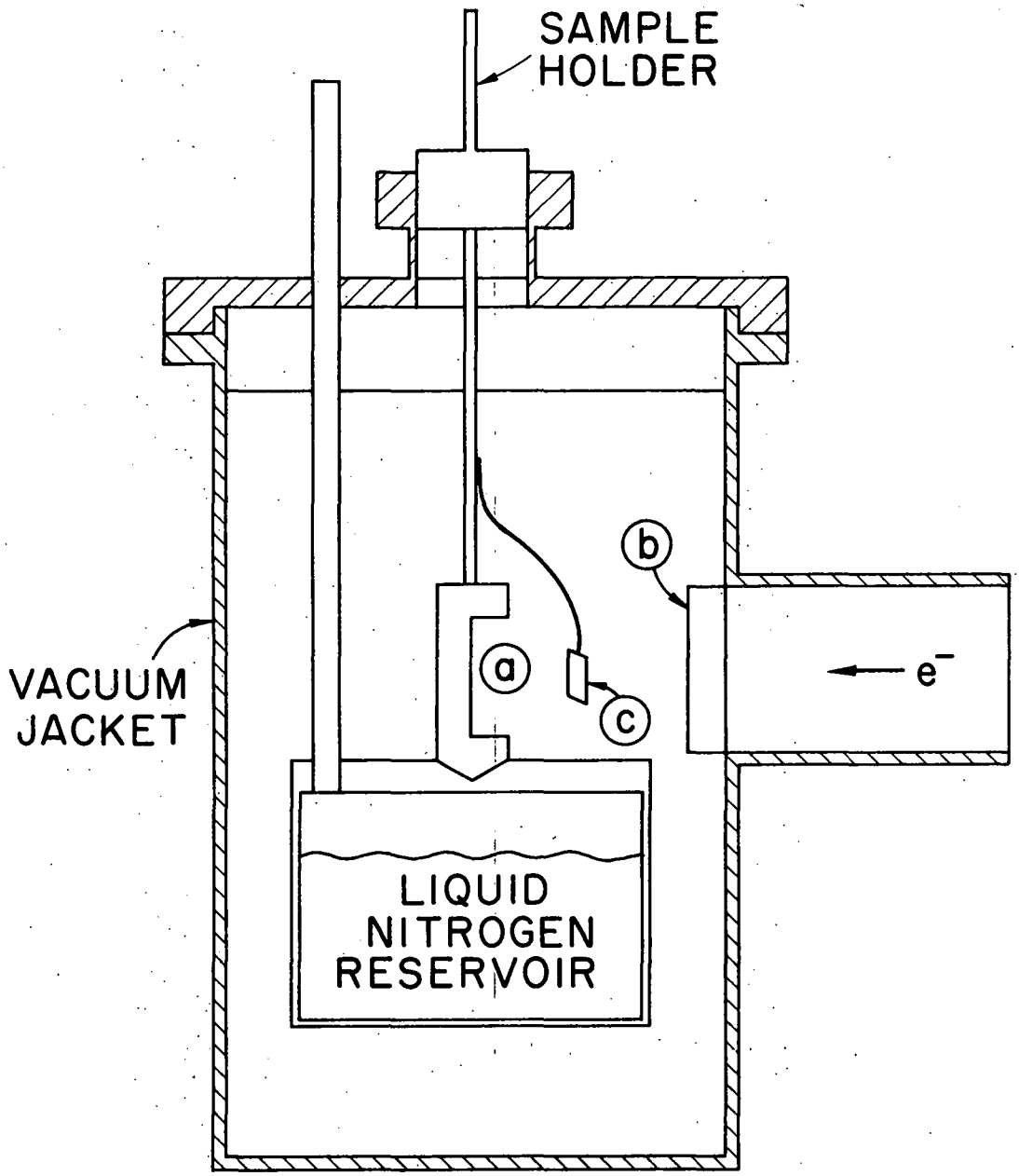
SAMPLE
HOLDER
VACUUM
JACKET
a
b
c
e⁻
LIQUID
NITROGEN
RESERVOIR

and producing bremsstrahlung x-rays. Without the scattering foil, the color center production was greatly decreased indicating the x-rays actually produce some of the observed color centers. The electron dose was typically 10^{13}-10^{14} electrons during an irradiation lasting about 5 minutes. This dosage was detected by a 1 cm^2 electrically isolated copper screen placed in front of the sample and connected to a current integrator.

The F^+ center was produced by irradiation with 1.5 MeV electrons. Without allowing these samples to warm-up, they exhibited a dark blue coloration and displayed the EPR spectrum of both the F^+ center and the center observed by Abraham and Stapleton (AS).[31] By warming irradiated Na beta-alumina or Li beta-alumina samples to room temperature in a dry box for a few minutes, the blue coloration was destroyed, and only the F^+ EPR remained. After this annealing, the Na and Li beta-alumina samples had a slight yellow-brown tint which appears to be characteristic of the F^+ center. For K beta-alumina, annealing at room temperature bleached both centers at about the same rate after several minutes.

Irradiation of Na beta-alumina at 0.75 MeV produced a sample with blue coloration, and only the EPR spectrum of the AS center was present. After warming to room temperature, the sample was clear and no EPR signal was observed suggesting the blue color is a characteristic of the AS center. This irradiation procedure has not been tried for other beta-aluminas, but it could offer a method for generating AS centers without creating F^+ centers.

In all types of beta-alumina where the F^+ center was observed, this center bleached slowly enough at room temperature to allow sample

loading into microwave cavities, thus permitting the F^+ center to be used in a variety of experiments. However, the rapid AS bleaching at room temperature has been an obstacle to an in depth study of the AS center. All samples could be stored indefinitely in liquid nitrogen without evidence of bleaching. Also, all these color centers could be destroyed by heating the beta-alumina in a vacuum for several hours at 200 C. This allows the same sample to be reused for several irradiations.

By irradiating Ag beta-alumina with 1.5 MeV electrons, the EPR of a color center tentatively identified as an Ag^{2+}[32] was observed. This sample was colored black, and the color and EPR signal were rapidly destroyed upon warming. Slower bleaching rates have been reported for samples with partial Ag^+ exchange with Na^+. Because F^+ and AS centers were not observed in Ag beta-alumina, this material was not included in later experiments.

B. EPR Spectrometer System

The EPR results shown in this thesis were obtained primarily from a homemade X-band (9.3 GHz) system. This apparatus was constructed for high sensitivity at 77 K, and it also permitted samples to be loaded and unloaded without warming them significantly above this temperature. Using this system, it was possible to observe color center EPR signals resulting from various irradiation procedures and monitor the bleaching of these centers after periods of annealing.

A block diagram of this apparatus is shown in Fig. 9. It utilizes homodyne signal detection with microwave bucking available through the bias arm. The klystron is stabilized by an automatic frequency controller

Figure 9. Schematic diagram of X-band (9.3 GHz) homodyne EPR spectrometer.

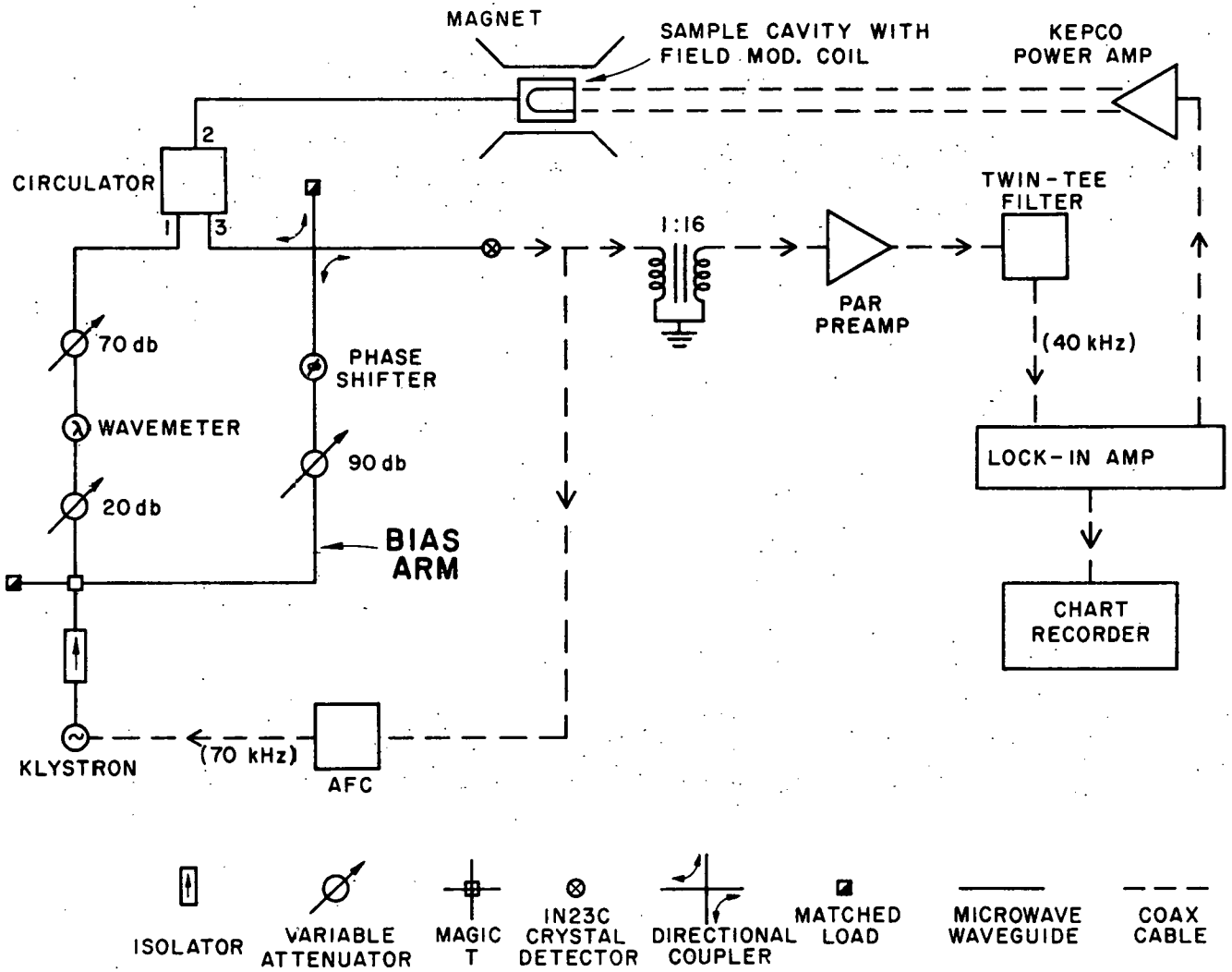
MAGNET
SAMPLE CAVITY WITH FIELD MOD. COIL
KEPCO POWER AMP
CIRCULATOR
2
1
3
1:16
PAR PREAMP
TWIN-TEE FILTER
(40 kHz)
70 db
PHASE SHIFTER
WAVEMETER
90 db
20 db
BIAS ARM
LOCK-IN AMP
CHART RECORDER
KLYSTRON
(70 kHz)
AFC
ISOLATOR
VARIABLE ATTENUATOR
MAGIC T
IN23C CRYSTAL DETECTOR
DIRECTIONAL COUPLER
MATCHED LOAD
MICROWAVE WAVEGUIDE
COAX CABLE

(AFC) operating at 70 kHz and locked to the sample cavity. Microwave frequency was measured with either a wavemeter or a microwave frequency counter, and a rotating coil gaussmeter calibrated to the DPPH resonance was used to measure the magnetic field.

To increase the signal to noise, the EPR signal was detected using high frequency magnetic field modulation. A power amplifier was connected to a coil inside the microwave cavity generating 40 kHz, 4 gauss peak to peak modulation at the sample. This 40 kHz signal was detected by a lock-in amplifier producing a derivative of the EPR absorption spectrum. An impedance matching transformer was inserted between the crystal detector and the PAR preamp, and a narrow-band filter prevented the 70 kHz AFC signal from saturating the lock-in.

The microwave cavity used in this experiment was a cylindrical TE_{011} cavity (see Figure 10). This mode was chosen because its shape is convenient for sample loading and reorientation, and coils can be inserted parallel to the cylindrical axis without spoiling the cavity Q. A quartz tube extending the length of the cavity was inserted along the cavity axis, and cold nitrogen gas was blown through the tube to cool the sample. The sample was positioned inside the tube, at the center of the cavity, and it was mounted on a teflon or white delrin sample holder. The sample and its sample holder could be loaded and manually rotated from above the cavity. The field modulation coil consisted of a pair of 1/16" diameter brass rods connected together to form a one turn coil. This coil design was superior to others that were tried because the brass rods were rigid enough to be immune to $\vec{I} \times \vec{H}_o$ vibration while providing adequate modulation.

Figure 10. A TE_{011} sample cavity showing the position of metal rods inside the cavity and the geometry of the microwave magnetic field, $\vec{H}'$, for this mode.

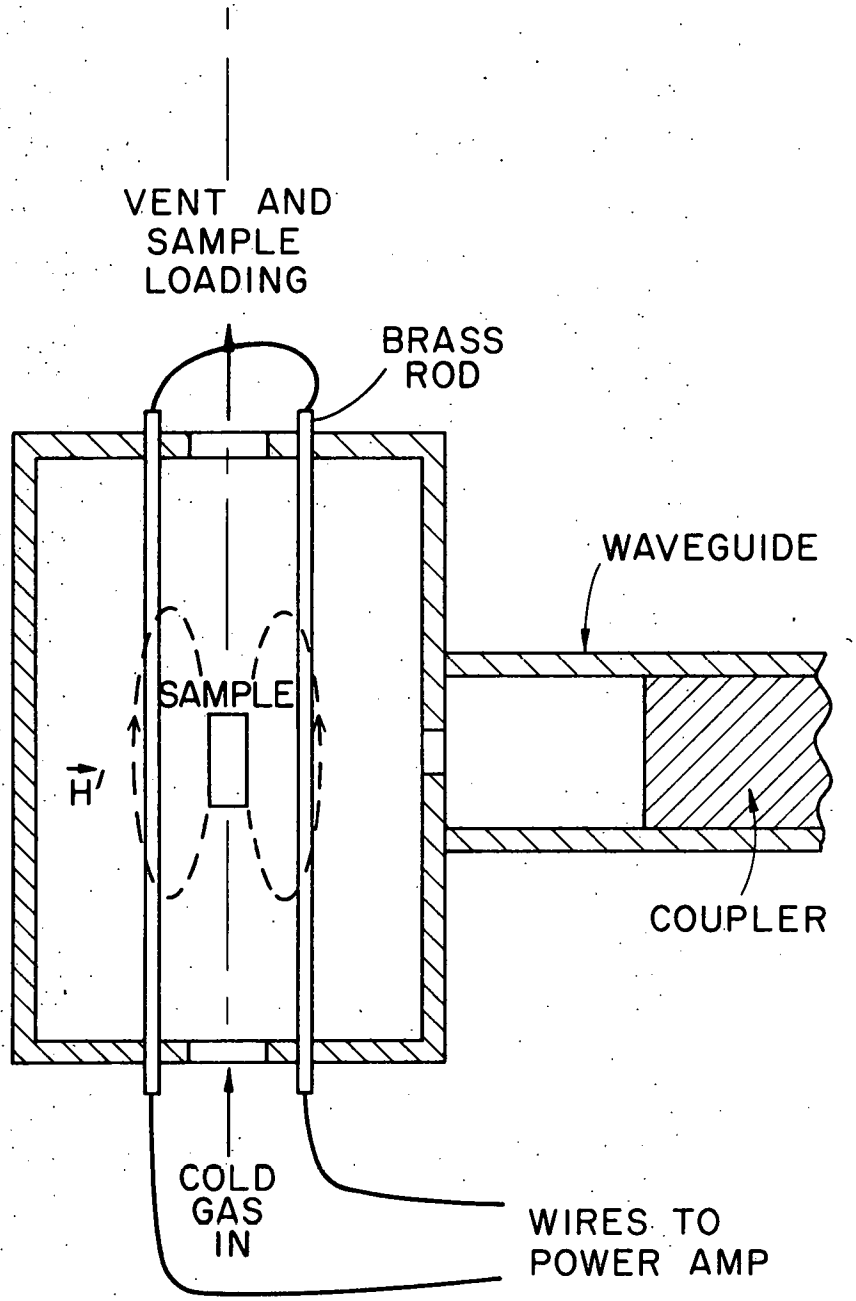
VENT AND
SAMPLE
LOADING
BRASS
ROD
WAVEGUIDE
SAMPLE
H
COUPLER
COLD
GAS
IN
WIRES TO
POWER AMP

Except for the interior of the quartz tube, the entire cavity and coupler assembly was contained in a vacuum to maintain thermal stability. The coupler consisted of movable teflon plugs that could be adjusted to provide the desired matching of cavity and waveguide.

C. ENDOR Spectrometer System

Electron nuclear double resonance (ENDOR) is a technique for detecting nuclear spin transitions through their coupling to the paramagnetic spin system. Under the proper conditions, saturation of an EPR line will partially polarize nuclei, and conversely, if the resonance condition of these polarized nuclei is suddenly satisfied, it causes a change in the paramagnetic spin populations, altering the EPR absorption. So in practice, ENDOR is carried out while partially saturating an EPR line and sitting at a constant value of the magnetic field. By monitoring the weak EPR signal and simultaneously sweeping in frequency through a nuclear magnetic resonance, a response in the EPR signal is observed when the nuclear resonance condition is satisfied. Through this process, the nuclear resonance signal is greatly enhanced over standard NMR techniques, and lines of width $\gtrsim$ 10 kHz can be resolved making it often possible to measure hyperfine interactions with greater accuracy than can be obtained using EPR.[33]

An ENDOR experiment basically consists of a sensitive EPR apparatus with the addition of a radio frequency (RF) coil around the sample and a RF generator and amplifier to drive the coil. For increased sensitivity and to make saturation of the EPR line easier, the ENDOR measurements in

this thesis were made at liquid helium temperature. At this temperature, saturation occurs at low microwave power levels, and for this reason superheterodyne detection (see Fig. 11) was used instead of the homodyne technique mentioned in Section B. As before, the AFC was locked to the sample cavity.

In this experiment the LSI-11 microcomputer functions as a signal averager and controls the frequency sweep of the RF coil. The frequency produced by the RF oscillator is proportional to the output voltage of the D:A converter. ENDOR data is collected during a RF sweep by stepping the output of the D:A, and after each step monitoring the EPR signal with the A:D. Using this system, an up-sweep was always followed by an identical down-sweep which eliminated ENDOR lineshape distortion sometimes caused by using one sweep direction. After the signal averaging was completed, the frequency at each point on the resulting ENDOR spectrum was measured using a frequency counter connected to the LSI-11 via an IEEE BUS. The data was then transferred to a floppy disc for further analysis.

The most formidable problem encountered when building an ENDOR experiment is to introduce a sufficient RF field at the sample while maintaining a high cavity Q. This problem was solved by using a cylindrical TE_{011} cavity similar to the one shown in Fig. 10. The ENDOR cavity was immersed in liquid helium pumped below the lambda point, and because of dewar size limitations, it operated at Ku-band (15.0 GHz). The sample loading and positioning remained the same as that used in the X-band EPR cavity.

The RF coil consisted of two "rods" positioned at the same place in the cavity as the brass rods in Fig. 10. Each "rod" was made from a

Figure 11. A block diagram of Ku-band (15.0 GHz) superheterodyne ENDOR spectrometer.

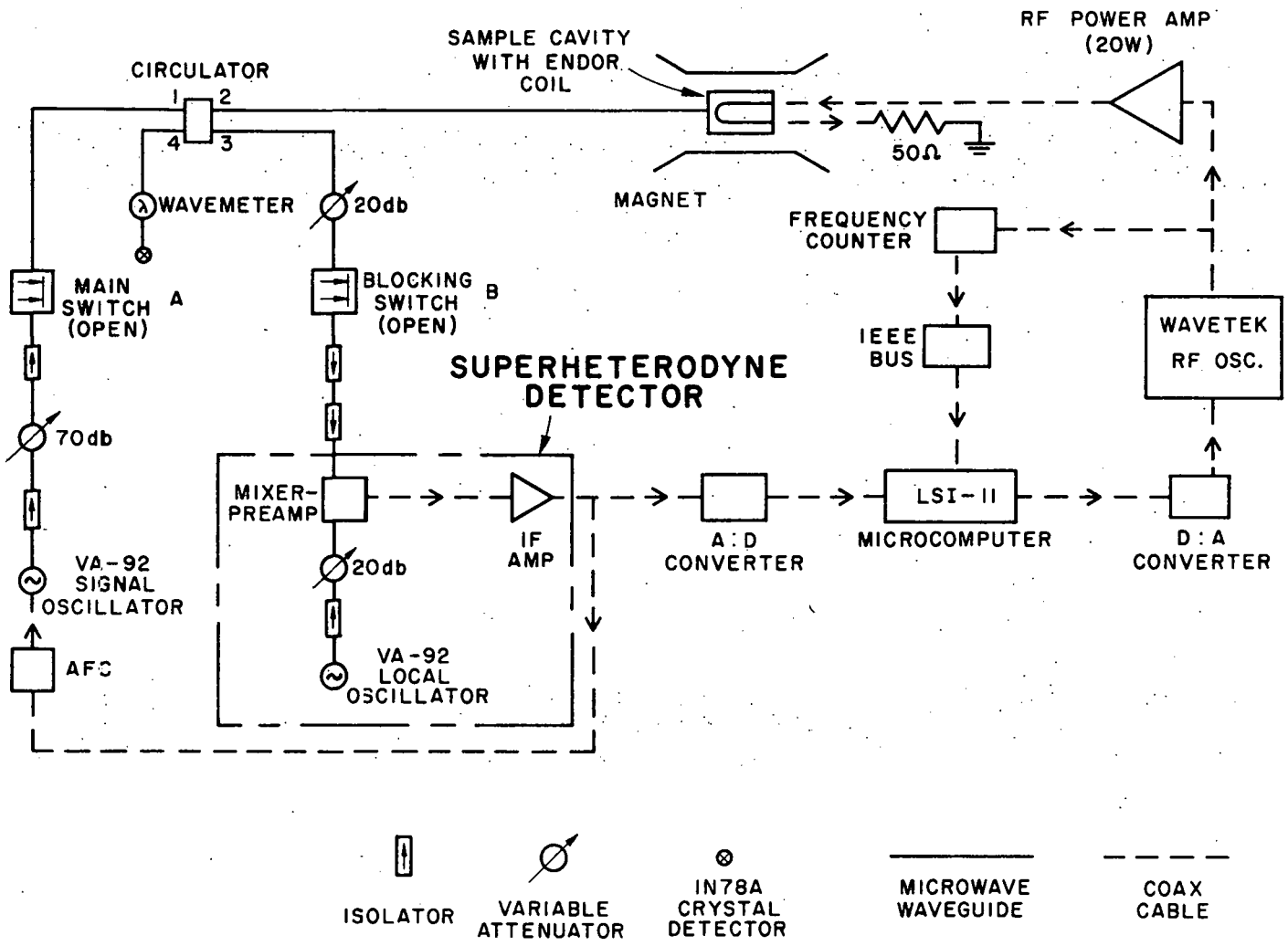
SAMPLE CAVITY
WITH ENDOR
COIL
RF POWER AMP
(20W)
CIRCULATOR
1
2
4
3
50Ω
WAVEMETER
20db
MAGNET
FREQUENCY
COUNTER
MAIN
SWITCH
(OPEN)
A
BLOCKING
SWITCH
(OPEN)
B
IEEE
BUS
WAVETEK
RF OSC.
SUPERHETERODYNE
DETECTOR
70db
MIXER-
PREAMP
IF
AMP
A:D
CONVERTER
LSI-11
MICROCOMPUTER
D:A
CONVERTER
VA-92
SIGNAL
OSCILLATOR
20db
AFC
VA-92
LOCAL
OSCILLATOR
ISOLATOR
VARIABLE
ATTENUATOR
IN78A
CRYSTAL
DETECTOR
MICROWAVE
WAVEGUIDE
COAX
CABLE

thin copper tube which was stripped from 0.035" diameter Coaxitube, and 3 strands of Formvar coated 32 gauge copper wire were encapsulated inside each copper tube using Stycast 1266 epoxy. These "rods" were then placed in the cavity, and the wires were soldered together to form a 3 turn RF coil. Coils constructed in this manner were resistant to vibrations and thermal stress, and they worked well over a 1-40 MHz frequency range. This cavity had a Q ≈ 8000, and the intensity of the RF field at the sample was a factor of 10 greater than that achieved with a slotted cavity-coil design having comparable bandwidth.[34]

D. Spin Hamiltonian Formalism

In order to interpret EPR or ENDOR results, it is necessary to fit the data with a spin Hamiltonian. The terms contained within this spin Hamiltonian describe the interactions of an electronic or nuclear spin with its environment, and evaluation of spin Hamiltonian parameters reveals valuable information about the identity and location of a spin within a material. This section marks the beginning of this process with an introduction to the particular Hamiltonian used to analyze the color center EPR and ENDOR data in beta-alumina. For convenience, the interactions observed in the EPR experiments are discussed first, followed by a qualitative description of their origin. Afterward, the interactions observed through ENDOR spectra are presented in the same manner. Further quantitative analysis of the spin Hamiltonian occurs in a later section after the EPR and ENDOR results are presented.

The spin Hamiltonian required to explain the color center EPR data for beta-alumina has the form:

$$H = \mu_B \vec{S}\cdot\tilde{\tilde{g}}\cdot\vec{H}_o + \sum_i \vec{S}\cdot\tilde{\tilde{A}}_i\cdot\vec{I}_i \quad . \tag{7}$$

The first term is the electronic Zeeman energy where μ_B is the Bohr magneton, $\vec{H}_o$ is the applied magnetic field, and $\tilde{\tilde{g}}$ is the electronic g tensor. The second term is the ligand hyperfine interaction with the summation extending over the ligand nuclei. Terms resulting from weaker interactions have not been included at this point because the resolution of the EPR data makes it impossible to observe these smaller effects. This discussion is limited to S=1/2 centers which eliminates fine structure terms.[35]

The Zeeman energy in Equation (7) originates from the Hamiltonian

$$H_z = \mu_B(\vec{L} + g_e\vec{S})\cdot\vec{H}_o \quad , \tag{8}$$

and in the spin Hamiltonian approach, this transforms into

$$H_z = \mu_B \vec{S}\cdot\tilde{\tilde{g}}\cdot\vec{H}_o = \mu_B g H_o S_z \tag{9}$$

where $\tilde{\tilde{g}}\cdot\vec{H}_o$ points along the z axis, and g is referred to as the g factor. For most color centers, g differs little from the free electron g factor, $g_e = 2.0023$, but valuable information about the structure of the centers comes from these small g shifts and their anisotropy. The spin-orbit interaction admixes crystal field wave functions and produces a contribution to $\tilde{\tilde{g}}$ from the $\vec{L}$ operator of Eq. (8). This causes g to deviate from g_e, and the magnitude of the deviation is indicative of the L character of the color center wave function. In the absence of the spin-orbit interaction, angular momentum is "quenched."[36] Also, the local symmetry of

the color center is reflected in the symmetry of $\tilde{\tilde{g}}$ through this same perturbation scheme.[36,37]

The hyperfine term originates from two main sources, the Fermi contact interaction and the dipole-dipole interaction between nuclear and electron spins. The contact term is isotropic and has the form

$$H_c = a\vec{S}\cdot\vec{I} \quad , \tag{10}$$

with

$$a = \frac{8\pi}{3} g\, g_n\, \mu_B^2\, |\psi(o)|^2 \quad . \tag{11}$$

The nuclear g factor of the ligand nucleus is g_n, and $|\psi(o)|^2$ is the electron density of the unpaired spin at the ligand nucleus. For convenience, g_n is written in units of μ_B, and it is of order μ_N/μ_B where μ_N is the nuclear magneton. The anisotropic part of the hyperfine interaction primarily results from the dipolar interaction

$$H_D = \frac{\vec{\mu}_1\cdot\vec{\mu}_2}{r^3} - 3\frac{(\vec{\mu}_1\cdot\vec{r})(\vec{\mu}_2\cdot\vec{r})}{r^5} \tag{12}$$

integrated over the color center wave function. This produces a hyperfine interaction with axial symmetry about the bond direction such that

$$\tilde{\tilde{A}} = \begin{pmatrix} (a-b)_{x'x'} & 0 & \\ & (a-b)_{y'y'} & \\ 0 & & (a+2b)_{z'z'} \end{pmatrix} \tag{13}$$

where the z' axis is the color center-ligand bond axis. If the color center also has axial symmetry about z', b may be written as

$$b = \frac{1}{2} g\, g_n\, \mu_B^2 \left\langle\psi\left|\frac{(3\cos^2\alpha-1)}{r^3}\right|\psi\right\rangle \tag{14}$$

where α is the angle between $\vec{r}$ and the symmetry axis z'.[38] For practical purposes, this treatment of the hyperfine interaction is usually adequate, but other contributions resulting from corrections to the electronic wave function and $\vec{L}\cdot\vec{I}$ coupling can cause small deviations from the simple form of Eq. (13).[39,40,41]

A frequently encountered problem is the solution to the spin Hamiltonian when $\tilde{\tilde{g}}$ and $\tilde{\tilde{A}}$ have axial symmetry about the same symmetry axis. For this case,

$$\tilde{\tilde{g}} = \begin{pmatrix} g_{\perp} & & 0 \\ & g_{\perp} & \\ 0 & & g_{\parallel} \end{pmatrix} , \qquad (15)$$

and $\tilde{\tilde{A}}$ remains unchanged from Eq. (13). For a color center, $g_{\perp} \simeq g_{\parallel}$, and a large resolvable hyperfine splitting generally indicates a>>b. Under these conditions, Eq. (7) becomes

$$H = g\mu_B H_o S_z + [a + b(3\cos^2\theta - 1) + 0\left(\frac{b^2}{a}\right) + \ldots]S_z I_z \qquad (16)$$

for a single ligand nucleus. The angle between the direction of the applied $\vec{H}_o$ field and the symmetry axis is θ, and

$$g = \left(g_{\parallel}^2 \cos^2\theta + g_{\perp}^2 \sin^2\theta\right)^{\frac{1}{2}} . \qquad (17)$$

For an allowed electron spin transition ($\Delta M_S = \pm 1$, $\Delta m_I = 0$), the resonance condition for this Hamiltonian is

$$h\nu = g\mu_B H_o + [a + b(3\cos^2\theta - 1)]\, m_I , \qquad (18)$$

where m_I is the nuclear spin quantum number. This spin Hamiltonian predicts 2I + 1 equally spaced EPR lines. The position of the center of the group of 2I + 1 lines shifts as a function of θ depending on g, and the

splitting between adjacent lines changes with θ depending on the size of b.[33,38]

Using ENDOR, it is possible to observe several interactions which are not resolvable from EPR data. Including these extra terms in the spin Hamiltonian, one obtains

$$H = \mu_B \vec{S}\cdot\tilde{\tilde{g}}\cdot\vec{H}_o + \sum_i \left[\vec{S}\cdot\tilde{\tilde{A}}_i\cdot\vec{I}_i - g_i \mu_B \vec{I}_i\cdot\vec{H}_o + \vec{I}_i\cdot\tilde{\tilde{P}}_i\cdot\vec{I}_i\right] \qquad (19)$$

where the nuclear Zeeman energy and nuclear quadrupole interaction have been added for each ligand nuclei.

The nuclear quadrupole interaction couples the nuclear electric quadrupole moment to the electric field gradient at the ligand nucleus. The quadrupole tensor, $\tilde{\tilde{P}}$, is defined as

$$P_{ij} = \frac{eQ}{2I(2I+1)} \frac{\partial^2\Phi}{\partial x_i \partial x_j} \qquad (20)$$

where Φ is the electrostatic potential, and Q is the nuclear quadrupole moment. From Laplace's equation, the trace of $\tilde{\tilde{P}}$ is equal to zero. In the principal axis system of $\tilde{\tilde{P}}$, the quadrupole contribution to the Hamiltonian can be written as[36]

$$H_Q = \frac{1}{2}\left[P_{z'z'}\left(3I_{z'}^2 - I(I+1)\right) + \left(P_{x'x'} - P_{y'y'}\right)\left(I_{x'}^2 - I_{y'}^2\right)\right] . \qquad (21)$$

It is now possible to obtain the energy levels of this new spin Hamiltonian containing the additional terms. As before, $\tilde{\tilde{g}}$ and $\tilde{\tilde{A}}$ have the same axial symmetry and are almost isotropic, and since the symmetry of the crystal field at the nucleus determines the symmetry of $\tilde{\tilde{P}}$, it is consistent to assume $\tilde{\tilde{P}}$ also has axial symmetry with the same symmetry

axis. For this case, Eq. (19) becomes

$$H = g\mu_B H_o S_z + [a + b(3\cos^2\theta - 1)] S_z I_z - g_n \mu_B H_o I_z + \frac{P_{||}}{2}\left[I_z^2 - \frac{I(I+1)}{3}\right](3\cos^2\theta - 1) \qquad (22)$$

where only one ligand nucleus is being considered, and $P_{||} = 3/2\ P_{z'z'}$. Using this equation, the ENDOR resonance condition ($\Delta M_S = 0$, $\Delta m_I = \pm 1$) is easily obtained

$$h\nu = \left|[a + b(3\cos^2\theta - 1)]M_S - g_n \mu_B H_o + P_{||}\, m_I (3\cos^2\theta - 1)\right| \qquad (23)$$

for $-I \leq m_I \leq I-1$.

The nuclei observed through ENDOR spectra can be divided into two catagories, "near" and "distant" nuclei. A near nucleus is any nucleus with a nonnegligible hyperfine interaction with the color center. Assuming S=1/2, Eq. (23) predicts that the ENDOR spectrum of a near nucleus will display two ($M_S = \pm 1/2$) main groups of lines. The frequencies at which these two clusters appear depends on the relative size of $[a + b(3\cos^2\theta - 1)]$ and $g_n \mu_B H_o$. Each cluster is composed of 2I equally spaced ENDOR lines resulting from the quadrupole splitting. A distant nucleus has a negligible hyperfine interaction and displays an ENDOR spectrum consisting of a single group of 2I quadrupole lines centered at the nuclear Zeeman frequency as predicted by Eq. (23).

Although these solutions to the spin Hamiltonian appear very specialized, they actually provide a strong foundation for interpreting a wide range of color center EPR and ENDOR data. As long as $\tilde{\tilde{g}}$ and $\tilde{\tilde{A}}$ are highly isotropic, $\vec{S}$ and $\vec{I}$ are quantized in the direction of $\vec{H}_o$ to a first

approximation. Under these conditions, it is possible to modify Eq. (18) and (23) when $\tilde{\tilde{g}}$, $\tilde{\tilde{A}}$, and $\tilde{\tilde{P}}$ have differing symmetry axes and still describe the anisotropy of these tensors rather simply. Based on this treatment of the spin Hamiltonian, EPR and ENDOR results are used to evaluate spin Hamiltonian parameters in the following sections.

E. EPR and ENDOR of the F^+ Center

Color centers identified as F^+ centers are observed in Na, K, and Li beta-alumina through EPR and ENDOR spectra. In this section, data on the F^+ center is presented and summarized. For each material, the EPR and ENDOR results are discussed interchangably because these techniques complement each other, and their data should be self-consistent. At the end of the section, the identification process for the F^+ center is reviewed.

1. Na Beta-Alumina Results

As described earlier, irradiation of Na beta-alumina at 1.5 MeV followed by room temperature annealing for a few minutes produced a single color center. The EPR spectrum of this center is shown in Fig. 12. This center is characterized by an eleven line hyperfine pattern with an intensity ratio 1:2:3:4:5:6:5:4:3:2:1. Both the $\tilde{\tilde{g}}$ and $\tilde{\tilde{A}}$ tensors were nearly isotropic and possessed axial symmetry about the crystalline c axis.

Assuming a color center interacts with 2 equivalent ligand nuclei, Eq. (18) becomes

$$h\nu = g\mu_B H_o + [a + b(3\cos^2\theta - 1)]\,(m_1 + m_2) \qquad (24)$$

Figure 12. Derivative of the EPR spectrum of an F^+ center in the conduction plane of Na beta-alumina as measured at 77 K and 9.3 GHz, with $\vec{H}_o$ parallel to the c axis. A similar EPR spectrum appears in K beta-alumina.

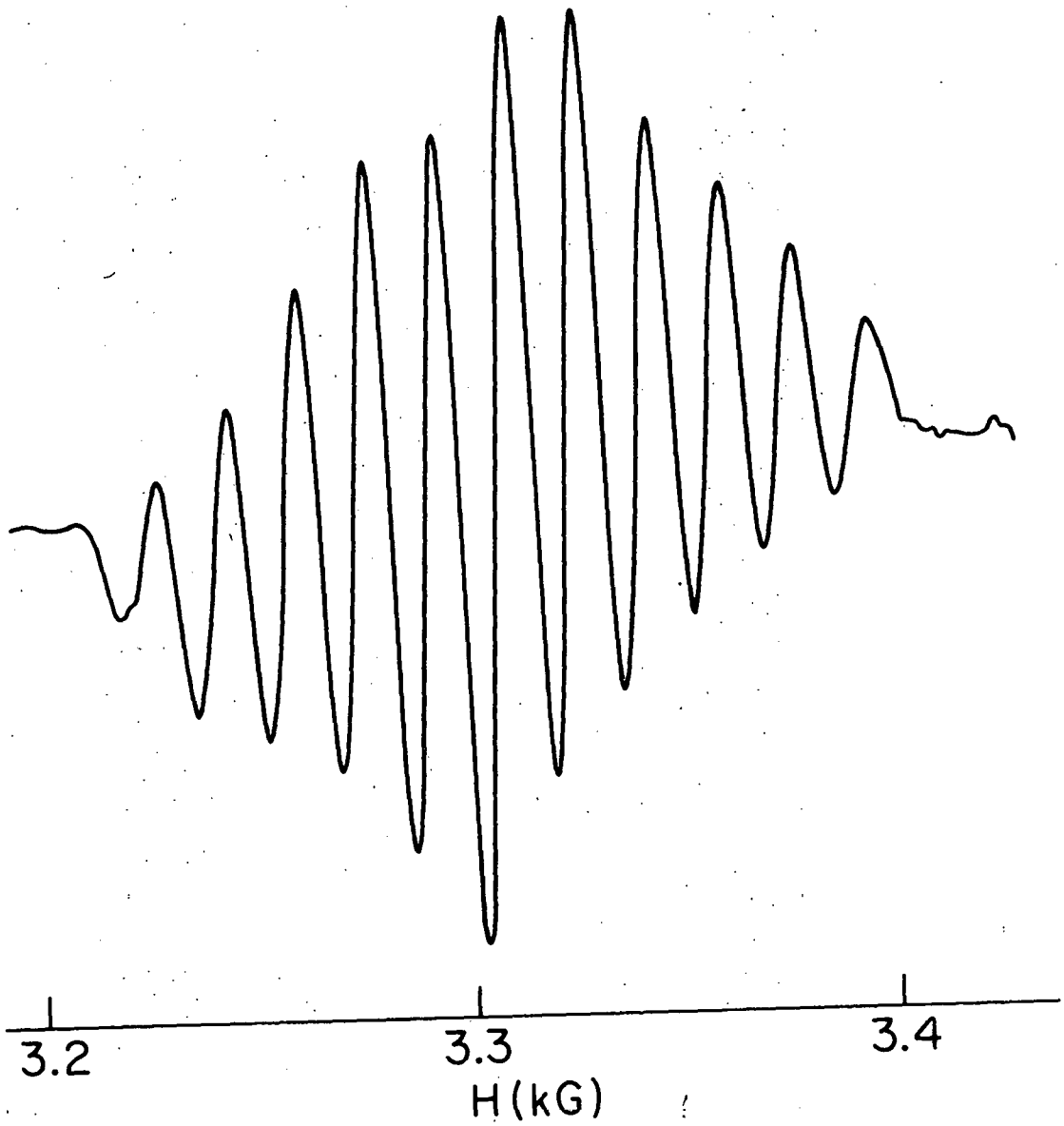
3.2
3.3
3.4
H(kG)

where m_1 and m_2 are the nuclear spin quantum numbers for each of the equivalent nuclei. For $I_1 = I_2 = 5/2$, an 11 line pattern with the proper intensities is predicted by this expression. Since aluminum is the only abundant nucleus in Na beta-alumina with a spin of 5/2, the EPR spectrum indicates that the color center is adjacent to 2 equivalent ^{27}Al nuclei, and the bond direction for each of these ligands is the c axis. When $\vec{H}_o$ is rotated, Eq. (24) describes the EPR data with $g_{||} = 2.0079(5)$, $g_{\perp} = 2.0039(5)$, $A_{||} = (a + 2b)/(g_{||}\mu_B) = 16.8(2)$ gauss, and $A_{\perp} = (a - b)/(g_{\perp}\mu_B) = 16.3(2)$ gauss. These results are in good agreement with the data of other researchers who independently observed this center in Na beta-alumina.[29,30]

The F^+ center concentration was determined by comparing the intensity of the F^+ EPR signal with the signal produced by a MgO sample doped with a known concentration of Cr^{3+}. (The MgO:Cr^{3+} sample was provided by M. M. Abraham.) This measurement indicated that the irradiation procedure produced $\sim 10^{17}$-10^{18} F^+/cm^3 in Na beta-alumina, and longer irradiations did not visibly increase the color center concentration suggesting the electron irradiation does not generate knock-on lattice defects.

ENDOR spectra of the F^+ center were obtained by saturating the center line of the EPR spectrum at $\sim$1.8 K. These spectra revealed several different peaks in the 2-35 MHz range which could be identified as near Al, near Na, and distant Al ligands. Saturation of different EPR lines did not significantly change the ENDOR spectra indicating that all of these ENDOR lines belong to the same defect, but saturation of different hyperfine lines produced slight changes in the ENDOR lineshape due to the complex nuclear polarization process. Also, it must be noted that beta-alumina

displayed unusually broad ENDOR lines caused by the conduction plane disorder. This inhomogeneous broadening limited the amount of information that was provided by the ENDOR measurements.

The two equivalent Al nuclei that produce the EPR hyperfine structure were observed in the ENDOR data. This near Al ENDOR spectrum shown in Figure 13 consists of two broad peaks. These peaks are separated by $2g_{Al}\mu_B H_o$, and they are centered around A/2. A fit of the hyperfine interaction (see Fig. 14) produced a = 45.7(1) MHz and b = 1.0(1) MHz, in agreement with the $A_{||}$ and $A_{\perp}$ values obtained from the EPR data. Each broad Al peak consisted of 5 quadrupole peaks with splittings described by a $\tilde{P}$ with axial symmetry along the c axis; $P_{||}$ = 0.35(6) MHz. Na^+ disorder should create a deviation from axial symmetry in $\tilde{P}$,[42] but this effect could not be observed due to poor resolution.

A broad structureless ENDOR line identified as a near ^{23}Na resonance is located around 10 MHz as shown in Figure 15. The relative sizes of the hyperfine and nuclear Zeeman interactions are such that Eq. (23) predicts a near Na ENDOR spectrum consisting of 2 broad lines centered at $g_{Na}\mu_B H_o$ ($g_{Na} \simeq g_{Al}$). The separation between the lines is equal to A. Only the 10 MHz line is observed because the other Na peak occurs at a frequency too low to permit the line to be resolved. The observed shift of the Na line with magnetic field direction indicates that the Na - color center bond direction is perpendicular to the c axis. Averaging over the Na bond direction within the conduction plane, this hyperfine interaction is approximately described by[43]

$$\vec{S}\cdot\tilde{A}_{Na}\cdot\vec{I} = \left[a + \frac{b}{2}\,(3\sin^2\theta - 2)\right] S_z I_z \qquad (25)$$

Figure 13. ENDOR spectrum of near Al nuclei in Na beta-alumina. H_o = 5346 gauss, f_o = 15.02 GHz, and $\vec{H}_o \| c$. The five line quadrupole structure is indicated for one of the peaks.

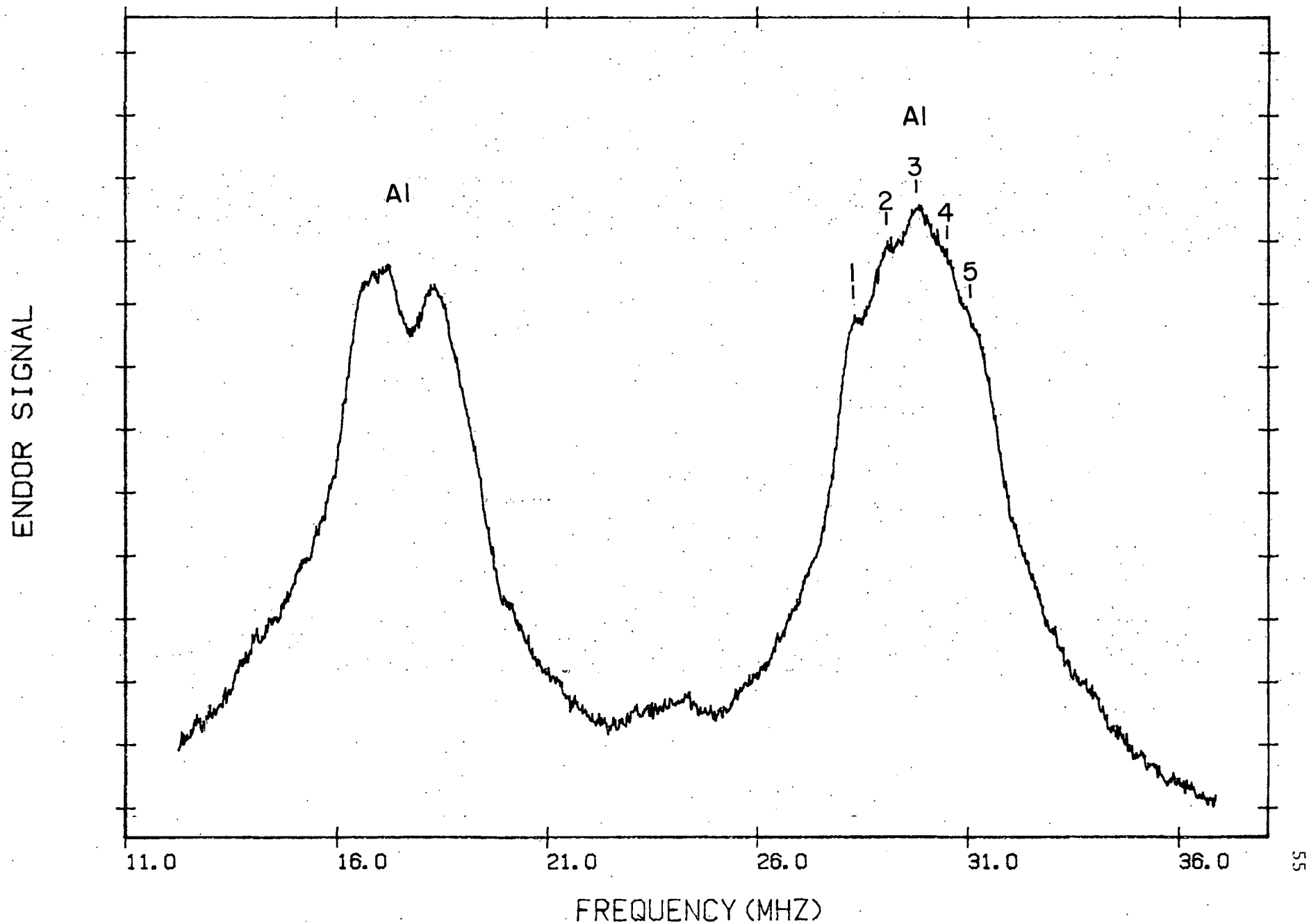
ENDOR SIGNAL
Al
Al
1
2
3
4
5
11.0
16.0
21.0
26.0
31.0
36.0
FREQUENCY (MHZ)

Figure 14. ENDOR data for the F^+ - Al hyperfine interaction in Na beta-alumina as a function of the direction of the applied magnetic field. The solid line is a fit to an $\tilde{\tilde{A}}$ with the form of Eq. (13) of the text.

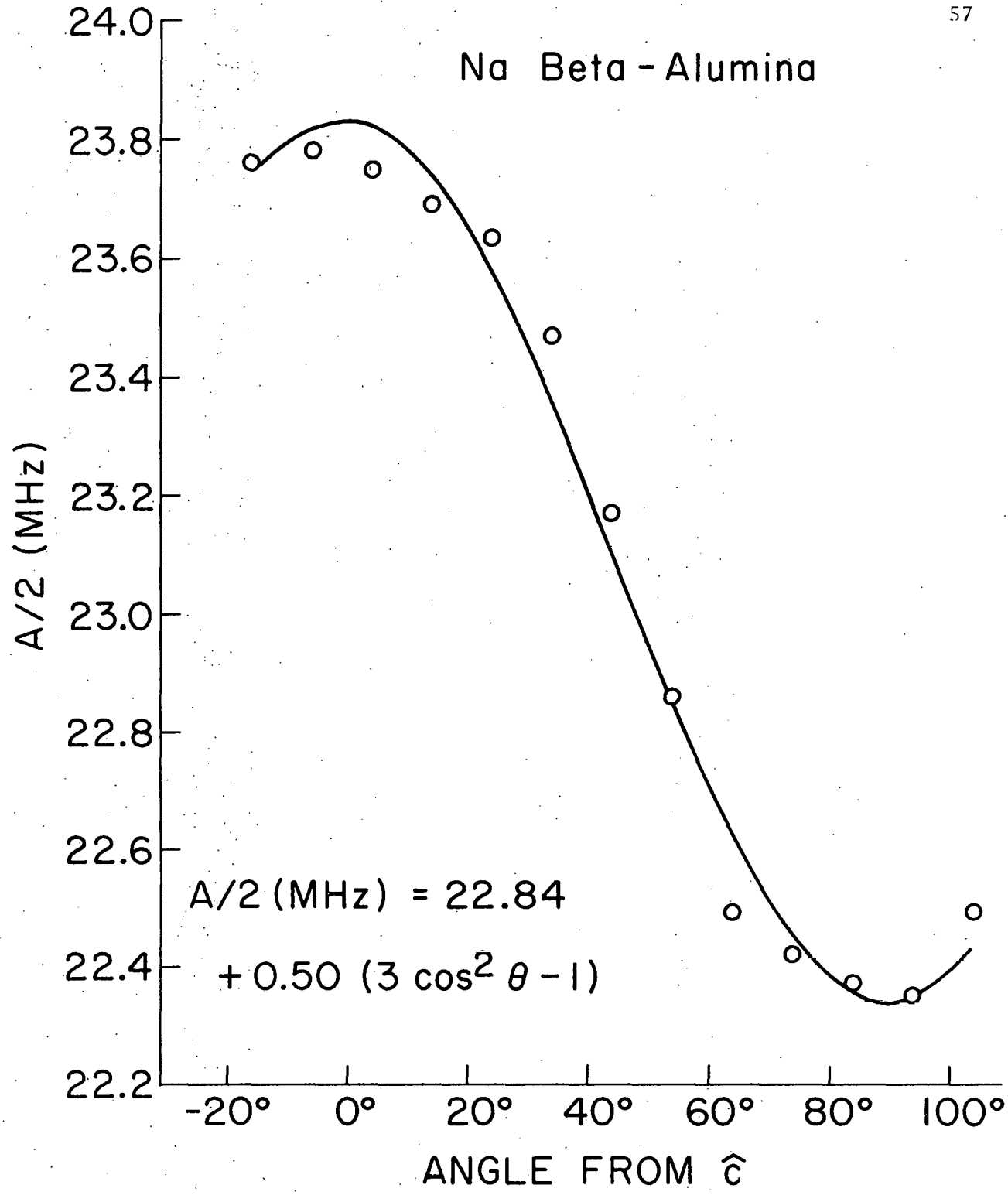
Na Beta - Alumina
24.0
23.8
23.6
23.4
23.2
23.0
22.8
22.6
22.4
22.2
A/2 (MHz)
A/2 (MHz) = 22.84
+ 0.50 (3 cos² θ - 1)
-20°
0°
20°
40°
60°
80°
100°
ANGLE FROM ĉ

Figure 15. Low frequency ENDOR spectrum of Na beta-alumina. H_o = 5346 gauss, f_o = 15.02 GHz, and $\vec{H}_o \| c$. The broad near Na line is shown along with the distant Al spectrum.

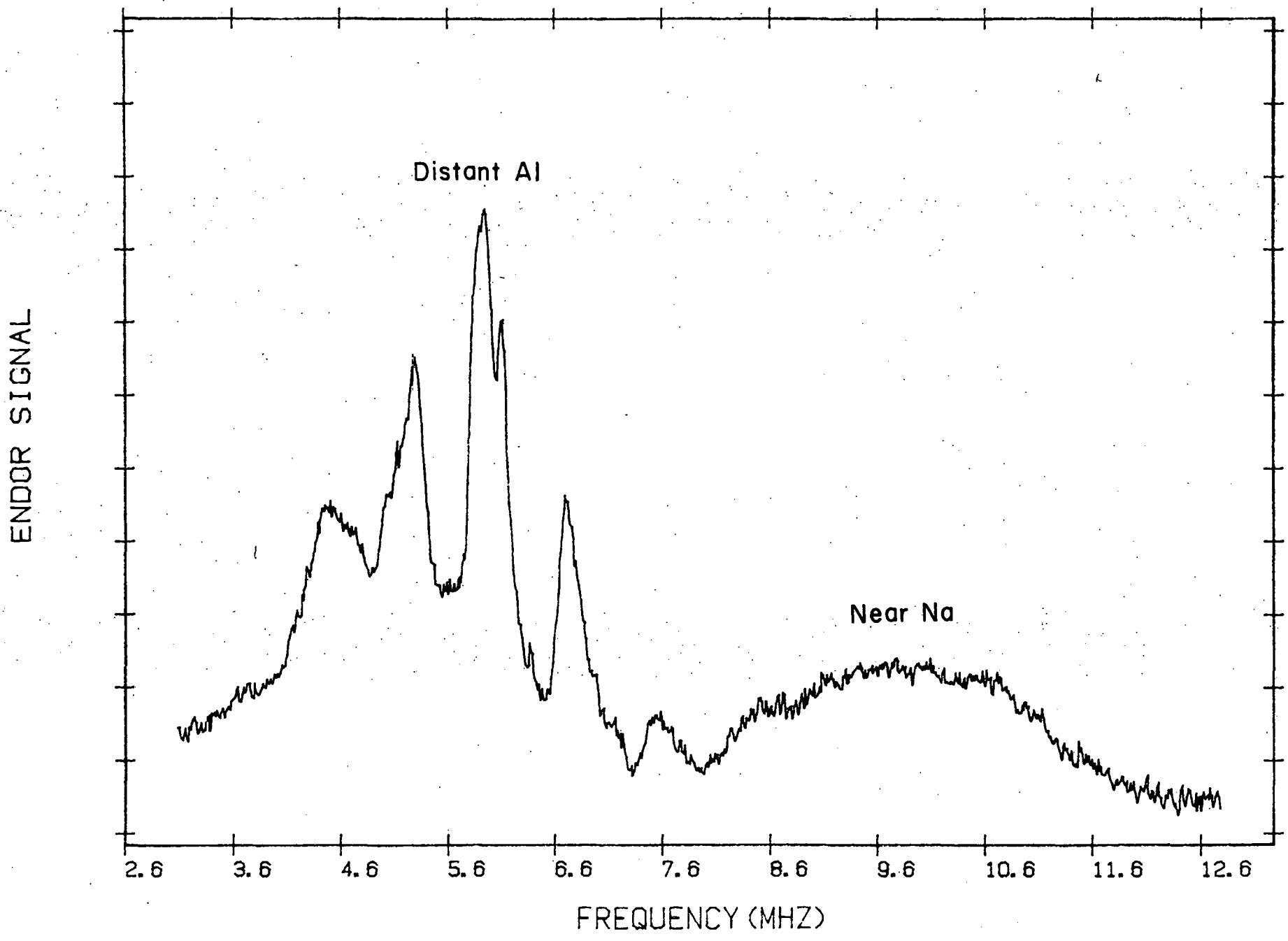
Distant Al
Near Na
ENDOR SIGNAL
2.6
3.6
4.6
5.6
6.6
7.6
8.6
9.6
10.6
11.6
12.6
FREQUENCY (MHZ)

with a = 9.5(3) MHz and b = 1.5(3) MHz. As before, θ is the angle between $\vec{H}_o$ and c. From the ENDOR data, it was impossible to resolve $\tilde{\tilde{P}}_{Na}$ or observe corrections to the hyperfine interaction due to the symmetry of the Na^+ cations within the conduction plane. The near Na resonance certainly results from the sum of several Na^+ cations residing in different environments.

The distant Al ENDOR signal is displayed in Figure 16. This spectrum consists of 5 quadrupole lines centered at the aluminum Zeeman energy, $g_{Al}\mu_B H_o$. The ^{27}Al and ^{23}Na nuclear Zeeman energies are almost identical ($g_{Na}/g_{Al} = 1.015$), but it is possible to attribute this resonance to Al from the number of quadrupole lines present. In the absence of a nearby color center, the distant Al quadrupole interaction displays axial symmetry along the c axis as predicted by the crystal structure, and the data is fit by $P_{||} = 0.39(7)$ MHz. Additional lines in Figure 16 could be caused by distant Na, different distant Al, or Al nuclei with hyperfine interactions comparable to or less than the observed quadrupole splitting.

2. K Beta-Alumina Results

The EPR spectrum of the F^+ center in K beta-alumina is similar to that obtained in Na beta-alumina. Once more, the characteristic 11 line hyperfine splitting was observed, and there were only minor changes in $\tilde{\tilde{g}}$ and $\tilde{\tilde{A}}$ with $g_{||} = 2.0075(5)$, $g_{\perp} = 2.0043(5)$, $A_{||} = 16.4(2)$ gauss, and $A_{\perp} = 15.5(2)$ gauss for K beta-alumina. The most noticable difference in the F^+ EPR data for the two materials was in the width of the hyperfine lines. For $\vec{H}_o || c$ in Na beta-alumina, the linewidth is $\Delta H = 11$ gauss, but in K beta-alumina the linewidth is $\Delta H = 5$ gauss.[30/] This is consistent

Figure 16. Distant Al ENDOR spectrum of Na beta-alumina. H_o = 5346 gauss, f_o = 15.02 GHz, and $\vec{H}_o \| c$. A prominent five line quadrupole structure is indicated.

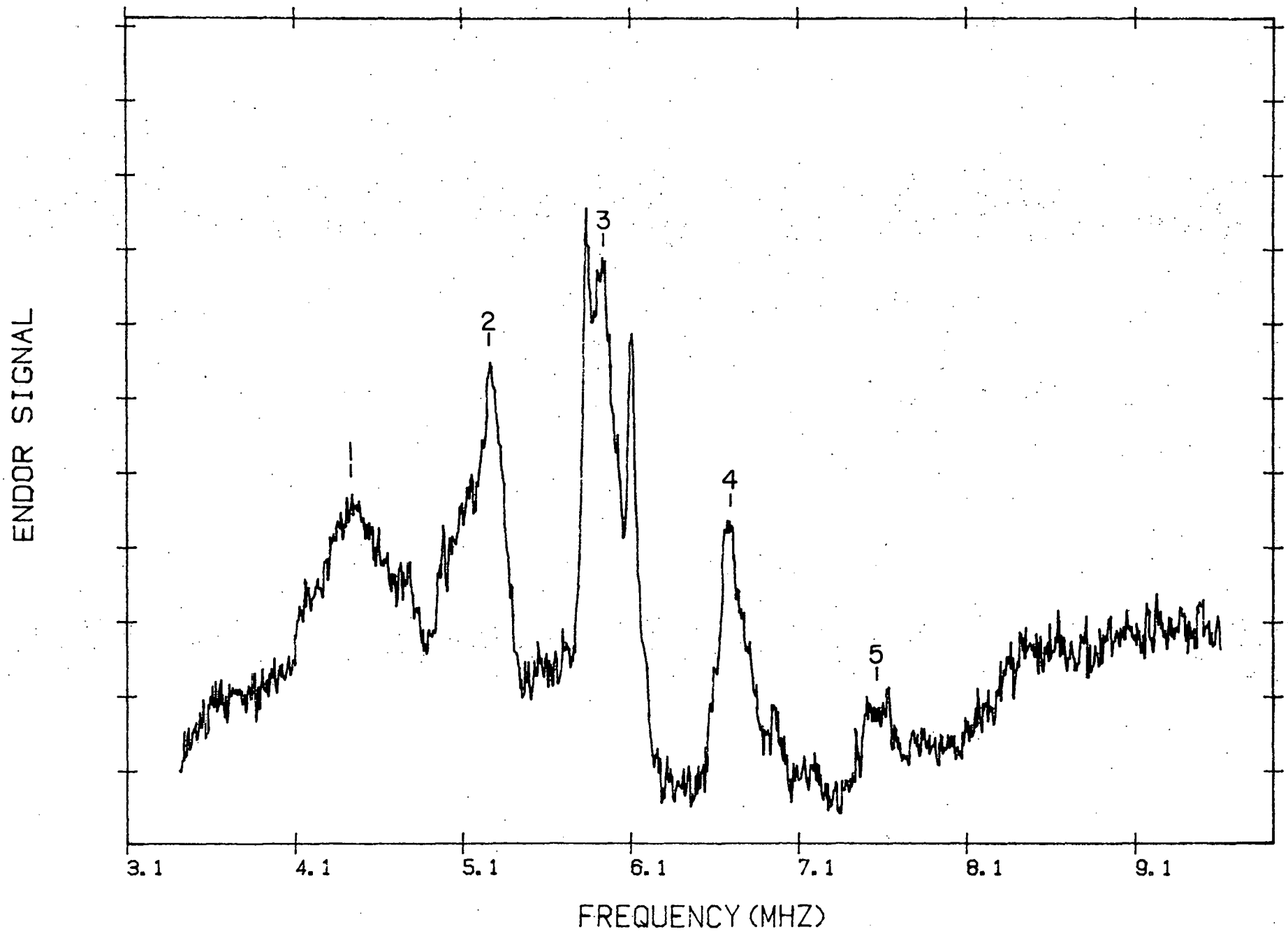
ENDOR SIGNAL
1
2
3
4
5
3.1
4.1
5.1
6.1
7.1
8.1
9.1
FREQUENCY (MHZ)

with the idea that the linewidth is due partially to the unresolved Na or K hyperfine interaction.[29] The nuclear moment of ^{39}K is significantly smaller than that of ^{23}Na in support of the linewidth data.

A near Al ENDOR spectrum is shown in Figure 17. The two large ENDOR lines in this figure are associated with the hyperfine splitting observed in the EPR data. A fit of the hyperfine interaction for these resonances (see Fig. 18) predicts a = 44.3(2) MHz and b = 0.7(1) MHz in agreement with $A_{||}$ and $A_{\perp}$ values. The quadrupole splitting for this ligand could be resolved on only a few spectra with $P_{||}$ = 0.7(3) MHz. The other pair of ENDOR lines, denoted Al', in Figure 17 are identified as an additional near aluminum resonance by the separation of the two lines, $2g_{Al}\mu_B H_o$. The Al' ligand was not observed in the EPR spectra, and it is highly isotropic with a' = 34.7(7) MHz and b' $\lesssim$ 0.7 MHz. Discussion of the Al' resonance is resumed with the Li beta-alumina data where a similar resonance is observed.

The K beta-alumina ENDOR measurements on the F^+ center did not reveal any potassium resonance. The weak potassium hyperfine interaction and small Zeeman energy causes the broad, near ^{39}K lines to overlap and occur at a low enough frequency to make these lines unresolvable. A distant Al resonance similar to the one in Na beta-alumina was observed in K beta-alumina with $P_{||}$ = 0.4(1) MHz.

3. Li Beta-Alumina Results

The irradiation and annealing procedure which produced the F^+ centers in Na and K beta-alumina creates two varieties of F^+ centers in Li beta-alumina. These centers are revealed by the Li beta-alumina EPR

Figure 17. ENDOR spectrum of near Al nuclei in K beta-alumina. H_o = 5318 gauss, f_o = 14.96 GHz, and $\vec{H}_o \perp c$. The Al and Al' resonances are indicated, and the quadrupole structure is labeled on one of the Al peaks.

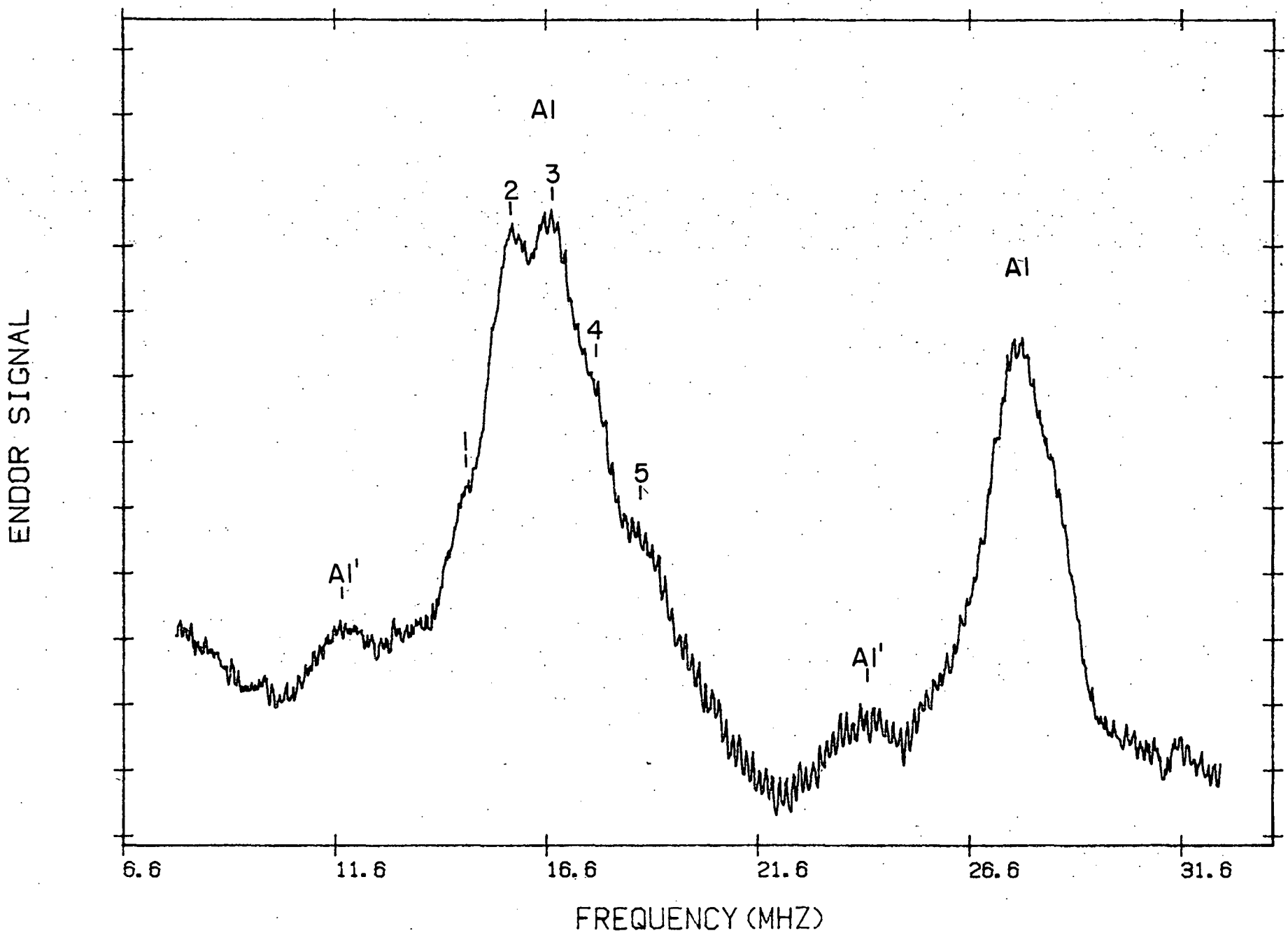
ENDOR SIGNAL
A1
2
3
4
5
1
A1'
A1
A1'
6.6
11.6
16.6
21.6
26.6
31.6
FREQUENCY (MHZ)

Figure 18. ENDOR data for the F^+ - Al hyperfine interaction in K beta-alumina as a function of the direction of the applied magnetic field. The solid line is a fit to an $\tilde{\tilde{A}}$ with the form of Eq. (13) of the text.

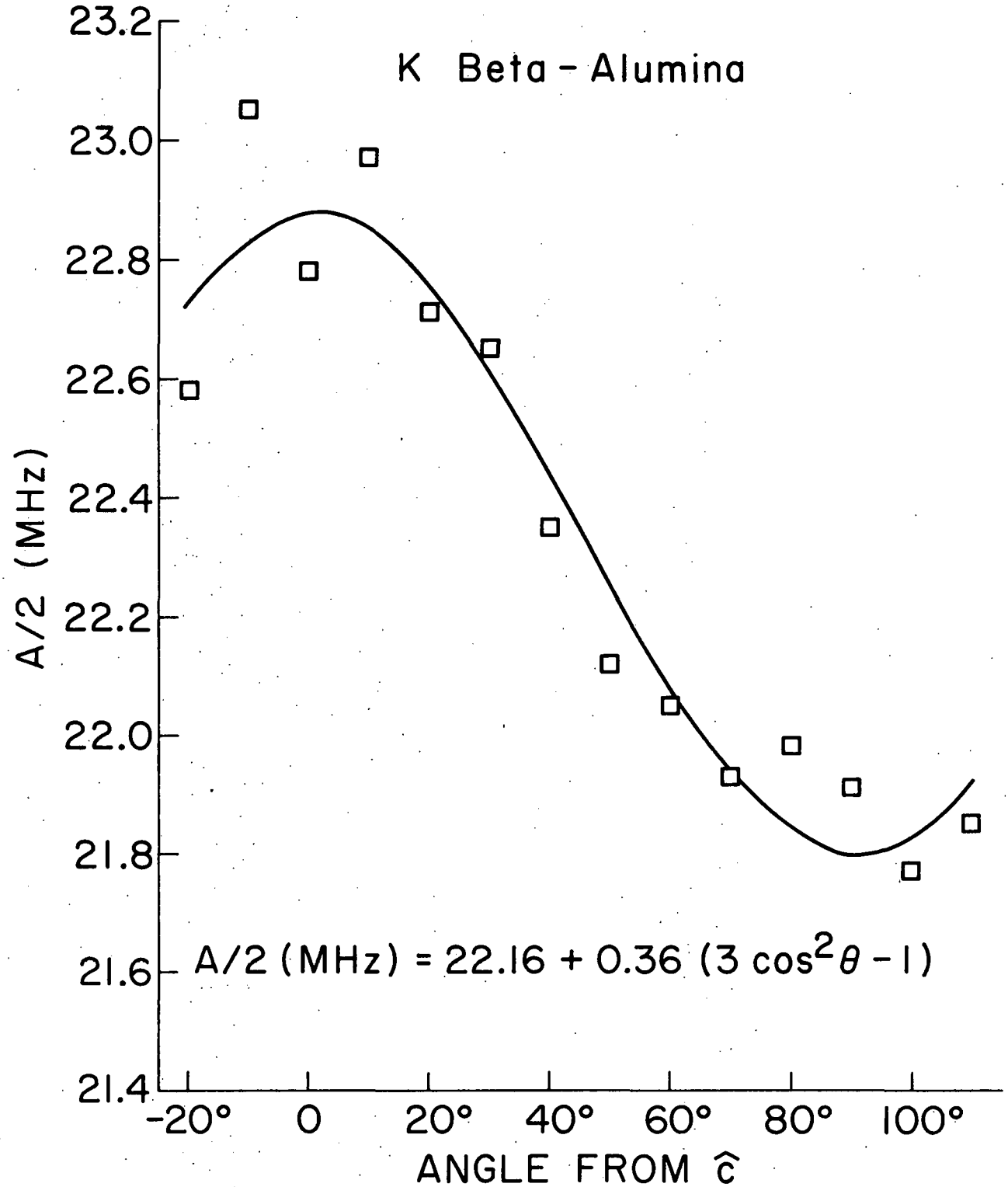
K Beta - Alumina
23.2
23.0
22.8
22.6
22.4
22.2
22.0
21.8
21.6
21.4
A/2 (MHz)
A/2 (MHz) = 22.16 + 0.36 (3 cos²θ - 1)
-20°
0
20°
40°
60°
80°
100°
ANGLE FROM ĉ

spectrum shown in Figure 19. This spectrum consists of a strong 11 line pattern with an intensity ratio indicative of two equivalent Al ligand nuclei. The center associated with the intense 11 line hyperfine splitting is denoted with a superscript prime. The weaker lines in this EPR spectrum are part of another 11 line hyperfine interaction belonging to a center denoted with no superscript.

The EPR spectra of both centers can be resolved by plotting the position of each hyperfine line for different $\vec{H}_o$ orientations as shown in Figure 20. This figure clearly displays the two distinct 11 line patterns indicated by diamonds (primed) and squares (unprimed). The EPR spectrum for each center is described by Eq. (24) with $\tilde{\tilde{A}}$ having axial symmetry along the c axis, and the solid lines in Figure 20 result from a computer fit of the data producing $g'_{||}$=2.0069(5), $g'_{\perp}$ = 2.0059(5), $g_{||}$ = 2.0083(5), $g_{\perp}$ = 2.0049(5), $A'_{||}$ = 13.2(2) gauss, $A'_{\perp}$ = 12.9(2) gauss, $A_{||}$ = 15.2(2) gauss, and $A_{\perp}$ = 14.5(2) gauss.

Analysis of the EPR spectra verifies that each of these color centers interacts with 2 equivalent Al nuclei. The symmetry of $\tilde{\tilde{A}}$ indicates that c is the bond axis for the Al - F^+ - Al bond, and the spin Hamiltonian parameters for this center closely resemble those obtained for the F^+ center in Na and K beta-alumina. The weak anisotropy of the $F^{+'}$ center makes it more difficult to determine the direction of the Al - $F^{+'}$ - Al bond, and the size of this hyperfine interaction is slightly smaller than the Al - F^+ coupling. These factors suggest that the small deviations in $\tilde{\tilde{g}}$ and $\tilde{\tilde{A}}$ for these centers are probably caused by different environments within the conduction plane. Also, the Al - $F^{+'}$ interaction resembles the Al' hyperfine interaction observed in K beta-alumina suggesting that the $F^{+'}$ center is present at low concentrations in that material.

Figure 19. Derivative of the EPR spectrum from F^+ centers in the conduction plane of Li beta-alumina as measured at 77 K and 9.3 GHz, with $\vec{H}_o$ parallel to the c axis. Features of the eleven line pattern displayed in Fig. 12 are still visible.

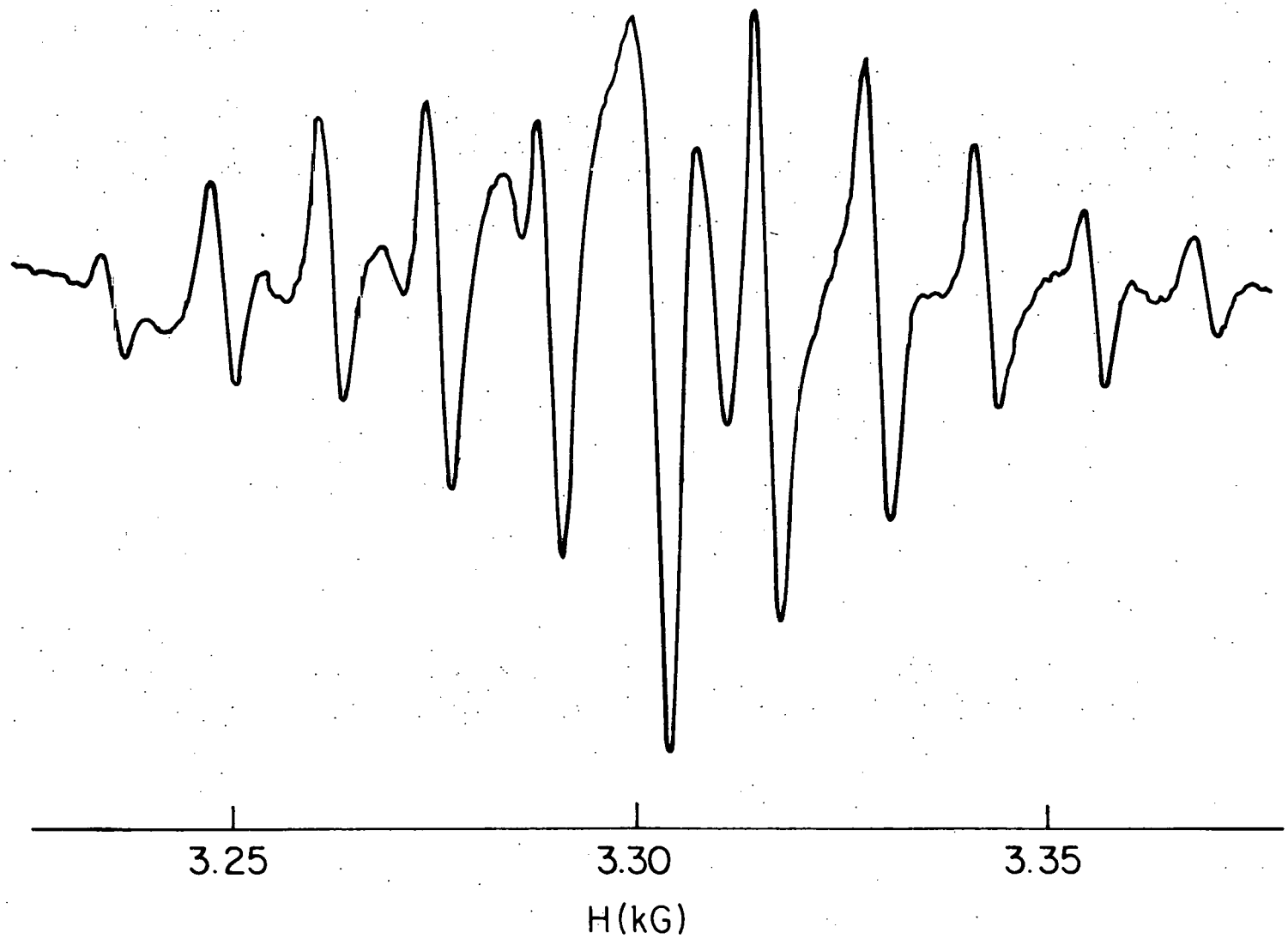
3.25
3.30
3.35
H(kG)

Figure 20. Peak positions in the Li beta-alumina EPR spectrum as a function of the applied magnetic field direction. The diamonds produced the fit of the $F^{+\prime}$ center, and the squares were used in the F^{+} center fit. The crosses represent EPR peaks that were not used in either fit. The solid lines result from fits of both the F^{+} and $F^{+\prime}$ centers to Eq. (24) of the text.

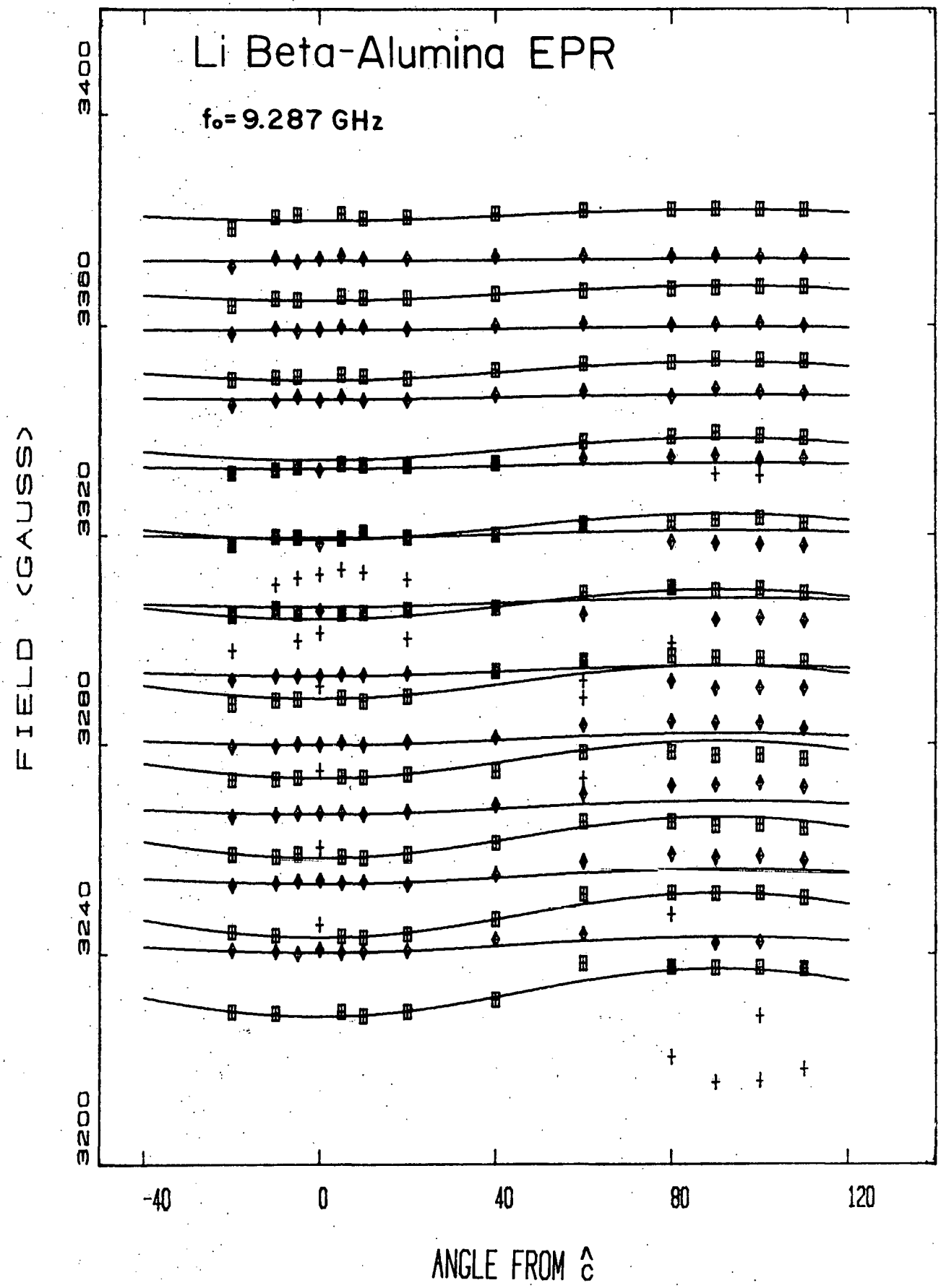
Li Beta-Alumina EPR
fo= 9.287 GHz
FIELD (GAUSS)
3400
3360
3320
3280
3240
3200
-40
0
40
80
120
ANGLE FROM ĉ

The ENDOR data for the near Al in Li beta-alumina verifies that the EPR hyperfine splitting observed for both the F^+ and $F^{+'}$ centers is caused by Al ligands with $a \simeq 42$ MHz and $a' \simeq 36$ MHz. A near Al ENDOR spectrum is shown in Figure 21. Further analysis of this resonance was unsuccessful due to the width of these ENDOR lines.

The low frequency ENDOR lines in Li beta-alumina are displayed in Figure 22. The near and distant Li lines are seen as a broad peak near $g_{Li}\mu_B H_o = 8.9$ MHz. The model for the F^+ center wave function predicts that the Fermi contact hyperfine interaction with the near ^7Li is ~ 2.0 MHz. For this reason, it is not possible to resolve the Li hyperfine interaction from the broad Li ENDOR line. A weak Li hyperfine coupling is confirmed by the Li beta-alumina EPR linewidth which is comparable to that observed in K beta-alumina. The distant Al spectrum at 6 MHz is very complex, but it is still possible to identify 5 major splittings with $P_{||} = 0.43(6)$ MHz. The additional ENDOR lines probably result from the other distant Al nuclei or near Al nuclei with hyperfine couplings comparable to the size of the quadrupole splitting.

4. Discussion of the F^+ Data

Until this point, no arguments have been given for identifying the color center as an F^+ center, but with all of the data presented, it is now possible to outline the identification process. All of the spin Hamiltonian parameters obtained from the EPR and ENDOR experiments are listed in Tables I-III. These tables provide a useful reference during this discussion, and for convenience elements of $\tilde{A}$ have been converted to units of MHz.

Figure 21. ENDOR spectrum (inverted) of near Al nuclei in Li beta-alumina. H_o = 5356 gauss, f_o = 15.03 GHz, and $\vec{H}_o$ is 40° from c. The Al and Al' peaks are labeled in the figure.

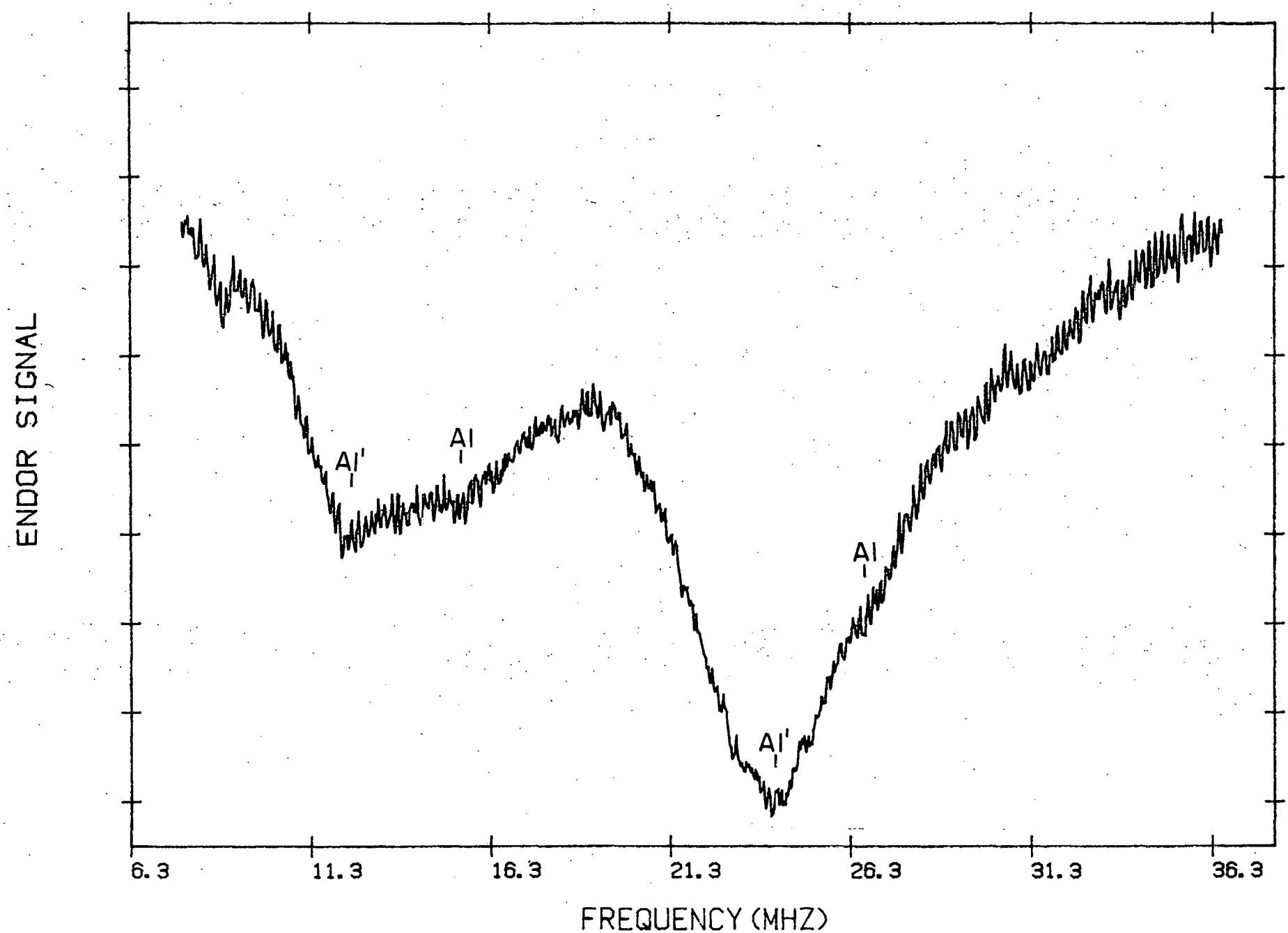
ENDOR SIGNAL
Al'
Al
Al
Al'
6.3
11.3
16.3
21.3
26.3
31.3
36.3
FREQUENCY (MHZ)

Figure 22. Low frequency ENDOR spectrum of Li beta-alumina. H_o = 5346 gauss, f_o = 15.04 GHz, and $\vec{H}_o \| c$. A five line distant Al quadrupole structure is indicated, and a broad Li line is also shown.

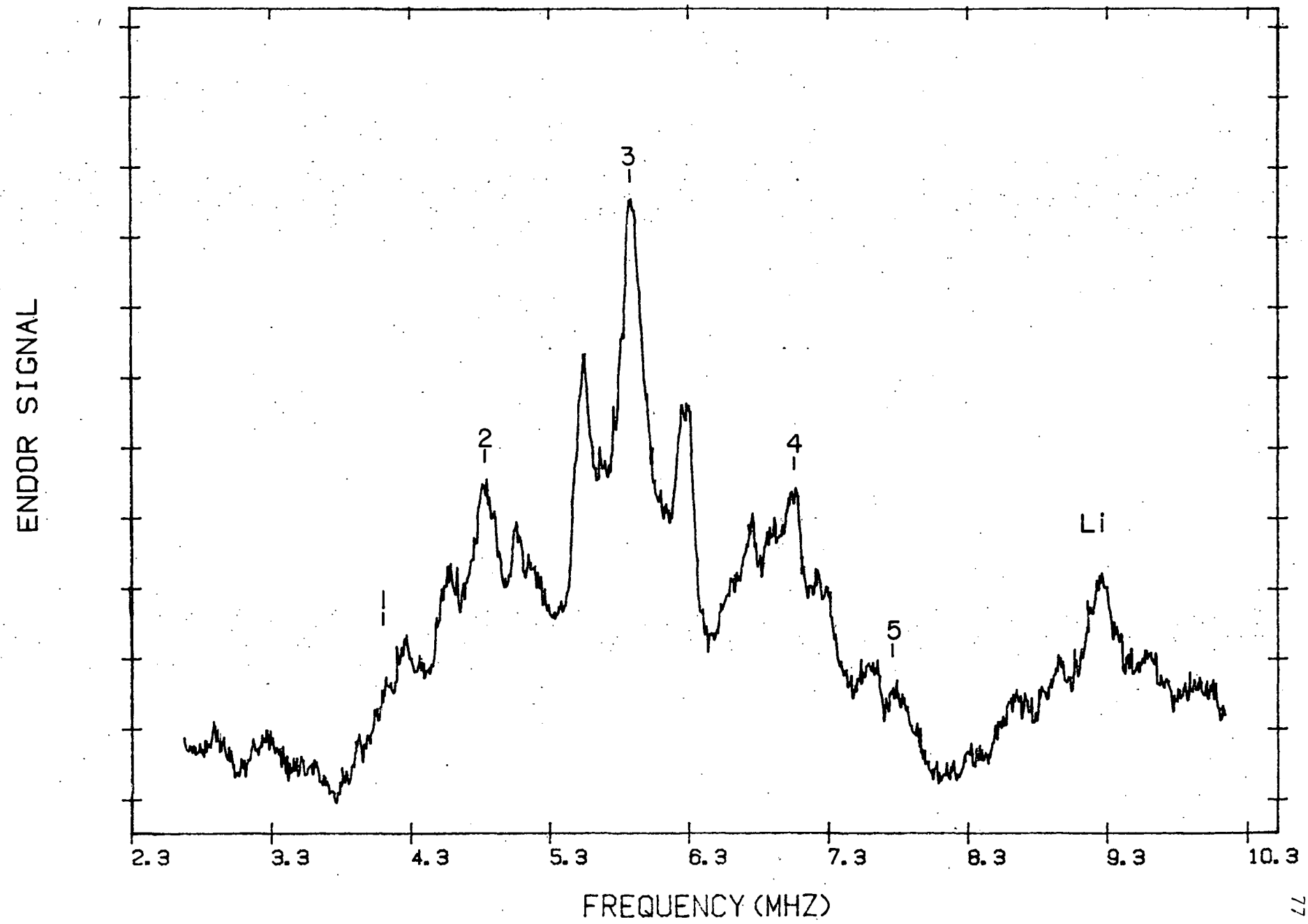
ENDOR SIGNAL
1
2
3
4
5
Li
2.3
3.3
4.3
5.3
6.3
7.3
8.3
9.3
10.3
FREQUENCY (MHZ)

TABLE I

F^+ SPIN HAMILTONIAN PARAMETERS FOR Na BETA-ALUMINA OBTAINED FROM EPR AND ENDOR MEASUREMENTS. THE RESULTS OF OTHER INDEPENDENT STUDIES ARE INCLUDED FOR COMPARISON

Parameter	Units	Exp. Value	Source	Ligand
$g_{\|\|}$	---	2.0079(5) 2.0076(2) 2.0085	EPR a b	---
$g_{\perp}$	---	2.0039(5) 2.0036(2) 2.0049	EPR a b	---
$A_{\|\|}$	MHz	47.2(6) 46.78(6) 47.0	EPR a b	Al
$A_{\perp}$	MHz	45.7(6) 45.35(8) 45.2	EPR a b	Al
a	MHz	45.7(1) 45.20(7)	ENDOR c	Al
b	MHZ	1.0(1) 1.20(2)	ENDOR c	Al
$P_{\|\|}$	MHz	0.35(6) 0.383(7)	ENDOR d	Al
a	MHz	9.5(3) 7.8(2)	ENDOR c	Na
b	MHz	1.5(3) 1.2(2)	ENDOR c	Na
$P_{\|\|}$	MHz	0.7(1)	c	Na
$P_{\|\|}$	MHz	0.39(7)	ENDOR	Distant Al

a. Ref. 29.

b. Ref. 30.

c. Ref. 43.

d. Ref. 42.

TABLE II

F^+ SPIN HAMILTONIAN PARAMETERS FOR K BETA-ALUMINA OBTAINED FROM EPR AND ENDOR MEASUREMENTS. THE RESULTS OF ANOTHER INDEPENDENT STUDY ARE INCLUDED FOR COMPARISON

Parameter	Units	Exp. Value	Source	Ligand
$g_{\|\|}$	---	2.0075(5) 2.0076	EPR b	---
$g_{\perp}$	---	2.0043(5) 2.0049	EPR b	---
$A_{\|\|}$	MHz	46.0(6) 46.4	EPR b	Al
$A_{\perp}$	MHz	43.5(6) 44.3	EPR b	Al
a	MHz	44.3(2)	ENDOR	Al
b	MHz	0.7(1)	ENDOR	Al
$P_{\|\|}$	MHz	0.7(3)	ENDOR	Al
a'	MHz	34.7(7)	ENDOR	Al'
b'	MHz	$\lesssim$ 0.7	ENDOR	Al'
$P_{\|\|}$	MHz	0.4(1)	ENDOR	Distant Al

b. Ref. 30.

TABLE III

F^+ SPIN HAMILTONIAN PARAMETERS FOR Li BETA-ALUMINA OBTAINED FROM EPR AND ENDOR MEASUREMENTS

Parameter	Units	Exp. Value	Source	Ligand
$g_{\|\|}'$	---	2.0069(5)	EPR	---
$g_{\perp}'$	---	2.0059(5)	EPR	---
$g_{\|\|}$	---	2.0083(5)	EPR	---
$g_{\perp}$	---	2.0049(5)	EPR	---
$A_{\|\|}'$	MHz	37.0(6)	EPR	Al'
$A_{\perp}'$	MHz	36.3(6)	EPR	Al'
$A_{\|\|}$	MHz	42.6(6)	EPR	Al
$A_{\perp}$	MHz	40.6(6)	EPR	Al
a'	MHz	~36	ENDOR	Al'
a	MHz	~42	ENDOR	Al
$P_{\|\|}$	MHz	0.43(6)	ENDOR	Distant Al

The dominant characteristic of all of the EPR data is the 11 line hyperfine splitting. This pattern is a clear indication of 2 equivalent Al ligand nuclei, and the ENDOR data repeatedly confirms that the EPR hyperfine structure is caused by Al. The only place in the structure of beta-alumina where a color center interacts with 2 equivalent Al nuclei is in the conduction plane, the mirror plane. The closest Al nuclei to the conduction plane are found in the Al - O - Al bonds across the plane at the "bridge" and charge compensation oxygen sites. A color center located at an oxygen site of this type should display an Al hyperfine interaction with axial symmetry along the c axis in agreement with the data. Therefore, based on the Al hyperfine interaction, it is believed that the color centers are located at conduction plane oxygen sites.

In order to identify the type of color centers present in the conduction plane it is necessary to look closely at the magnitude of various spin Hamiltonian parameters. The fact that the g factors are so close to the free electron value suggest that the wave function of the color center is an s or p-state. For a p-state color center, the g tensor displays axial symmetry along the axis of the p-lobe containing the unpaired spin, and there is significant g factor anisotropy with $g_{||} \approx g_e$ and $g_{\perp} - g_e = 0.1 - 0.01$.[38,39] The EPR data shows significant deviation from g_e when $\vec{H}_o$ is parallel to the c axis. That would place the p-lobe in the conduction plane and produce a small contact interaction with the Al nuclei above and below the conduction plane. This contradicts the data which exhibits a large aluminum contact interaction. Also, the g factor shift from g_e is much smaller than the shift normally observed for a p-state color center. For these reasons p-state centers such as the O center

are rejected as a plausible explanation for this color center in beta-alumina.[29]

The observed g factor shifts and Al contact hyperfine interactions suggest instead that the color center is an s-state defect. The model for such a defect is an electron trapped at a conduction plane O^{2-} vacancy (see Fig. 23). This color center is commonly called an F^+ center because a local positive charge remains due to the absence of the divalent oxygen ion. To a first approximation, the F^+ center, like the F center, has a hydrogenic s-state wave function. The F center g shift is produced by the electron spin-orbit interaction with neighboring nuclei, and this model predicts $g - g_e \leq 0$ in agreement with the data for F centers in alkalide halides.[44] However, in oxides and other divalent materials $g - g_e > 0$ has frequently been observed for F^+ centers with g shifts similar to those observed in beta-alumina.[45] This effect has been attributed to the admixture of a charge transfer state where a hole is trapped at a neighboring anion.[46] Using this model it is possible to suggest that a neighboring oxygen within the conduction plane interacts with the F^+ center producing the size and asymmetry of the g shifts, but this calculation has not been attempted.

The magnitude of the observed hyperfine interactions is in agreement with those expected for an F^+ center. The O - Al distance at the bridge oxygen is 1.68 Å with $(a\mu_N)/(g_{Al}\mu_B)$ = 31 MHz from Al ENDOR data on Na beta-alumina. By comparison, the F^+ center in MgO displays a contact interaction with ^{25}Mg such that $(a\mu_N)/(g_{Mg}\mu_B)$ = 32 MHz where the Mg - O distance is 2.1 Å.[47] The magnitude of the near Al dipolar interaction is

Figure 23. The structure of stoichiometric Na beta-alumina with the probable position of an F^+ center indicated within the conduction plane at a bridge oxygen site. Above and below the F^+ center are the two equivalent Al nuclei which produce the observed hyperfine lines in the EPR spectrum. A Na^+ cation is located 3.2 Å from the F^+ center.

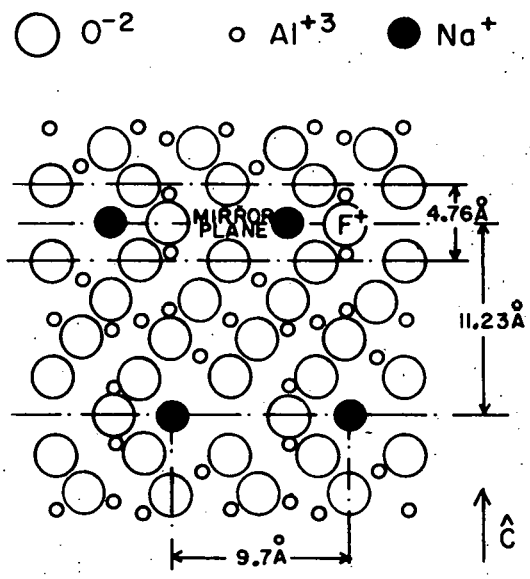
O^{-2}
Al^{+3}
Na^{+}
MIRROR PLANE
F^{+}
4.76Å
11.23Å
9.7Å
ĉ

$$b_{Al} \sim \frac{1}{2} \frac{g_{Al} g \mu_B^2}{R_o^3} = 2.18 \text{ MHz} \qquad (26)$$

where $R_o = 1.68$ Å. This classical dipolar result is about twice as large as the observed Al anisotropy in Na beta-alumina. The same corrections to the electronic wave function that explain the g factor shifts also produce deviations in the dipolar coupling.[29,48]

For an F^+ center at the bridge oxygen site in Na beta-alumina, 3 Beevers-Ross Na^+ ions are each located 3.2 Å away with bond axes 60° apart within the conduction plane. The observed symmetry of the Na hyperfine interaction indicates that the Na-color center bonds are within the conduction plane in agreement with this model. $|\psi(o)|^2$ at the cation nucleus scales roughly as $Z^{1.5}/R_o^3$ for an F center where Z is the atomic number of the ligand.[49,50] Based on the near Al contact interaction, this scaling predicts $a_{Na} = 5.2$ MHz which is within a factor of 2 of the Na ENDOR results. Using the $Z^{1.5}$ scaling, it is possible to take the experimental Na contact interaction, $a_{Na} = 9.5$ MHz, and estimate the Li and K hyperfine couplings to be $a_{Li} = 2.0$ MHz and $a_K = 3.8$ MHz. These small contact terms make resolution of the K and Li hyperfine interactions impossible from the ENDOR data. The discrepancy in the measured values of a_{Na} obtained in this study and the one performed by Barklie et al.[43] probably results from asymmetry in the shape of the broad near Na ENDOR line. The ENDOR resonances observed in this experiment were fairly symmetrical due to the use of both RF sweep directions, but there is no evidence that Barklie also took this precaution.

The measured quadrupole couplings also are consistent with other data. The quadrupole interaction for the near Al resonance has the

expected symmetry axis for an adjacent F^+ center located along the c axis, and preliminary calculations indicate that the quadrupole splitting, $P_{||}$ = 0.4 MHz, is mostly due to the field gradient produced by the effective positive point charge of the F^+ center.[42] The resolved distant Al quadrupole splitting, $P_{||}$ = 0.4 MHz, is the same as the largest Al quadrupole coupling observed in NMR measurements.[51]

Based on this discussion, it is possible to conclude that the 11 line EPR spectrum is caused by an F^+ center located at a conduction plane oxygen site. The observed g factors and hyperfine interactions are all in agreement with this model, and as a result of the EPR and ENDOR experiments, enough is known about the conduction plane color centers to perform relaxation studies in beta-alumina. However, the poor resolution of the ENDOR data makes it impossible to learn anything about the conduction plane itself without a detailed theoretical description of the spin Hamiltonian parameters. At this time, it is not known whether the F^+ resides at a bridge or a charge compensation site, and the $F^{+'}$ center cannot be distinguished from the F^+ center except for the fact that the spin Hamiltonian parameters for the two centers are slightly different. Because all of the previous arguments are equally valid for the $F^{+'}$ center, this defect must also be an F^+ residing at a conduction plane oxygen site, but further comparison of the F^+ and $F^{+'}$ centers is fruitless in the absence of a deeper understanding of the spin Hamiltonian.

F. EPR and ENDOR of Other Color Centers in Beta-Alumina

Using the irradiation procedure outlined in Part A, the only other color center observed is the Abraham-Stapleton (AS) center. EPR data

reveals that this center has a g tensor with axial symmetry about the c axis such that $g_{||} = 2.048(5)$ and $g_{\perp} = 2.002(9)$ for Na beta-alumina.[31] These g values are characteristic of a p-state ion with a trapped hole similar to the g factors observed for O^- centers in oxides.[38] Assuming the AS center is an O^-, the symmetry of the g tensor indicates that the unpaired spin resides in a p-lobe pointing perpendicular to the c axis. With $\vec{H}_o \perp$ c, a hyperfine structure consisting of several closely spaced lines is barely resolvable with a hyperfine splitting of $\sim$7.5 gauss.[31] This structure cannot be resolved for $\vec{H}_o ||$ c.

Preliminary ENDOR data indicates that the hyperfine splitting is associated with a near Al ligand nucleus with $A_{||} = 18$ MHz and $A_{\perp} = 24$ MHz for Na beta-alumina. The quadrupole splitting for this Al ligand appears to be axially symmetric about c with $P_{||} \approx 0.9$ MHz. The quadrupole structure, displayed in Figure 17 and assigned to an Al nucleus adjacent to an F^+ center, could be caused by the presence of an Al nucleus associated with the AS center in the ENDOR spectrum. This would explain the large value of $P_{||}$ in Table II.

Considering the symmetry of $\tilde{\tilde{g}}$ and $\tilde{\tilde{A}}$ for the AS center, there is nothing conclusive to indicate that this center is located in the conduction plane. Also, there is no evidence of conduction plane cation resonances in the AS ENDOR data at this time. Further study of the AS center may be interesting in itself, but preliminary experiments indicate that research on the AS center probably will not reveal any new information about the conduction plane.

IV. ELECTRON SPIN RELAXATION STUDIES OF THE F^+ CENTER

A. Experimental Procedure

The electron spin relaxation rates were measured at 9.5 and 16.5 GHz using the pulse saturation and recovery technique. During this procedure, the magnetic field was tuned to a point in the EPR absorption spectrum and held constant. A high power saturating microwave pulse was sent to the sample cavity burning a hole in the EPR line, and after the pulse was turned off, the microwave absorption of the sample was monitored using a low microwave power level so that the spin system was not significantly perturbed. After saturation, the hole in the EPR line recovered with a characteristic time constant which defines the electron spin relaxation rate.

A block diagram of the Ku-band pulsed spectrometer is shown in Figure 24. (The X-band spectrometer was similar to the one presented. For details, see Ref. 52.) Like the ENDOR spectrometer, a superheterodyne detector was used to monitor the EPR signal during recovery. During this phase, switch A was closed, attenuating the microwave radiation entering the sample cavity, and switch B was open to permit the signal reflected from the cavity to be detected. A pulse was turned on by closing switch B to protect the IF amplifier from saturation and opening switch A. This pulse-recovery cycle was repeated, and the recoveries were accumulated using a signal averager with a calibrated time base. After signal averaging, a crude measurement of the relaxation rate was obtained using a

Figure 24. Schematic diagram of superheterodyne pulsed EPR spectrometer at Ku-band (16.5 GHz).

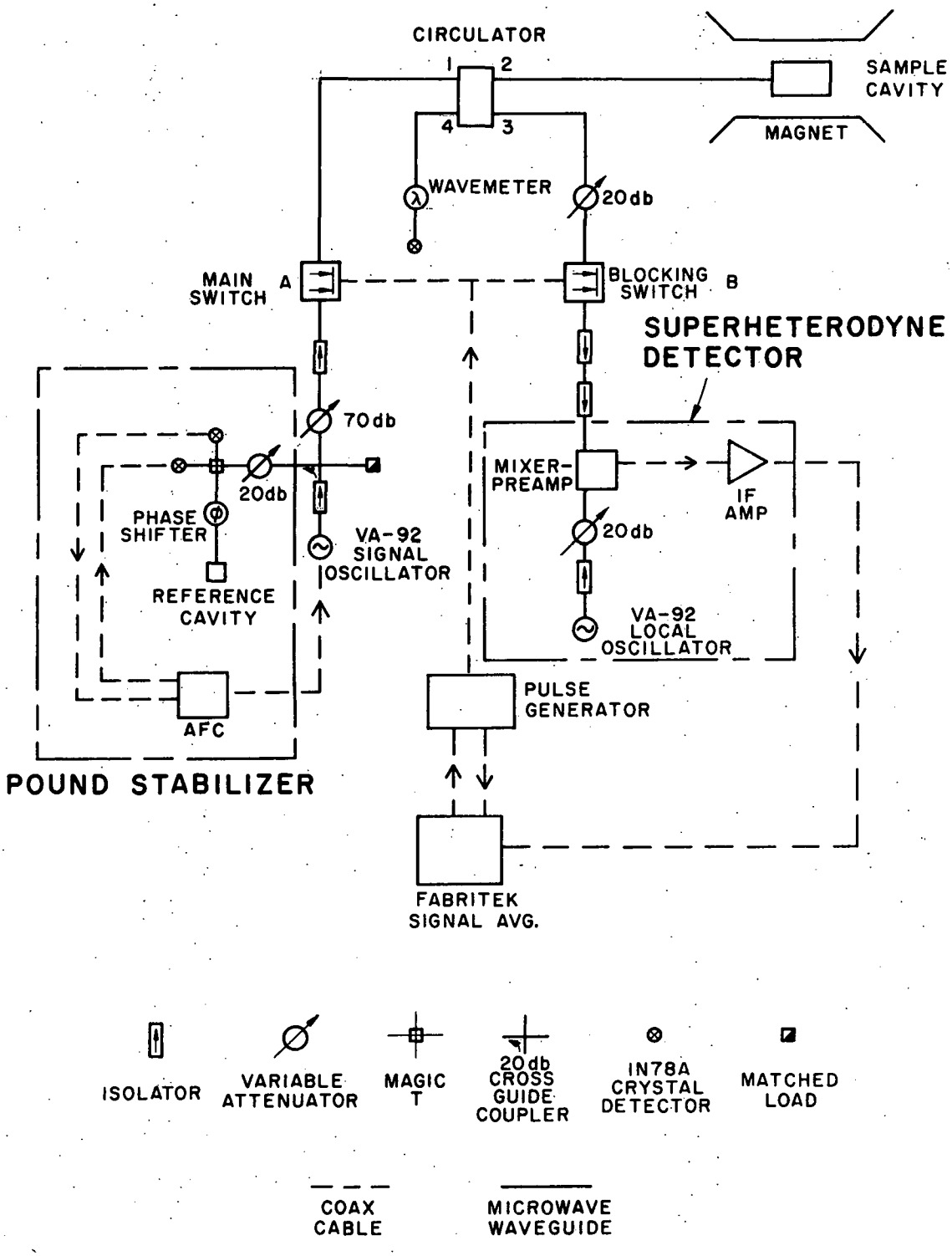
CIRCULATOR
1
2
3
4
SAMPLE CAVITY
MAGNET
WAVEMETER
20db
MAIN SWITCH
A
BLOCKING SWITCH
B
SUPERHETERODYNE DETECTOR
70db
20db
PHASE SHIFTER
REFERENCE CAVITY
VA-92 SIGNAL OSCILLATOR
MIXER-PREAMP
IF AMP
20db
VA-92 LOCAL OSCILLATOR
AFC
POUND STABILIZER
PULSE GENERATOR
FABRITEK SIGNAL AVG.
ISOLATOR
VARIABLE ATTENUATOR
MAGIC T
20db CROSS GUIDE COUPLER
IN78A CRYSTAL DETECTOR
MATCHED LOAD
COAX CABLE
MICROWAVE WAVEGUIDE

logarithmic amplifier, and the recovery was recorded on paper tape or a floppy disc for more detailed analysis later. Because of the rapid changes in the sample cavity power level, the signal klystron was locked to a reference cavity that was tuned to resonate at the same frequency as the sample cavity. The power level at the reference cavity was constant during the pulse-recovery cycle.

The sample temperature was measured and controlled to within a few millikelvin with a Ge temperature sensor mounted inside the cavity wall. The sensor formed one arm of a low frequency bridge circuit whose error voltage was phase sensitively detected and used to drive a heater wire wound around the body of the cavity. The cavity assembly was thermally isolated from the liquid helium bath by a copper can containing low pressure helium exchange gas and thinwall stainless steel waveguide. A TE_{112} cavity was used, and the beta-alumina sample was placed directly on the cavity sidewall with a thin coat of N-grease to insure a good thermal contact.

The beta-alumina samples were irradiated and bleached using the method previously described, and all the recovery times quoted were measured at the same point in the F^+ hyperfine spectrum, with the magnetic field parallel to the c axis, but away from the central peak in order to avoid any additional resonances associated with g values of 2.00. However, the observed relaxation rates appeared to be independent of the point in the hyperfine spectrum where the experiment was performed, including the complicated Li beta-alumina EPR spectrum. Due to the difference in g factors with $\vec{H}_o \| c$, the AS center did not overlap the F^+ EPR spectrum at 16.5 GHz, and the presence of the AS center was not a factor in the spin relaxation measurements on K beta-alumina.

The observed relaxation rate of the F^+ center represents an average value as will become evident later, and for this reason, the recoveries were seldom truly exponential in time. The data should be construed as representative of the recovery rate between times at which the signal is 60% and 90% recovered to its thermal equilibrium value, but the relaxation rate only varied ∿10% for different intervals that were selected between 10% and 90% of the total recovery. The initial 10% of the recovery was often quite rapid due to spectral diffusion and drift problems. The reported relaxation rates were independent of pulse duration over the range 0.3 - 0.003 sec, and the data were not dependent on the amplitude of the saturating pulse. By consistently fitting the recovery over the 60-90% interval and varying these other parameters, the observed relaxation rates were reproducible to within ≈10% of the reported value at each temperature.

B. A Survey of Color Center Relaxation Phenomena

In an ordered ionic crystal, a color center spin relaxes via scattering processes involving only phonons because of the absence of other effective low energy excitations. Unlike d and f-state ions, color centers have no low energy excited electronic states thus reducing the number of plausible relaxation mechanisms, and the spin-orbit interaction is small enough to be ineffective in coupling the spin to the phonon bath. Instead, the phonons interact with the color centers via modulation of the electron-nuclear hyperfine interaction, $A\,\vec{I}\cdot\vec{S}$.

Expanding the hyperfine interaction in strain components, one obtains a spin-lattice Hamiltonian

$$H_{S\text{-}PH} = \vec{I}\cdot\vec{S}\left[\bar{A}^{(1)}\sum_{m} e_m + \bar{A}^{(2)}\sum_{n,m} e_n e_m + \ldots\right] , \quad (27)$$

where $\bar{A}^{(1)}$ is an average value of $\partial A/\partial e_m$ and $\bar{A}^{(2)}$ is an average value of $\partial^2 A/\partial e_n \partial e_m$. Using the golden rule, the first term in Eq. (27) produces a one-phonon direct process with a spin-lattice relaxation rate

$$\frac{1}{T_D} = B_1 (\hbar\omega)^3 \coth\left(\frac{\hbar\omega}{2kT}\right) , \quad (28)$$

where B_1 is a constant, and the resonant phonon energy is $\hbar\omega = g\mu_B H_o$. For $kT >> \hbar\omega$, this reduces to

$$\frac{1}{T_D} = B_1' H_o^2 T , \quad (29)$$

where B_1' is also a constant. The H_o^2 in Eq. (29) occurs because the magnetic electron-nuclear hyperfine interaction is time-odd, and $\langle + |\bar{A}^{(1)}\vec{I}\cdot\vec{S}| - \rangle \neq 0$ for Kramer's conjugate states $|+\rangle$ and $|-\rangle$.[53] In a similar manner, the second term in Eq. (27) predicts that the relaxation rate for the two-phonon Raman process is[54]

$$\frac{1}{T_R} = B_2 T^7 J_6\left(\frac{\theta_D}{T}\right) , \quad (30)$$

where θ_D is the Debye temperature, B_2 is a constant, and

$$J_6(z) = \int_0^z \frac{x^6 e^x}{(e^x-1)^2}\, dx . \quad (31)$$

For $\theta_D/T >> 1$, $J_6(\theta_D/T)$ becomes a constant, and at low temperatures the Raman relaxation process is

$$\frac{1}{T_R} = B_2' T^7 \quad (32)$$

with B_2' a constant. Summing the direct and Raman processes, the low temperature spin-lattice relaxation rate of an F center in an ordered material has the form

$$\frac{1}{T_1} = B_1' H_o^2 T + B_2' T^7 \quad . \tag{33}$$

At higher temperatures where $\theta_D/T \lesssim 1$, the Raman process becomes $1/T_R \propto T^2$, which is the classical result for a two-phonon process at high temperature.

The relative magnitudes of these competing relaxation processes are such that for $T \lesssim 5$ K the direct process dominates, and $1/T_1 \propto T$. At slightly higher temperatures, 5 K $\lesssim T \lesssim$ 50 K, the Raman process takes over, and $1/T_1 \propto T^7$ is observed. The temperature dependence described by Eq. (33) has been confirmed experimentally for F centers in an ordered material,[55] and due to the weak coupling of the F center-ligand hyperfine interaction, spin-lattice relaxation rates as low as $\sim 10^{-3}$ sec^{-1} at 2 K and 3000 gauss have been observed depending on the sample preparation technique.[48,55,56,57]

The introduction of isolated defects and impurities in a crystal often produces additional low energy excitations resulting from atomic tunneling. Common examples of this behavior are the translational tunneling of Li^+ impurities in alkalide halides and rotational tunneling of OH^- and CN^- impurities in ionic crystals.[58] These tunneling states are observed in heat capacity, thermal conductivity, and dielectric measurements,[58] and different electron spin relaxation mechanisms are available due to the presence of the additional excitations.

Anomalous electron spin relaxation rates have been observed for F centers adjacent to Li^+ ions (F_A(Li) center) in KCl and KBr.[59,60] These studies indicate that the color center relaxation rate is several

orders of magnitude larger ($1/T_1 \sim 10^2$ sec^{-1} at 2 K and 3000 gauss) due to the presence of the tunneling impurities, and the temperature dependence of the electron spin relaxation rate is also markedly different. Unfortunately, there is a wide variation in the temperature dependence of $1/T_1$ for even closely related systems like KCl:Li^+ and KBr:Li^+.[61] The change in the spin relaxation rate with temperature is highly dependent on the size and distribution of the isolated defect tunneling state energies, and as a result, minor changes in the crystal environment of the Li^+ defects produce observable effects on the electron spin relaxation data. The concentration of the tunneling impurities also may alter the tunneling state energies due to strain or electric-dipole interactions between defects.[62,63]

In a glass, the problem of predicting the behavior of the spin relaxation rate vs temperature is not as formidable insofar as the distribution of the tunneling state energies is not highly dependent on the particular material being studied. In 1966, Feldman et al.[64] measured the spin relaxation of atomic hydrogen in fused silica and observed that between 2 and 20 K, $1/T_1$ varied strongly with temperature, and above 20 K, $1/T_1$ became nearly linear with T. Murphy[65] attributed this behavior to the presence of "local vibrations" within the glass. Later this same temperature dependence was observed for the spin relaxation of a paramagnetic radical in acetyl-(d,l)-alanine, an organic crystal in which rotational tunneling is believed to occur.[66] Once more, Murphy's model was used to describe the data, and the problem of electron spin relaxation in a glass was largely overlooked for the last decade in spite of the success of the LTS model in explaining other low temperature properties of glasses.

C. Electron Spin Relaxation by Localized Tunneling States

The electron spin relaxation data for the F^+ center in beta-alumina displayed the same temperature dependence as that observed by Feldman for vitreous silica. The results for Na beta-alumina are shown in Figure 25. If one attempts to explain this data by attributing the relaxation rate above 10 K to a direct process, varying as T and the low temperature data to a temperature independent cross relaxation mechanism, then the linear portion of the curve would have to extrapolate through the origin, which it clearly does not. In addition, the magnitude of the relaxation rate is several orders of magnitude faster than usually observed for F centers in ordered crystalline materials. These same characteristics are observed in the F^+ center relaxation data for Na, Li, and K beta-alumina in Figure 26. These results are not explained by conventional phonon processes, and the additional relaxation mechanisms associated with the presence of the LTS system must be included.

In order to develop a model for electron spin relaxation in a glass, it is first necessary to introduce phenomenological interaction Hamiltonians coupling the color center spins, LTS, and phonons. For a tunneling state consisting of an atom residing in an asymmetric double well potential, the unperturbed LTS Hamiltonian in the nondiagonal basis of two separate wells is denoted with a superscript prime and given by[16]

$$H_o' = \frac{1}{2}\begin{pmatrix} \xi & \Delta \\ \Delta & -\xi \end{pmatrix} \tag{34}$$

where ξ is the asymmetry of the potential wells, and Δ is an overlap energy given by $\hbar\omega_o \cdot \exp(-\lambda)$. Here $\hbar\omega_o$ is the ground state energy of an

Figure 25. Spin relaxation rate of the F^+ center in Na beta-alumina as measured at microwave frequencies of 9.5 and 16.5 GHz. The curves (dashed and solid lines) are the result of the model described in the text.

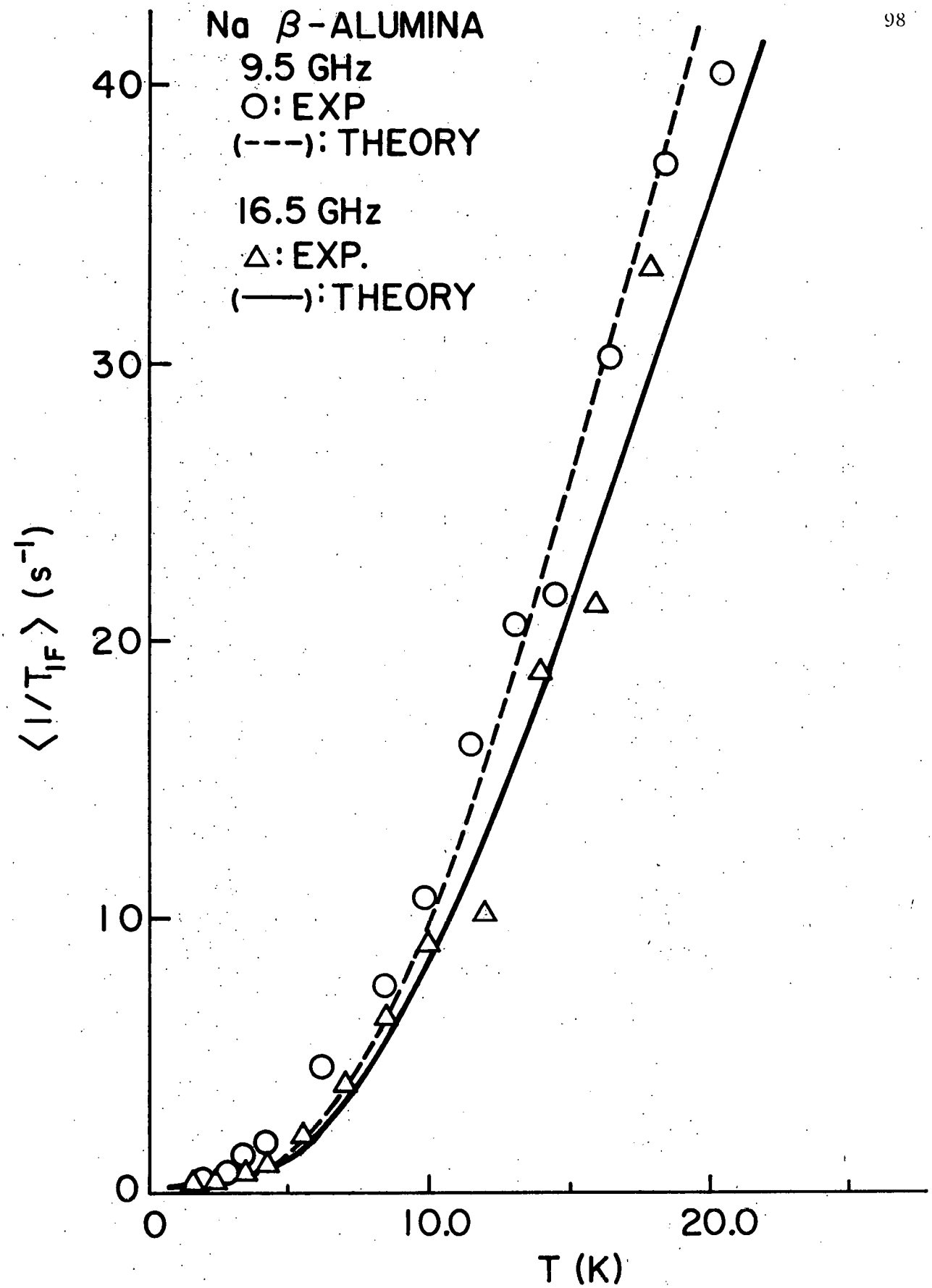
Na β-ALUMINA
9.5 GHz
○: EXP
(---): THEORY
16.5 GHz
△: EXP.
(——): THEORY
40
30
20
10
0
0
10.0
20.0
T (K)
⟨1/T1F⟩ (s⁻¹)

Figure 26. Spin relaxation rate of the F^+ center in Na, Li, and K beta-alumina as measured at a single microwave frequency of 16.5 GHz. The curve through the data for each sample results from the model described in the text.

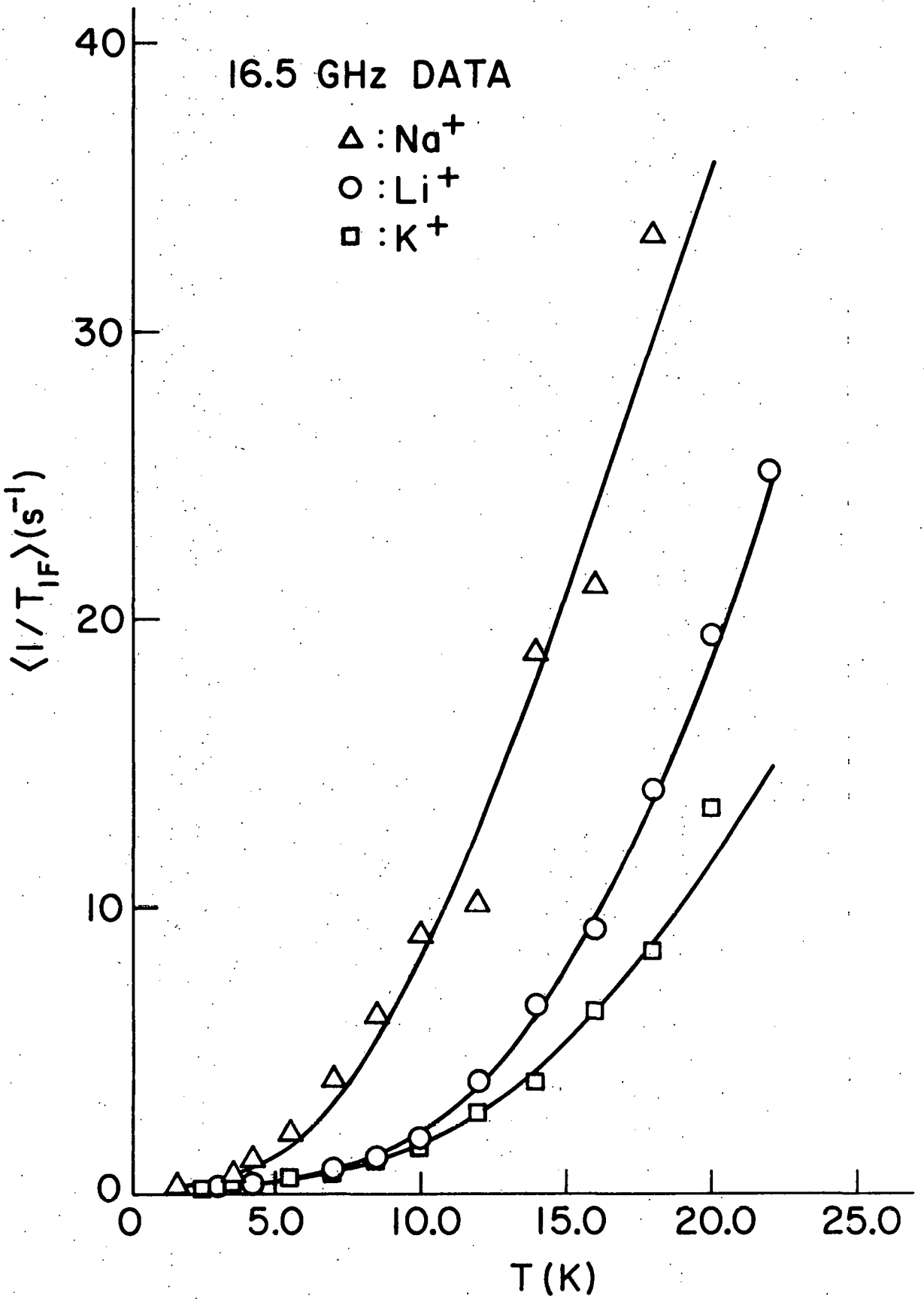
16.5 GHz DATA
△ : Na+
○ : Li+
□ : K+
40
30
20
10
0
0
5.0
10.0
15.0
20.0
25.0
T (K)
⟨1/T1F⟩(s-1)

isolated potential well, and $\lambda = (2 \cdot m \cdot V)^{\frac{1}{2}} d/\hbar$, where V is the barrier height, d the well separation, and m is the mass of the tunneling unit. In the diagonal (unprimed) basis, the Hamiltonian becomes

$$H_o = \frac{1}{2} \begin{pmatrix} E & o \\ o & -E \end{pmatrix} , \qquad (35)$$

where E is the energy splitting between the two levels and equals $(\xi^2 + \Delta^2)^{\frac{1}{2}}$. A fundamental property of the LTS theory is that there exists an almost constant and broad distribution of E values up to a cutoff, E_{max}/k, of the order of 10-100 K. It is generally assumed that the LTS distribution can be described by a density of states given by[15]

$$P(E,\Delta) = \frac{P(E)}{\Delta(1-(\Delta/E)^2)^{\frac{1}{2}}} \qquad (36)$$

where P(E) is weakly dependent on E.

The tunneling state-phonon interaction is obtained by expanding the nondiagonal LTS Hamiltonian, H_o', in strain. Transforming into the diagonal basis, this interaction becomes[16]

$$H_{T\text{-}PH} = \frac{1}{2E} \begin{pmatrix} \xi\frac{\partial \xi}{\partial e} + \Delta\frac{\partial \Delta}{\partial e} & \xi\frac{\partial \Delta}{\partial 3} - \Delta\frac{\partial \xi}{\partial e} \\ \xi\frac{\partial \Delta}{\partial e} - \Delta\frac{\partial \xi}{\partial e} & -\xi\frac{\partial \xi}{\partial e} - \Delta\frac{\partial \Lambda}{\partial e} \end{pmatrix} \cdot e \qquad (37)$$

Further approximations to this equation are discussed later.

Formulation of the electron spin-LTS interaction requires speculation on the location and identity of the tunneling unit. In beta-alumina, observed low temperature properties are dependent on the cation present in the conduction plane. Therefore, it is assumed that some of the cations in the conduction plane are tunneling although it is improbable that these are the only tunneling units in the material. The coupling of the F^+

center to the LTS is assumed to be a Fermi contact hyperfine interaction with a cation nucleus tunneling a distance, d, through a barrier. Using the $Z^{1.5}/R_o^3$ scaling to expand the contact term, one can write the spin-LTS interaction for an F^+ in contact with a tunneling cation, characterized by an energy splitting E, as

$$H'_{T\text{-}S} = A\,\vec{I}\cdot\vec{S}\,\frac{3d}{2R_o}\begin{pmatrix}-1 & o\\ o & 1\end{pmatrix} \qquad (38)$$

or in the diagonal basis as

$$H_{T\text{-}S} = A\,\vec{I}\cdot\vec{S}\,\frac{3d}{2R_oE}\begin{pmatrix}-\xi & \Delta\\ \Delta & \xi\end{pmatrix} \quad . \qquad (39)$$

The strength of the contact hyperfine interaction between the F^+ center and the nearest neighbor sodium nucleus was determined to be $A/h \simeq 8$ MHz from the $\vec{H}_o \| c$ ENDOR data, and the hyperfine couplings for Li and K beta-alumina were obtained by scaling this value with the appropriate $Z^{1.5}\mu_n$. Average values of d can be estimated from dielectric susceptibility data.[23,26]

If the initial and final states are denoted as

$$|i\rangle = |+,\ \psi_+,\ \ldots.,\ \eta_\alpha,\ \ldots\rangle$$

$$|f\rangle = |-\ \psi_-,\ \ldots.,\ \eta_\alpha + 1,\ \ldots\rangle \quad , \qquad (40)$$

in which $|+\rangle$, $|\psi_\pm\rangle$, and $|\eta_\alpha\rangle$ are electron spin, LTS, and phonon states respectively, then the interaction Hamiltonians of Eqns. (37) and (39)

yield the following transition rate

$$W_{if} = \frac{2\pi}{\hbar} \sum_{\alpha} \left| \frac{\langle -,\psi_- | H_{T\text{-}S} | +,\psi_+ \rangle \langle \psi_+, n_\alpha + 1 | H_{T\text{-}PH} | \psi_+, n_\alpha \rangle}{-\hbar\omega_\alpha} \right.$$

$$+ \frac{\langle -,\psi_- | H_{T\text{-}S} | +,\psi_- \rangle \langle \psi_-, n_\alpha + 1 | H_{T\text{-}PH} | \psi_+, n_\alpha \rangle}{-\hbar\omega_\alpha + E}$$

$$\left. + \frac{\langle \psi_-, n_\alpha + 1 | H_{T\text{-}PH} | \psi_+, n_\alpha \rangle \langle -,\psi_+ | H_{T\text{-}S} | +,\psi_+ \rangle}{\delta} \right.$$

$$\left. + \frac{\langle \psi_-, n_\alpha + 1 | H_{T\text{-}PH} | n_\alpha, \psi_- \rangle \langle -,\psi_- | H_{T\text{-}S} | +,\psi_+ \rangle}{E + \delta} \right|^2 \left(1 + e^{E/kT}\right)^{-1} \delta_D\left(\hbar\omega_\alpha - E - \delta\right) \quad (41)$$

Here δ is the electronic Zeeman energy splitting, δ_D is the Dirac delta function, and the quantum numbers of all nuclear spin states have been suppressed. By considering the additional pair of initial and final states given by

$$|i'\rangle = |+,\psi_-, \ldots n_\alpha + 1 \ldots\rangle$$

$$|f'\rangle = |-,\psi_+, \ldots . n_\alpha \ldots\rangle \quad (42)$$

one obtains the following relaxation rate of an F^+ center, where Γ, the energy width of an intermediate LTS or phonon state, has been included and E is assumed to be much larger than δ:

$$\frac{1}{T_{1F}} = W_{if} + W_{fi} + W_{i'f'} + W_{f'i'}$$

$$= \frac{D \operatorname{sech}^2(E/2kT)}{4\tau' E^4} \left[\frac{\Delta^2(\xi\partial\xi/\partial e + \Delta\partial\Delta/\partial c)^2}{E^2 + \Gamma^2} \right.$$

$$\left. + \frac{\xi^2(\xi\partial\Delta/\partial e - \Delta\partial\xi/\partial e)^2}{\delta^2 + \Gamma^2} \right] \quad (43)$$

where

$$D = \frac{5}{2}\left(\frac{3\Lambda d}{2R_o}\right)^2 \tag{44}$$

and

$$\frac{1}{\tau} = \frac{(\xi\partial\Delta/\partial e - \Delta\partial\xi/\partial e)^2}{4\,E^2\,\tau'}$$

$$= \frac{1}{2\pi\hbar^4\rho}\left(\frac{2}{v_T{}^5} + \frac{1}{v_L{}^5}\right)\frac{E}{4}(\xi\partial\Delta/\partial e - \Delta\partial\xi/\partial e)^2 \coth\left(\frac{E}{2kT}\right) \tag{45}$$

Equation (45) represents the relaxation rate, $1/\tau$, of a LTS which results from a direct, one phonon process. In Eq. (45), v_T and v_L represents the transverse and longitudinal acoustic phonon speeds respectively, and ρ is the crystalline mass density. This expression assumes a range of $1/\tau$ values for a single value of E, but the results of the relaxation model are insensitive to this distribution since eventually there is an average over values of Δ and ξ. The factor of 5/2 in Eq. (44) results from averaging over the I = 3/2 nuclear spin matrix elements. Multi-phonon relaxation processes are not included in Eq. (45) because the direct process predicts the correct temperature dependence of the relaxation scattering observed in higher temperature dielectric[26] measurements on beta-alumina.

More precisely, $1/T_{1F}$ in Eq. (43) represents the electron spin relaxation rate of an F^+ center adjacent to a tunneling cation with LTS parameters Δ, ξ, $\partial\Delta/\partial e$, and $\partial\xi/\partial e$. Since there is a distribution of LTS parameters, it is necessary to average $1/T_{1F}$ over this distribution in order to obtain a measurable relaxation rate. Based on estimates of the LTS density, it is probable that only about 10% of the F^+ centers are

strongly coupled to any LTS.[23] In this situation, the bulk of the F^+ centers must relax via spin diffusion to the faster relaxing centers which are in hyperfine contact with a LTS. A negligible diffusion barrier exists between spins having equal Zeeman energies, and this is supported by the rapid spin-spin relaxation rates observed for F centers ($T_2 \lesssim 10^{-6}$ sec).[48] Therefore, it is reasonable to assume rapid spin diffusion among the color centers, and the observed average electron spin relaxation rate is

$$\left\langle \frac{1}{T_{1F}} \right\rangle = \frac{\int_0^{E_{max}} \int_{\Delta_{min}}^{E} \frac{1}{T_{1F}} P(E,\Delta)\, d\Delta\, dE}{\int_0^{E_{max}} \int_{\Delta_{min}}^{E} P(E,\Delta)\, d\Delta\, dE} \quad . \tag{46}$$

In order to facilitate a comparison of these results with the data of Anthony and Anderson,[23] the data is fit to a LTS density of states such that

$$\int_{\Delta_{min}}^{E} P(E,\Delta)\, d\Delta = PM\left(\frac{E}{kT_N}\right)^{0.2} + PN\left(\frac{E}{kT_N}\right)^{3} = P_o(E) \quad , \tag{47}$$

with Δ_{min}/E equal to 10^{-3}, T_N equal to 1 K, and a cutoff at E_{max}. PM and PN are constants determined from fitting the data, but PM is much greater than PN.

The spin relaxation mechanism is a process requiring one LTS and one phonon. It is shown schematically in Fig. 27. The rapid LTS relaxation rate, $1/\tau$, is represented by the solid line and involves only a tunneling state transition. This mechanism is assumed strong enough to keep the LTS system in thermal equilibrium with the phonon bath at all

Figure 27. Schematic diagram of the energy levels and product wave functions for a coupled electron spin (±) - localized tunneling state ($\psi_{\pm}$) system. The solid lines indicate transitions which contribute to the relaxation rate $1/\tau$ of the localized tunneling state, and the dashed lines indicate transitions which contribute to the slower electron spin relaxation rate $1/T_{1F}$.

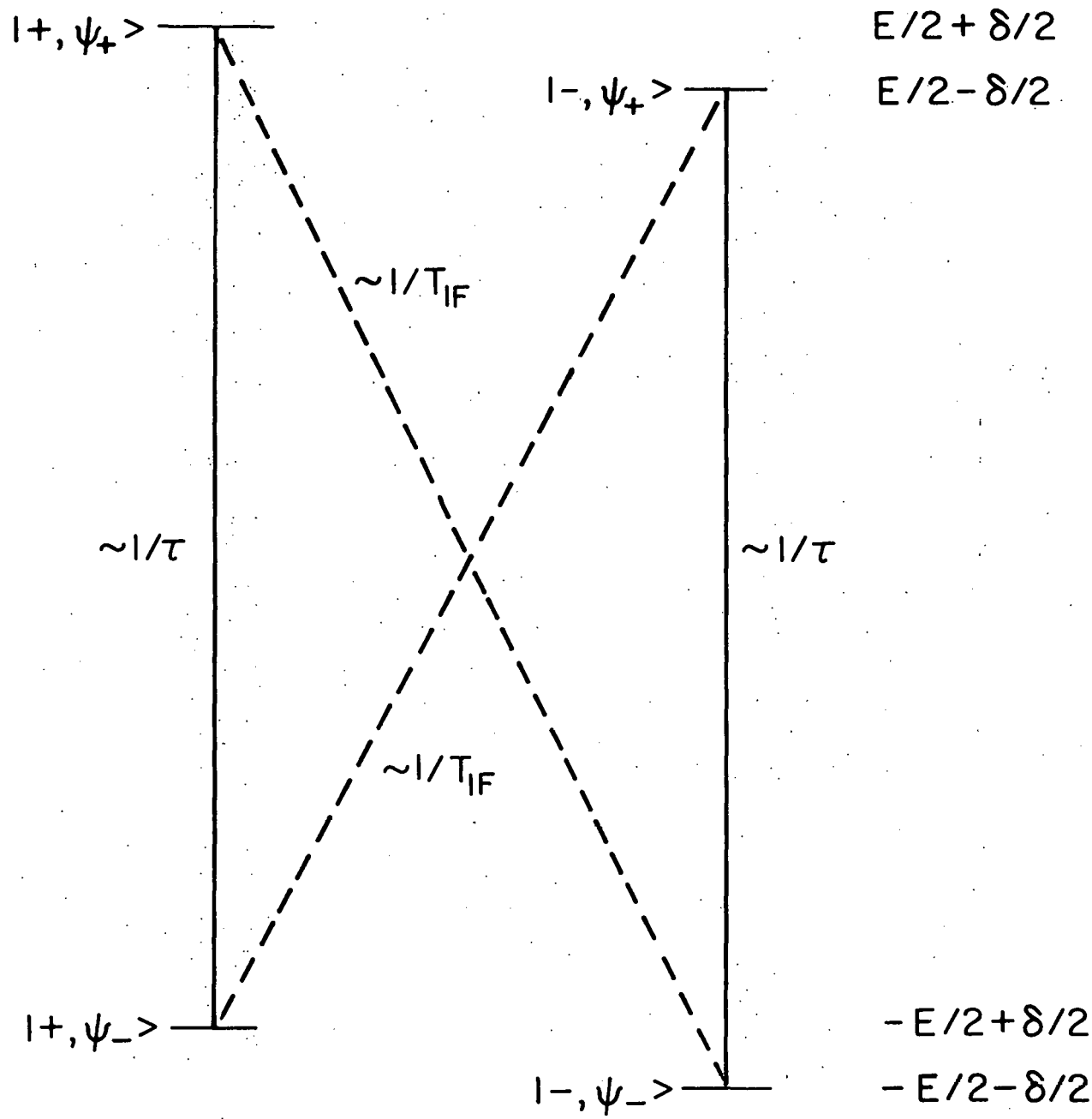
|+, ψ+>
|−, ψ+>
|+, ψ−>
|−, ψ−>
E/2 + δ/2
E/2 − δ/2
−E/2 + δ/2
−E/2 − δ/2
~1/T1F
~1/T1F
~1/τ
~1/τ

times. Electron spin relaxation proceeds via the pathways indicated by the dotted lines of Fig. 27. These transitions are weakly allowed by the hyperfine interaction which admixes the basis states, resulting in simultaneous spin and LTS transitions through the emission or absorption of a phonon. This physical picture of relaxation with the coupled spin and LTS systems is analogous to nuclear relaxation in the presence of paramagnetic impurities in the fast diffusion limit.[67] Figure 27 also illustrates this nuclear relaxation phenomenon for nuclei, with a Zeeman splitting δ, which are weakly coupled to fast relaxing electrons, with a Zeeman splitting $E >> \delta$. As before, nuclear relaxation occurs by the transitions indicated by the dotted lines, and these transitions are allowed by spin function admixtures induced by the weak dipole-dipole interaction between the two spin systems.

Two of the interesting properties of this model are the different magnetic field and temperature dependences predicted by the two terms in Eq. (43). If one assumes that the density of tunneling states, P(E), is a constant up to some cut-off E_{max}, and that Γ is much smaller than E, the LTS energy splitting, then the first term in Eq. (43) predicts that $\langle 1/T_{1F} \rangle \propto H^0 T^2$ for $kT << E_{max}$. With the additional assumption that $\delta = g\mu_B H_o >> \Gamma$, the second term predicts in contrast that $\langle 1/T_{1F} \rangle \propto H^{-2} T^4$. Both terms predict a linear temperature dependence at higher temperatures, where $kT \gtrsim E_{max}$. Therefore, at low temperatures the model predicts $\langle 1/T_{1F} \rangle \propto T^{2-4}$. This result is confirmed by the data as shown in Fig. 28. In this diagram, each set of data was fit to a function of the form

$$\langle 1/T_{1F} \rangle = BT^n + C \qquad (48)$$

Figure 28. Log $\langle 1/T_{1F} \rangle$ vs Log T for Na, Li, and K beta-alumina as measured at a microwave frequency of 16.5 GHz. The curves and table result from fitting the data to the function described by Eq. (48) of the text. A similar fit of the Na beta-alumina data at 9.5 GHz is not shown, but it produced a $T^{2.02}$ temperature dependence for $\langle 1/T_{1F} \rangle$.

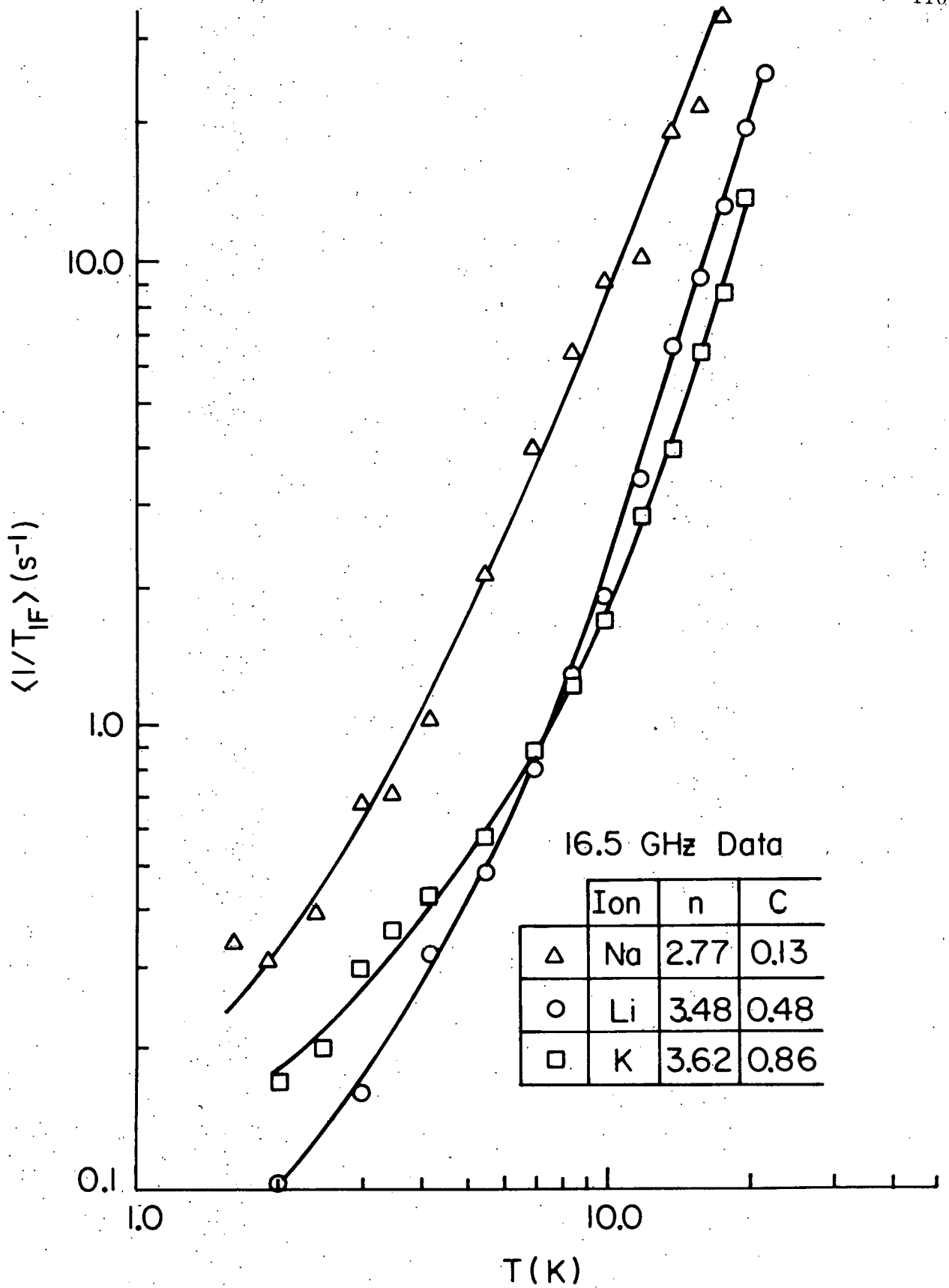
10.0
1.0
0.1
1.0
10.0
T(K)
⟨1/T1F⟩ (s⁻¹)
16.5 GHz Data
Ion
n
C
Na
2.77
0.13
Li
3.48
0.48
K
3.62
0.86

where C is a positive constant. The $T^{3.48}$ and $T^{3.62}$ behavior of the Li and K beta-alumina data suggests that unless $P(E) \propto E^{1.5}$ for $1\ K \leq E/k \leq 10\ K$, the second term in Eq. (43) must contribute significantly to the F^+ relaxation rate in these materials. None of the data from other experiments supports the existence of a strongly E dependent LTS density of states in this region.[23,26] The $T^{2.02}$ and $T^{2.77}$ power law fits of the Na data at X and Ku-band frequencies may reflect a lower cut-off value of E_{max}/k, the values of which have been reported as 65, 80, and 130 K for Na, K, and Li beta-alumina respectively.[23] A lower cut-off energy tends to linearize the T dependence at a lower temperature. Another factor which supports the dominance of the second term in Eq. (43) is the small, but clearly perceptable, frequency dependence of $\langle 1/T_{1F} \rangle$ shown in Fig. 25. The Ku-band relaxation data is consistently slower than the corresponding X-band data. However, the field dependence is much reduced from H_o^{-2}, a result predicted only in the limit that $\delta >> \Gamma$.

Lyo and Orbach[68] have proposed that the first and fourth terms in Eq. (41) can explain the optical homogeneous linewidth which varies as T^2 in rare earth doped glasses.[69,70] Since the first excited electronic state in a rare earth ion has an energy $\gtrsim 50\ cm^{-1}$ above the ground state, only scattering processes in which the ion remains in the same electronic state are energetically favorable. Under these conditions ($|+\rangle = |-\rangle$), only the first and fourth terms, due to Lyo and Orbach, are then permitted.

In Eq. (41), the intermediate states are such that only one of the two Hamiltonian operators, $\mathcal{H}_{T\text{-}S}$ or $\mathcal{H}_{T\text{-}PH}$, is off-diagonal with respect to the LTS. Another spin relaxation mechanism is possible in which both of these operators are off-diagonal with respect to the tunneling states. The

resulting temperature dependence of this mechanism is identical to that of an ordinary one phonon direct process, i.e., proportional to T for $kT >> \delta$.

The only remaining T_1 process involving these interactions in first order is the resonant cross relaxation between a spin and an LTS for which $E=\delta$. Assuming: (1) that the resonant tunneling states remain in thermal equilibrium with the lattice as the spins and resonant tunneling states undergo mutual "flip-flop" transitions, and (2) that a rapid spin diffusion rate can be ascribed to the spin system, then the resulting relaxation rate is independent of temperature. Such resonant pairs of spins and tunneling states will be very rare, but also very effective in bringing the spin system to thermal equilibrium at low temperatures where other processes freeze out.

Another relaxation mechanism is a two LTS process proposed by Reinecke and Ngai[71] to explain nuclear relaxation in glasses. This process is not considered to be a reasonable explanation for the observed electron spin relaxation data for two reasons. First, it requires the improbable situation of two LTS states having an energy difference δ, to be coupled strongly to the same F^+ center. Second, the predicted relaxation rate for this mechanism varies as T if P(E) is a constant and $kT << E_{max}$.

Two possible temperature dependences have been considered in order to account for the observed relaxation rates at the lowest temperatures, where the mechanism involved in Eq. (43) becomes very weak. The relaxation rate was assumed to be either a constant, C, or linear in temperature, GT. The fit of the data at the higher temperatures is only slightly affected by this choice, and only those fits which include the GT term are reported here.

In addition to the LTS system, excess vibrational states have been observed in beta-alumina. Infrared spectra,[72] Raman scattering data,[73] and heat capacity results[74] were explained by speculating the existence of Einstein oscillator states due to cation motion within the conduction plane. These excitations have well defined energies instead of the broad distribution characteristic of the LTS. If the spins interacted with a Debye phonon system augmented by these Einstein oscillators instead of the LTS, the expression for the relaxation rate would be $\langle 1/T_{1F} \rangle \propto e^{-E'/kT}$ for $E' \gg kT$,[75] where E' is the Einstein oscillator energy. The data are not described by this temperature dependence. Also infrared, Raman, and heat capacity experiments all failed to observe Einstein oscillator states of comparable energy in Li beta-alumina, but the same spin relaxation phenomena is observed in Li beta-alumina as in Na and K beta-alumina. For these reasons, the LTS and not the excess vibrational states allow the phonons to relax the F^+ centers. It is possible that these excess vibrational states also interact with the LTS producing a slightly different spin relaxation temperature dependence than predicted by a simple Debye phonon spectrum, but no attempt has been made to account for this effect in the data analysis.

D. Comparison Between Theory and Experiment

In this section basic assumptions about the nature of Γ and $H_{T\text{-}PH}$ are made, and based on these assumptions values of the LTS parameters are estimated which provide a quantitative description of the electron spin relaxation data. Using the theory presented in the previous section, the

LTS parameterization can be compared with the results from low temperature bulk measurements on beta alumina. Through this process, it is possible to obtain a self consistent explanation of the electron spin relaxation phenomena in beta-alumina and reconfirm properties of the LTS model previously observed through bulk measurements only.

It is convenient to begin this discussion by assuming that Γ is due to a large LTS linewidth, i.e.,

$$\Gamma_{LTS} \propto \hbar\left(\frac{1}{\tau} + \frac{1}{T_2}\right) \quad . \tag{49}$$

Here $1/T_2$ is an LTS-LTS relaxation rate, and it has been widely studied through a variety of acoustic and dielectric experiments.[16,76] Although the origin of $1/T_2$ is not completely understood, it is believed to be only weakly dependent on T and E,[77,78] and at T = 1.5 K and E/h = 9 GHz, it has been estimated at 2×10^9 s^{-1} in borosilicate BK7.[79] The LTS-lattice relaxation rate is measured indirectly in any resonant contribution to dielectric susceptibility or thermal conductivity, and in practically all glasses it is found to be less than about 10^6 s^{-1} for an E/h of 9 GHz and at a temperature of 2 K. In sodium beta-alumina dielectric saturation has been observed,[26] and this allowed the investigators to estimate τT_2 at 6×10^{-11} s^2 for an E/h of 11.5 GHz and a temperature of 1 K. All this experimental evidence indicates that δ is much larger than Γ_{LTS} in the temperature region of our experiments, where $\delta/h \approx 10$ GHz.

Based on the temperature dependence and weak field dependence exhibited in the electron spin relaxation data, it would still be possible to reproduce these results for $\delta >> \Gamma$ if the two terms of Eq. (43) were of comparable size. The H_o and T dependence of each set of data could

then be fit by adjusting the relative contributions of each of these terms. Under these approximations

$$\frac{1}{T_{1F}} \propto \frac{\Delta^2(\xi\partial\xi/\partial e + \Delta\partial\Delta/\partial e)^2}{E^2} + \frac{\xi^2(\xi\partial\Delta/\partial e - \Delta\partial\xi/\partial e)^2}{\delta^2} \quad . \quad (50)$$

Making the usual assumption that $\partial\xi/\partial e >> \partial\Delta/\partial e$ would lead to the result that the second term of Eq. (50) is much larger than the first if $E >> \delta$. In order to make the contribution from the first term significant, one must make the diagonal components of $H_{T\text{-}PH}$ larger while diminishing the off-diagonal elements. This can be accomplished by setting $\partial\xi/\partial e \simeq \partial\Delta/\partial e$. However, this same LTS-phonon interaction describes acoustic attenuation and thermal conductivity in glasses. In these experiments resonant scattering processes are produced by the contribution of the off-diagonal components of $H_{T\text{-}PH}$, and relaxation scattering processes are caused by the diagonal components.[15] The assumption that $\partial\xi/\partial e >> \partial\Delta/\partial e$ produces the correct relative sizes of the relaxation and resonant processes observed in acoustic measurements to within a factor of 10.[16] In order to force the two terms in Eq. (50) to contribute equally at 10 K, with $E_{max}/k \simeq 50$ K, and $\delta/h \simeq 10$ GHz, the diagonal and off-diagonal elements of $H_{T\text{-}PH}$ must be adjusted so as to enhance the relaxation scattering processes over the resonant scattering processes by a factor of 1,000 or more. Such a large asymmetry in the relative strengths of the two processes has not been observed experimentally in any glass, including beta-alumina. Therefore, under the assumption that $\delta >> \Gamma$, the second term in Eq. (50) dominates, and the model would then predict a much stronger magnetic field dependence than is observed.

Another contribution to Γ could arise from short phonon lifetimes. Here $\Gamma_{PH} \simeq \hbar v/\ell$, where v is an acoustic phonon velocity and ℓ is a phonon mean free path. In a perfect crystal ℓ is limited by the finite crystal size and weak phonon-phonon scattering resulting from anharmonic terms in the lattice potential. In a glass, however, ℓ is limited by the structural disorder of the material, at least for phonons with wavelengths comparable to the size of a unit cell of the glass. Using this physical picture, Kittel[80] explained the thermal conductivity data of glasses by suggesting a constant, temperature independent mean free path $\ell_o \simeq 10^{-7}$ cm for phonons with $\omega/2\pi \gtrsim 100$ GHz. These higher frequency phonons are just those responsible for the relaxation of the higher energy tunneling states, which in turn are responsible for the spin relaxation of the F^+ center in our model. With $v \simeq 10^5$ cm/s, $\Gamma_{PH}/h \simeq v/2\pi\ell_o$ is of the order of 100 GHz, and under these conditions $\Gamma_{PH} \gtrsim \delta$ since $\delta/h \simeq 10$ GHz in the relaxation experiments. Therefore, the short phonon lifetimes observed in glasses may explain the weak magnetic field dependence displayed by the data. Defining $(1/2)\cdot\partial\xi/\partial e = \gamma$, and assuming $\partial\Delta/\partial e \simeq 0$,[15] Eq. (43) is rewritten as

$$\frac{1}{T_{1F}} \simeq \frac{D\ \mathrm{sech}^2(E/2kT)\ \xi^2}{\tau E^2}\left\{\frac{1}{E^2 + \Gamma_{PH}^2} + \frac{1}{\delta^2 + \Gamma_{PH}^2}\right\} . \qquad (51)$$

It must be noted that the magnetic field dependence has been explained with a value of Γ_{PH} such that $\Gamma_{PH}/\hbar \gg 1/\tau$. In so doing it has been assumed that the scattering processes which determine Γ_{PH} for high energy phonons do not involve the LTS system, and these scattering processes do not efficiently produce electron spin transitions.

When Eq. (51) is applied to electron spin relaxation in glasses, the relative sizes of E, Γ_{PH}, and δ are such as to make the second term dominant. The solid and dotted lines in Figs. 25 and 26 are the result of using Eq. (51) to calculate $\langle 1/T_{1F} \rangle$. The parameters used in these calculations are displayed in Table IV along with estimates of the same parameters determined by Anthony and Anderson in the analysis of their data on the beta-alumina.[23] In these fits of the data, the first term in Eq. (51) contributes less than 1% to the predicted relaxation rates.

There are too many adjustable parameters in the LTS model of glasses to allow a unique determination of these quantities from an analysis of relaxation data alone. The same can be said regarding most measurements on glasses. What can be accomplished is to produce a fit of the data in which the resulting parameters from all available experiments can be compared. For this reason the parameterization scheme of Anthony and Anderson[23] has been adopted, although it is not a unique description of the LTS system in beta-alumina. However, the values estimated by them do describe the results of several different experiments on beta-alumina as indicated by the solid lines in Fig. 3-7, and a detailed comparison of the parameters obtained from these two studies reveals similarities which support the model of the F^+ center relaxation in beta-alumina. The temperature dependence observed for any of the experiments is determined by PM, PN, and E_{max}/k. By examining the data of Table IV and comparing the relative size of these parameters for each cation, the same trends are observed in both sets of experiments. The magnitudes of these parameters are also in agreement, but due to the normalization of P(E) in our expression of $\langle 1/T_{1F} \rangle$, the relaxation model is only sensitive

TABLE IV

SUMMARY OF THE PARAMETERS FOR Na, Li, AND K BETA-ALUMINA USED TO GENERATE THE CURVES IN FIGS. 25 AND 26. ALL PARAMETERS ARE DEFINED IN THE TEXT. RESULTS OF ANTHONY AND ANDERSON ARE INCLUDED FOR COMPARISON

Parameter	Units	Na	LI	K	Source
ρ	g cm^{-3}	3.22	3.14	3.33	a
v_T	10^5 cm s^{-1}	3.8	4	4.3	a
v_L	10^5 cm s^{-1}	9.1	9	9.5	a
$\Delta_{min/E}$	---	10^{-3}	10^{-3}	10^{-3}	a
PM	10^{33} $erg^{-1}cm^{-3}$	2.4	4.9	1.2	a
PN	10^{29} $erg^{-1}cm^{-3}$	2.5	0.0	0.15	b
E_{max}/k	K	40	90	80	b
$\gamma \cdot d$	10^{-8} cm eV	0.12	0.40	0.18	b
$A(\mu_n, Z)$	10^6 Hz	8.0	1.67	3.20	b
R_o	10^{-8} cm	3.2	3.2	3.2	b
Γ_{PH}	10^9 Hz	25	25	25	b
G	s^{-1} K^{-1}	0.17	0.06	0.10	b
PN	10^{29} $erg^{-1}cm^{-3}$	4.5	0.36	0.26	c
E_{max}/k	K	65	130	80	c
γ[d]	eV	0.2	0.6	0.1	c
γ[e]	eV	0.3	1.4	0.9	c
d	10^{-8} cm	0.3	0.2	0.1	c

a. Common parameter values used by Anthony and Anderson (Ref. 23) and in this work.
b. Parameter values used in this work only.
c. Parameter values from Ref. 23 which differ from those used in this work.
d. Results from thermal conductivity data (Ref. 23).
e. Results from dielectric susceptibility data (Ref. 23).

to the relative size of PM to PN. The relaxation data could also have been fit with a constant P(E) by making small changes in the value of E_{max}/k. The magnitude of the predicted relaxation rate is determined by γ, d, A, and R_o. These parameters are not independently determined in the model, but it is significant that this theory predicts the observed relaxation rate for values of γ and d which are in good agreement with those of Anthony and Anderson.[23] Also, the values of A and R_o are reasonable when the structure and observed hyperfine couplings in the beta-alumina are considered. In comparing the relative values of $\gamma \cdot d$ required to fit this data and those of Anthony and Anderson, it must be noted that the same trends can be seen in the relaxation and dielectric susceptibility data as one changes from cation to cation. This further supports the model of tunneling cations interacting with F^+ centers via contact hyperfine interactions. The estimate of a constant Γ_{PH} results from the weak field dependence displayed in Fig. 25. The value of $\Gamma_{PH}/h \approx 25$ GHz is within an order of magnitude of estimated phonon mean free paths in glasses based on thermal conductivity data. Considering the scatter of the data in Fig. 25, larger values of Γ_{PH} would also be acceptable, producing an even weaker magnetic field dependence. Another contribution to the magnetic field dependence is the dependence of Γ_{PH} upon the phonon energy. This is observed for lower phonon energies[81,82] and may influence the F^+ relaxation rate at those temperatures where the rate is just becoming temperature dependent. However, the scatter in the relaxation data precludes more detailed calculations. The coefficient G of the low temperature, linear relaxation rate was determined from the lowest temperature data. Its origin was discussed in the previous section.

E. Conclusions and Comments

Electron spin relaxation measurements on F^+ centers in beta-alumina have reconfirmed that relaxation in a disordered material is markedly different from that which occurs in ordered ionic solids, and the data and model presented here constitute the first quantitative study of electron spin relaxation in a glass. The proposed LTS-phonon relaxation mechanism accurately predicts the magnitude and temperature dependence observed in the electron spin relaxation data. The LTS parameterization used to describe the data is in good agreement with previous heat capacity, thermal conductivity, and dielectric susceptibility measurements on beta-alumina. In addition, it is inferred that phonon lifetime effects are responsible for the weak magnetic field dependence displayed in the data.

This model does not explain both the anomalous optical homogeneous linewidth[69,70] and nuclear relaxation[71,83] observed in glasses. Both of these quantities are believed to be proportional to T^n for $1 \lesssim n \lesssim 2$ and $T \lesssim 100$ K, but there are few data points in the 1-20 K range suggesting that these early studies may be overlooking some effects due to the LTS system. Also, these experiments have not been performed on beta-alumina at this time.

In beta-alumina, it seems that the distribution of tunneling states extends to unusually large energies, and even the higher energy excitations conform well to the simple LTS model. As a result, the LTS model describes the $\gtrsim$ 10 K dielectric[26] and ultrasonic[84] data for beta-alumina where in other glasses, the data usually deviates from the simple behavior predicted by the LTS theory in this temperature region. The 2-20 K electron spin

relaxation measurements actually probe these same high energy LTS suggesting that the relaxation data for other glasses may not be as conclusive as the beta-alumina results. For example, a lower value of E_{max}/k would produce a relaxation rate with a weaker temperature dependence than the one observed in beta-alumina, and it is possible some of the variation in the electron spin relaxation, nuclear relaxation, and optical homogeneous linewidth is caused by differences in the glasses. The contribution of other scattering processes also cannot be overlooked when seeking to explain T^{1-2} behavior in optical linewidth and nuclear relaxation data.

These properties of glasses have been recognized only recently, but it is hoped that the success of this study of electron spin relaxation in beta-alumina will be a first step towards a broad understanding of relaxation phenomena associated with disorder.

BIBLIOGRAPHY

1. J. H. Kennedy, in Topics in Applied Physics: Solid Electrolytes, edited by S. Geller (Springer-Verlag, New York, 1977), Vol. 21, p. 105.

2. C. R. Peters, M. Bettman, J. W. Moore, and M. D. Glick, Acta Cryst. B 27, 1826 (1971).

3. W. L. Roth, F. Reidinger, and S. LaPlaca, in Superionic Conductors, edited by G. D. Mahan and W. L. Roth (Plenum Press, New York, 1976), p. 223.

4. P. J. Anthony, Ph.D. Thesis (University of Illinois at Urbana-Champaign, 1978), unpublished.

5. W. L. Roth, J. Solid State Chem. 4, 60 (1972).

6. T. Kaneda, J. B. Bates, and J. C. Wang, Solid State Commun. 28, 469 (1978).

7. John N. Mundy, in Fast Ion Transport in Solids, edited by P. Vashista, J. N. Mundy, and G. K. Shenoy (North-Holland, New York, 1979), p. 159.

8. J. C. Wang, M. Gaffari, and Sang-il Choi, J. Chem. Phys. 63, 772 (1975).

9. J. P. Boilot, G. Collin, R. Comes, J. Thery, R. Collongues, and A. Guiner, in Superionic Conductors, edited by G. D. Mahan and W. L. Roth, (Plenum, New York, 1976), p. 243.

10. D. B. McWhan, P. D. Dernier, C. Vettier, A. S. Cooper, and J. P. Remeika, Phys. Rev. B 17, 4043 (1978).

11. D. B. McWhan, S. J. Allen, J. P. Remeika, and P. D. Dernier, Phys. Rev. Lett. 35, 953 (1975).

12. Hiroshi Sato and Ryoichi Kikuchi, in Fast Ion Transport in Solids, edited by P. Vashista, J. N. Mundy, and G. K. Shenoy (North-Holland, New York, 1979), p. 337.

13. Charles Kittel, Introduction to Solid State Physics, 4th ed. (John Wiley and Sons, New York, 1971).

14. T. L. Smith, Ph.D. Thesis (University of Illinois at Urbana-Champaign, 1979), unpublished.

15. J. Jackle, Z. Phys. 257, 212 (1972).

16. S. Hunklinger and W. A. Arnold, in Physical Acoustics, edited by W. P. Mason and R. N. Thurston (Academic Press, New York, 1976), Vol. 12, p. 155.

17. J. Jackle, L. Piche, W. Arnold, and S. Hunklinger, J. of Non-Cryst. Solids 20, 365 (1976).

18. M. von Schickfus and S. Hunklinger, J. Phys. C 9, L439 (1976).

19. M. von Schickfus, S. Hunklinger, and L. Piche, Phys. Rev. Lett. 35, 876 (1975).

20. M. von Schickfus and S. Hunklinger, Phys. Lett. A 64, 144 (1977).

21. P. W. Anderson, B. I. Halperin, and C. M. Varma, Philos. Mag. 25, 1 (1972).

22. W. A. Phillips, J. Low Temp. Phys. 7, 351 (1972).

23. P. J. Anthony and A. C. Anderson, Phys. Rev. B 19, 5310 (1979).

24. P. J. Anthony and A. C. Anderson, Phys. Rev. B 16, 3827 (1977).

25. P. J. Anthony and A. C. Anderson, Phys. Rev. B 14, 5198 (1976).

26. U. Strom, M. von Schickfus, and S. Hunklinger, Phys. Rev. Lett. 41, 910 (1978).

27. Ulrich Strom, private communication.

28. D. Gourier, J. Antoine, D. Vivien, J. Thery, J. Livage and R. Collongues, Phys. Stat. Sol. (a) 41, 423 (1977).

29. K. O'Donnell, R. C. Barklie, and B. Henderson, J. Phys. C 11, 3871 (1978).

30. D. Gourier, D. Vivien, and J. Livage, Phys. Stat. Sol. (a) 56, 247 (1979).

31. M. M. Abraham and H. J. Stapleton, unpublished.

32. R. C. Barklie, K. O'Donnell, and B. Henderson, J. Phys. C 11, 3881 (1978).

33. A. Abragam and B. Bleaney, Electron Paramagnetic Resonance of Transition Metal Ions, (Clarendon, Oxford, 1970).

34. M. Giordano, F. Momo, and A. Sotgiu, J. Phys. E 12, 815 (1979).

35. G. E. Pake and T. L. Estle, The Physical Principles of Electron Paramagnetic Resonance, 2nd ed., (W. A. Benjamin, Reading, 1973).

36. C. P. Slichter, Principles of Magnetic Resonance, 2nd ed., (Springer-Verlag, New York, 1978).

37. Theodore G. Castner and Werner Kanzig, J. Phys. Chem. Solids 3, 178 (1957).

38. B. Henderson and J. E. Wertz, Defects in the Alkaline Earth Oxides, (Taylor and Francis, London, 1977).

39. O. F. Schirmer, J. Phys. Chem. Solids 32, 499 (1971).

40. O. F. Schirmer, J. Phys. Chem. Solids 29, 1407 (1968).

41. W. Marshall, in Paramagnetic Resonance, edited by W. Low (Academic, New York, 1963), Vol. 1, p. 347.

42. R. C. Barklie, J. R. Niklas, and J. M. Spaeth, J. Phys. C 13, 1757 (1980).

43. R. C. Barklie, J. R. Niklas, and J. M. Spaeth, J. Phys. C 13, 1745 (1980).

44. Jordan J. Markham, in Solid State Physics, edited by Frederick Seitz and David Turnbull (Academic, New York, 1966), Supp. 8.

45. J. E. Wertz, J. W. Orton, and P. Auzins, Discussions Faraday Soc. 31, 140 (1961).

46. R. H. Bartram, C. E. Swenberg, and S. Y. La, Phys. Rev. 162, 759 (1967)

47. W. P. Unruh and J. W. Culvahouse, Phys. Rev. 154, 861 (1967).

48. H. Seidel and H. C. Wolf, in Physics of Color Centers, edited by W. Fowler (Academic, New York, 1968), p. 557.

49. A. E. Hughes and B. Henderson, in Point Defects in Solids, edited by J. H. Crawford and L. M. Slifkin (Plenum, New York, 1972), Vol. 1.

50. W. C. Holton and H. Blum, Phys. Rev. 129, 89 (1962).

51. Intaik Chung, Ph.D. Thesis (S.U.N.Y. at Albany, 1974), unpublished.

52. R. C. Herrick, Ph.D. Thesis (University of Illinois at Urbana-Champaign, 1976), unpublished.

53. M. F. Deigen and V. Ya. Zevin, Soviet Phys. JETP 12, 785 (1960).

54. V. Ya. Zevin, Soviet Phys. Solid State 3, 439 (1961).

55. D. W. Feldman, R. W. Warren, and J. G. Castle, Jr., Phys. Rev. 135, A470 (1964).

56. R. W. Warren, D. W. Feldman, and J. G. Castle, Jr., Phys. Rev. 136, A1347 (1964).

57. H. Panepucci and L. F. Mollenauer, Phys. Rev. 178, 589 (1969).

58. V. Narayanamurti and R. O. Pohl, Rev. of Mod. Phys. 42, 201 (1970).

59. M. F. Deigen, B. D. Shanina, V. S. Vikhnin, I. M. Zaritski, A. A. Konchits, G. Korradi, R. Voska, V. M. Maevski, and V. V. Udod, Soviet Phys. Solid State 15, 310 (1973).

60. Hiroshi Ohkura, Masao Matsuoka, and Yuzo Mori, J. Phys. Soc. Japan 39, 547 (1975).

61. Hiroshi Ohkura, Yuzo Mori, Masao Matsuoka, Tohru Watanabe, and Akio Satoh, Progress of Theoretical Phys. Supp. 57, 68 (1975).

62. Baruch Fischer and Michael Klein, Phys. Rev. Lett. 43, 289 (1979).

63. Michael W. Klein, Baruch Fischer, A. C. Anderson, and P. J. Anthony, Phys. Rev. B 18, 5887 (1978).

64. D. W. Feldman, J. G. Castle, Jr., and G. R. Wagner, Phys. Rev. 145, 237 (1966).

65. J. Murphy, Phys. Rev. 145, 241 (1966).

66. W. L. Gamble, I. Miyagawa, and R. L. Hartman, Phys. Rev. Lett. 20, 415 (1968).

67. T. J. Schmugge and C. D. Jeffries, Phys. Rev. 138, A1785 (1965).

68. S. K. Lyo and R. Orbach, to be published.

69. P. M. Selzer, D. L. Huber, D. S. Hamilton, W. M. Yen, and M. J. Weber, Phys. Rev. Lett. 36, 813 (1976).

70. J. Hegarty and W. M. Yen, Phys. Rev. Lett. 43, 1126 (1979).

71. T. L. Reinecke and K. L. Ngai, Phys. Rev. B 12, 3476 (1975).

72. A. S. Barker, Jr., J. A. Ditzenberger, and J. P. Remeika, Phys. Rev. B 14, 386 (1976).

73. C. H. Hao, L. L. Chase, and G. D. Mahon, Phys. Rev. B 13, 4306 (1976).

74. D. B. McWhan, C. M. Varma, F. L. S. Hsu, and J. P. Remeika, Phys. Rev. B 15, 553 (1977).

75. D. W. Feldman, J. G. Castle, Jr., and J. Murphy, Phys. Rev. 138, A1208 (1965).

76. Brage Golding and John E. Graebner, in Physics of Amorphous Insulators, edited by W. A. Phillips (Springer-Verlag, New York), in preparation.

77. J. L. Black and B. I. Halperin, Phys. Rev. B 16, 2879 (1977).

78. J. Joffrin and A. Levelut, J. Phys. (Paris) 36, 811 (1976).

79. A. Bachellerie, P. Doussineau, A. Levelut, and T.-T. Ta, J. Phys. (Paris) 38, 69 (1977).

80. Charles Kittel, Phys. Rev. 75, 972 (1949).

81. W. Dietsche and H. Kinder, Phys. Rev. Lett. 43, 1413 (1979).

82. M. D. Zaitlin and A. C. Anderson, Phys. Rev. B 13, 4475 (1975).

83. J. Szeftel and H. Alloul, J. Non. Cryst. Solids 29, 253 (1978).

84. P. Doussineau, R. G. Leisure, A. Levelut, and J.-Y. Prieur, J. Phys. Lett. (Paris) 41, L-65 (1980).

VITA

Steven Ross Kurtz was born in [redacted]. He attended public school in Clinton, Maryland, and was graduated from Surrattsville Senior High School in 1971. He entered Bucknell University, in Lewisburg, Pennsylvania, and received the Bachelor of Science degree in 1975. Since then he has attended the University of Illinois, at Urbana-Champaign, from which he received the Master of Science degree in physics in 1977. He was awarded an Exxon Research Fellowship in 1979, and he is a member of the American Physical Society.